

**Best Available
Copy
for all Pictures**

AD-771 278

GEOLOGIC RECONNAISSANCE AND LITHOLOGIC IDENTIFICATION
BY REMOTE SENSING

ENVIRONMENTAL RESEARCH INSTITUTE OF MICHIGAN

PREPARED FOR
ADVANCED RESEARCH PROJECTS AGENCY
BUREAU OF MINES

DECEMBER 1973

DISTRIBUTED BY:

NTIS

National Technical Information Service
U. S. DEPARTMENT OF COMMERCE

AD 771278
191700-8-F

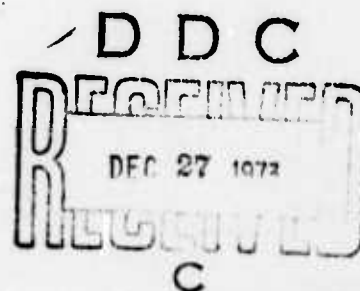
Final Report

GEOLOGIC RECONNAISSANCE AND LITHOLOGIC IDENTIFICATION BY REMOTE SENSING

5 May 1972 Through 30 April 1973

ROBERT VINCENT
THOMAS WAGNER
BEN DRAKE
PHILIP JACKSON

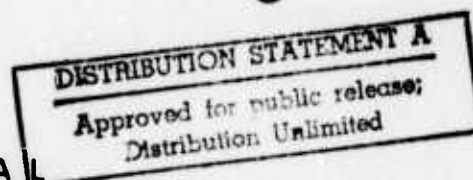
Radar and Optics Division



DECEMBER 1973

**ENVIRONMENTAL
RESEARCH INSTITUTE
OF MICHIGAN**

FORMERLY WILLOW RUN LABORATORIES,
THE UNIVERSITY OF MICHIGAN



Sponsored by
Advanced Research Projects Agency
ARPA Order No. 1579
and Contract No. HO220064

Reproduced by
NATIONAL TECHNICAL
INFORMATION SERVICE
U S Department of Commerce
Springfield VA 22151

NOTICES

Sponsorship. The work reported herein was conducted by the Environmental Research Institute of Michigan for the Advanced Research Projects Agency of the Department of Defense and was monitored by the U.S. Bureau of Mines under Contract Number HO220064, ARPA Order No. 1579, Amendment 3. The Project Officer was Frank Ruskey.

Disclaimer. The views and conclusions contained in this document are those of the authors and should not be interpreted as necessarily representing the official policies, either expressed or implied, of the Advanced Research Projects Agency or of the U.S. Government.

Distribution. Initial distribution is indicated at the end of this document.

DDC Availability. Qualified requesters may obtain copies of this document from:

Defense Documentation Center
Cameron Station
Alexandria, Virginia 22314

Final Disposition. After this document has served its purpose, it may be destroyed. Please do not return it to the Environmental Research Institute of Michigan.

ACQUISITION NO.	
RTHE	
DIC	
MANUSCRIPTS	
IDENTIFICATION	
BY	
DISSEMINATION/AVAILABILITY	
SEC.	
A	

✓ Per 7000 50

UNCLASSIFIED

SECURITY CLASSIFICATION OF THIS PAGE (When Data Entered)

REPORT DOCUMENTATION PAGE		READ INSTRUCTIONS BEFORE COMPLETING FORM
1 REPORT NUMBER	2 GOVT ACCESSION NO	3 RECIPIENT'S CATALOG NUMBER
4 TITLE (and Subtitle) Geologic Reconnaissance and Lithologic Identification by Remote Sensing		5 TYPE OF REPORT & PERIOD COVERED Final Report 5 May 1972-30 April 1973
7 AUTHOR(s) Robert Vincent, Thomas Wagner, Ben Drake, Philip Jackson		6 PERFORMING ORG REPORT NUMBER 191700-8-F
9 PERFORMING ORGANIZATION NAME AND ADDRESS Environmental Research Institute of Michigan Radar and Optics Division P.O. Box 618, Ann Arbor, MI 48107		8 CONTRACT OR GRANT NUMBER(s) HO220064
11 CONTROLLING OFFICE NAME AND ADDRESS Advanced Research Projects Agency 1400 Wilson Blvd., Arlington, VA 22209		10 PROGRAM ELEMENT PROJECT TASK AREA & WORK UNIT NUMBERS ARPA Order No. 1579, Amendment 3, Program Code 2F10
14 MONITORING AGENCY NAME AND ADDRESS (if different from Controlling Office) U.S. Dept. of Interior, Bureau of Mines Building 20, Denver Federal Center Denver, CO 80225		12 REPORT DATE December 1973
		13 NUMBER OF PAGES 119
		15 SECURITY CLASS (of this report) Unclassified
16 DISTRIBUTION STATEMENT (of this Report) Initial distribution is indicated at the end of this document.		15a DECLASSIFICATION/DOWNGRADING SCHEDULE N/A
<div style="border: 1px solid black; padding: 5px; text-align: center;"> DISTRIBUTION STATEMENT A Approved for public release; </div>		
17 DISTRIBUTION STATEMENT (of the abstract included in this report) Unclassified		
18 SUPPLEMENTARY NOTES Principal Investigator, Philip L. Jackson		
19 KEY WORDS (Continue on reverse side if necessary and identify by block number) Geology, Remote Sensing, Geologic Reconnaissance, Lithologic Identification, Igneous Rocks, Thermal Infrared, Soil Identification, Image Ratioing		
20 ABSTRACT (Continue on reverse side if necessary and identify by block number) The role of remote sensing in geologic reconnaissance for purposes of tunnel site selection was studied further and a test case was undertaken to evaluate this geological application. Airborne multispectral scanning (MSS) data were obtained in May, 1972, over a region between Spearfish and Rapid City, South Dakota. With major effort directed toward the analysis of these data, the following geologic features were discriminated: (1) exposed rock areas, (2) five separate rock groups, (3) large-scale structures. This discrimination was accomplished by		

DD FORM 1473 EDITION OF 1 NOV 65 IS OBSOLETE
1 JAN 73

UNCLASSIFIED

SECURITY CLASSIFICATION OF THIS PAGE (When Data Entered)

UNCLASSIFIED

SECURITY CLASSIFICATION OF THIS PAGE (When Data Entered)

20. ABSTRACT (Continued)

ratioing multispectral channels. Laboratory-type remote sensing data are shown to permit geologic interpretation. These technological advances are the first steps toward airborne lithologic identification. The method has the potential for still finer discrimination and, hence, application to more rock types.

UNCLASSIFIED

SECURITY CLASSIFICATION OF THIS PAGE (When Data Entered)

PREFACE

The work described in this final report was supported by the Advanced Research Projects Agency of the Department of Defense and was monitored by the U.S. Bureau of Mines under Contract No. HO220064, ARPA Order No. 1579, Amendment 3 (Program Code 2F10). Inclusive dates for this reporting period are 5 May 1972 through 30 April 1973. The Project Officer was Frank Ruskey. The Principal Investigator was Philip L. Jackson. The Environmental Research Institute of Michigan number for this report is 191700-8-F.

The scientists who contributed to this project throughout the contract period are Ben Drake, Robert Vincent and Thomas Wagner. Vincent was primarily responsible for developing the ratio technique for geologic and lithologic problems, Wagner for soils analysis, and Drake for the geologic background and interpretation. Jackson was responsible for the overall coordination of the project. The work reported commenced in April 1971, under Contract No. HO220041, ARPA Order No. 1579, Amendment 2, Program Code 1F10. This earlier work was reported in Willow Run Laboratories Report 10018-13-F.

CONTENTS

Preface	3
List of Illustrations	6
List of Tables	8
1. Introduction	9
2. General Considerations of Remote Sensing for Tunnel Site Selection	11
3. Geologic Outline of the Northern Black Hills	13
4. Ratio Gating Logic Recognition Maps Produced from Analog Ratio Images	17
4.1 Description of the RAGAL Procedure	18
4.2 Experimental Results	19
4.3 Comparison of Traditional Multispectral Recognition with Ratio Gating Logic	38
4.4 Discussion and Conclusions	45
5. Discrimination of Compositional Differences by the Ratio Method	47
5.1 Definition of the Basis for Discrimination of the Infrared Ratio Among Igneous Silicates	48
5.1.1 Statistical Procedures	53
5.1.2 Correlation of Calculated Ratios with Chemical Parameters	56
5.1.3 Correlation of Calculated Ratios with Mineralogical Parameters	65
5.2 Geologic Applications for the R _{1,2} Infrared Ratio Imaging Method	79
5.3 Conclusions	85
6. Soil Information from Remote Sensor Imagery	87
6.1 Introduction	87
6.1.1 Approach	87
6.1.2 Background	88
6.1.3 A Multispectral System	88
6.1.4 Soil Reflectance	93
6.2 Ratioed Images	94
6.2.1 Munsell Hue	94
6.2.2 Natural Soil Drainage	95
6.2.3 Vegetation Vigor	95
6.2.4 Scene Contrast Suppression	99
6.2.5 Soil Emittance	99
6.3 Multi-Channel Recognition	103
6.4 Toward an Operational System	107
6.4.1 Spectral Variations	110
6.4.2 Conclusions	112
7. Conclusions and Recommendations	113
References	115
Distribution List	118

ILLUSTRATIONS

1. Euclidian Distance Approximation to Ratio Gating Logic	20
2. Location of MSS Flight Line Flown in Northern Black Hills, South Dakota, on May 21, 1972	21
3. Analog Images of Ratios R_{32} , R_{42} , and R_{62} for Flight Section 2A, Near Lead, South Dakota	22
4. Analog Images of Ratios R_{45} , R_{65} , and R_{41} for Flight Section 2A, Near Lead, South Dakota	23
5. Analog Images of Ratios R_{32} , R_{42} , and R_{62} for Flight Section 2B, Near Lead, South Dakota	24
6. Analog Images of Ratios R_{45} , R_{65} , and R_{41} for Flight Section 2B, Near Lead, South Dakota	25
7. Target Categories for Black Hills, South Dakota Data Set	29
8. Ratio Gating Logic Recognition Maps of Vegetative Targets in Flight Section 2A of Black Hills Data	30
9. Ratio Image (R_{32}) and Ratio Gating Logic Recognition Maps of All Non-Vegetation and Water in Flight Section 2A of Black Hills Data	31
10. Ratio Gating Logic Recognition Maps of Geologic Targets in Flight Section 2A of Black Hills Data	32
11. Ratio Gating Logic Recognition Maps of Vegetative Targets in Flight Section 2B of Black Hills Data	33
12. Ratio Image (R_{32}) and Ratio Gating Logic Recognition Maps of All Non-Vegetation and Water in Flight Section 2B of Black Hills Data	34
13. Ratio Gating Logic Recognition Maps of Geologic Targets in Flight Section 2B of Black Hills Data	35
14. Recognition Maps Produced by Statistical Decision Theory with Single-Channel Inputs for Vegetative Targets in Flight Section 2B of Black Hills Data Set	39
15. Recognition Maps Produced by Statistical Decision Theory with Single-Channel Inputs for Geologic Targets in Flight Section 2B of Black Hills Data Set	40
16. Recognition Maps Produced by Statistical Decision Theory with Ratio Inputs for Vegetative Targets in Flight Section 2B of Black Hills Data Set	41
17. Recognition Maps Produced by Statistical Decision Theory with Ratio Inputs for Geologic Targets in Flight Section 2B of Black Hills Data Set	42
18. Infrared Spectra of Igneous Silicate Rocks	49
19. Correlation of $\%SiO_2$ with $R_{1,2}$ for Set A and Set B.	59
20. Correlation of $\%SiO_2 + 5.4 (\%Fe_2O_3)$ with $R_{1,2}$ for Set A.	61
21. Correlation of $\%SiO_2 + 3.7 (\%Fe_2O_2)$ with $R_{1,2}$ for Set B	62

22. Correlation of $^{28}\text{SiO}_2$ - $^{27}\text{Al}_2\text{O}_3$ with $R_{1,2}$ for Set A and Set B	63
23. Mineralogical Parameter M_{16} Versus $R_{1,2}$ for Set C	74
24. Mineralogical Parameter M_6 Versus $R_{1,2}$ for Set C	81
25. Discrimination of Acidic Silicates Near Mill Creek, Oklahoma	83
26. Comparison of Thermal Infrared Ratio Image with an Aerial Photo for a Rhyolitic Tuff (Dark on Ratio Image, Marked by T) Associated with Malachite	84
27. Multispectral Imagery Display	90
28. Maximum and Minimum Radiance for Two Colors of Soil (10 YR and 5 YR)	96
29. Comparison of a Single-Band Video Image with a Ratioed Image	97
30. Enhancement of Natural Soil Drainage	98
31. Comparison of Black and White Panchromatic Photo-Mosaic with a Ratioed Image for Vegetation Vigor Enhancement	100
32. Comparison of a Video Image of Agricultural Land Use with a Ratioed Image of the Same Area	101
33. Blackbody Temperatures Showing the Restrahlen Effect for Mineral Soils in the 8 to 10 μm Wavelength Range	103
34. Comparison of Two Thermal Images with a Ratioed Image of a Soil Test Area Near Weslaco, Texas	104
35. Spectral Distribution of Two Materials and Ratio Decision Boundaries	106
36. Overlapping Spectral Distributions of Two Materials and Likelihood- Ratio Decision Boundary	106
37. Comparison of a Conventional Soil Drainage Map with Soil Recognition Images for Fleming Creek Watershed	108
38. Maximum Likelihood Recognition Map for Soils Signatures Only	109
39. Directional Reflectance of Soil Surfaces	111

TABLES

1. List of Spectral Channels and Ratios Used with the Black Hills Data	26
2. Ratio Ranges of Black Hills Targets	28
3. Evaluation of RAGAL Recognition Maps of the Black Hills Data	36
4. Qualitative Comparison of Recognition Results of Statistical Decision Theory with Ratio Gating Logic.	43
5. Chemical Composition of Igneous Silicate Rock Samples in Weight Percent	52
6. Thermal Infrared Ratios ($R_{1,2}$) Calculated from Laboratory Spectra	54
7. Regression of the C_{12} (Set A) and C_{12} (Set B) Chemical Parameters with $R_{1,2}$	58
8. Normative Minerals	66
9. Computed "Norms" of Set C Rock Samples (Volume %, Incorporating Water).	67
10. Regression of the M_{16} Mineralogical Index with $R_{1,2}$ for Set C	72
11. Reclassification of Rock Samples According to C.I.P.W. Calculations and Travis's Nomenclature.	75
12. Assignment of Group Classifications According to Travis's Nomenclature	76
13. A Classification Based on the M_{16} Mineralogical Index.	78
14. Regression of the M_6 Mineralogical Index with $R_{1,2}$ for Set C	80

GEOLOGIC RECONNAISSANCE AND LITHOLOGIC IDENTIFICATION
BY REMOTE SENSING

FINAL REPORT

5 May 1972 Through 30 April 1973

1

INTRODUCTION

The work during this period was primarily concerned with a test site for geologic remote sensing. After the initial phase, we determined that the most effective contribution would be a test case. The purpose of the test case was to evaluate the usefulness of certain types of remote sensing and data analysis as aids in determining the selection of tunnel sites. In effect, the contribution of remote sensing to tunnel site selection is in our increasing knowledge of geology, lithology, and hydrology (as described in the previous report). The determination of pertinent hydrology by remote sensing can now be considered operational (as illustrated in Section 3.6.1.1 of the previous report). Geology (in terms of tectonics, depositional erosional patterns and ensuing inferences) is the subject of much literature in photogeology and side-looking radar.

Lithology, however, has been the weakest area of remote sensing. Heretofore, there has been no method of discriminating between rock types, except for some research that has been done with low-flying, non-imaging gamma ray sensors. The power of point-by-point image ratioing of multispectral channels for both SiO_2 and Fe_2O_3 content of rocks was shown in section 4.1 of the previous report.

The identification of rock types by remote sensing meant the breaking of new ground and the filling in of a gap in geologic remote sensing. We, therefore, felt that our most useful contributions could be made by extending such identification and by testing in an area which includes many types of geologic structures and lithologies, some of them covered by vegetation. A test site was chosen in the Black Hills of South Dakota, and airborne multispectral scanning data were obtained in May, 1972. Groundtruthing at the time of the flight and after preliminary processing of the data indicated a significant advance in geologic remote sensing.

By ratioing pairs of multispectral images, the following geologic features can be discriminated:

- (1) exposed rock areas
- (2) separate rock groups, including Precambrian quartzite; Precambrian phyllite, slate, and schist; basal quartzite and sandstone; and intrusives such as rhyolite, quartz latite, quartz monzonite, and phonolite

(3) large-scale structures: faults, folds, intrusive bodies, and regional trends.

The form of the analysis output is photo-interpretive, the cost is relatively low, the technique has operational potential because it is relatively simple, and no a priori information is required.

To aid in making the data processing automatic, a gating logic has been developed for the ratioed images. The basis of the logic is to use a known ratio range for a rock type in the preparation of recognition maps. All ratio values which fall into a preset range indicating a given rock type are selected and automatically placed in the location of the rock's occurrence in the scene.

Statistical procedures have been investigated to indicate the probabilities and standard deviations of rock type selections by automatic gating logic. The techniques are based on laboratory measurements which enable statistical determinations and give a firm basis for remote sensing of rock types.

The ratioings for SiO_2 and FeO_2 content have already been described in the previous report. Much of the present report is concerned with establishing theoretical, experimental, and data processing bases for the ratioing technique.

2

GENERAL CONSIDERATIONS IN REMOTE SENSING FOR TUNNEL
SITE SELECTION

The rationale behind remote sensing for tunnel site selection is presented in some detail in the previous report. Also treated are the aspects of geology, lithology, and hydrology which are required for tunnel site selection and for which remote sensing is useful.

During the past two years, remote sensing has advanced technically while, through wide publicity, the potential user has become aware of its possibilities. These advances in technical and information dissemination have come about as a result of the successful experiments of ERTS-1.

The authors feel that it is no longer necessary to describe remote sensing, point out applications, and justify its use for geologic and site-planning purposes. Both the public and private sector have access to ERTS imagery at nominal cost. And though the fact is less well known, the public sector has access to Strategic Air Command synthetic-aperture radar imagery for much of the United States—through Goodyear Aerospace in Litchfield, Arizona. Also, applications committees for synthetic-aperture radar are being formed by NASA for EOS (Earth Observation Satellite) and, for the Space Shuttle, studies of multispectral radar have been made.

In the near future, therefore, photographic, multispectral, and radar imagery will be available to both public and private sectors at nominal cost. Moreover, since the resolution of synthetic-aperture radar imagery is not a function of distance, satellite imagery can be as fine in resolution as airborne imagery.

It is likely that the agency or private contractor responsible for a major construction project such as a deep rock tunnel would use available remote sensing imagery for site selection. In fact, it is the opinion of the authors that within a few years specification for preconstruction geology studies will require the full use of remote sensing imagery and analysis.

The cost of remote sensing is rapidly decreasing for large construction projects. As an example, the Black Hills test case flown over an 80 mi² area in South Dakota by the ERIM MSS aircraft based in Ann Arbor, Michigan, cost \$100 per mi², at 10 ft resolution. In this case, transit costs to South Dakota were shared; otherwise the cost would have been \$150 per mi² for a single flight at this distance from the aircraft home base. The cost per square mile is reduced when the total area is increased.

The commercial rate for synthetic-aperture radar imagery is \$6.00-\$7.00/mi², based on large-area coverage. Specific flights over small areas would increase this cost many times.

Because remote sensing data have become increasingly available in the last two years, we felt that we could make the greatest contribution to geologic remote sensing by acquiring

multispectral scanning data at a test site. Cost restrictions of the contract prevented the funding of a radar flight over the same region.

So, rather than devoting our time to another general analysis and evaluation of remote sensing, this experiment was undertaken with concurrence of the project monitor. We feel fortunate that we were able to make significant advances in the hitherto weakest portion of geologic remote sensing: lithologic identification.

3

GEOLOGIC OUTLINE OF THE NORTHERN BLACK HILLS

The Black Hills of western South Dakota and northeastern Wyoming are an elliptical dome approximately 125 miles long and 60 miles wide that trends approximately N 35° W. The dome actually consists of two nearly flat-topped, steep-sided, probably fault-bounded, uplifted blocks jointed along an approximately north-south lineament passing near the South Dakota-Wyoming border. The eastern block trends approximately north and stands slightly higher than the western block, which trends northwest from the northwestern corner of the eastern block. The higher parts of the Hills rise almost 4000 ft above the surrounding plains.

The Black Hills basically consist of a core of Precambrian igneous and metamorphic rocks exposed over an area 60 miles by 20 miles. Around the core are draped a few thousand feet of Paleozoic sedimentary rocks, which dip off the dome in all directions. The Red Valley, with Lower Mesozoic sedimentary rocks underlying it, completely encircles the uplift. A Cretaceous hogback ridge forms an outer encircling rim. Early Tertiary intrusive rocks occur in a belt across the northern Black Hills.

The Black Hills have undergone two major periods of deformation: Precambrian and early Tertiary, probably Eocene. The Precambrian deformation produced a series of plunging isoclinal folds of various sizes. During or after the closing phases of the Precambrian folding, there were intrusions of granite bodies and diorite and gabbro dikes. Although the granites occur mainly in the southern Black Hills, they are exposed at four localities in the northern Hills. The diorite and gabbro dikes were metamorphosed to amphibolites and metagabbros during the Precambrian deformation; however, Bayley indicates that the amphibolites are metamorphosed lava flows, at least in the Galena-Roubaux district [1]. Noble and Harder suggest that the progressive metamorphism of the rocks in the Lead region is related to an intrusion of unexposed Precambrian igneous rocks [2].

The major structural features of the Black Hills, as well as the present domal form of the Hills, were formed in the early Tertiary during the Laramide Revolution. Whether the Hills were uplifted by vertically acting forces, by laterally compressive forces, or by some combination of the two types is an open question; most geologists favor vertically acting forces. It has

1. Richard W. Bayley, *Structure and Mineralization of Precambrian Rocks in the Galena-Roubaux District, Black Hills, South Dakota*, USGS Bull. 1312-E, 1970. 15pp.

2. J. A. Noble and J. O. Harder, *Stratigraphy and Metamorphism in a Part of the Northern Black Hills and the Homestake Mine, Lead, South Dakota*, Geol. Soc. Amer. Bull. V. 59, 1948, pp. 941-976.

been postulated that a Tertiary batholith underlies the northern Black Hills, if not the entire Hills area, and is responsible for the uplift [3, 4].

Several secondary structural features which probably formed at the time of the major uplift are superimposed on the general domal structure. These include the following.

(1) Sharp steep monoclinal flexures in the sedimentary rocks, especially at the western edges of the uplifted blocks and along the lineament at which the two domal blocks are joined [5]. The sedimentary strata are nearly horizontal on top of the dome (except where affected by emplacement of the Tertiary intrusive rocks), but they form monoclines as they dip off the Black Hills, probably as a result of draping over steep deep-seated faults. In general, the beds on the western margins of the blocks dip more steeply than those on the eastern edges.

(2) Small to moderate-size igneous intrusive bodies.

(3) Plunging anticlinal folds, mainly at the north ends of both blocks but also at the southern end of the eastern block. These plunging folds may be caused by intrusive bodies or by movements along secondary faults.

Tertiary intrusive igneous bodies occur in a zone 15 to 20 miles wide extending N 70-75° W across the northern Black Hills from the Bear Lodge Mountains to Bear Butte. Superimposed on both domal blocks, these intrusives consist of relatively minor dikes and sills, as well as larger, much more important intrusives (roughly circular to slightly elongated) that range from less than a mile to about 10 miles in diameter. It is thought that the larger intrusives were forcibly injected; some consider them mainly laccoliths, others describe them as mainly steep-sided stocks with concordant upper surfaces. The larger intrusives folded and/or faulted the Precambrian-to-Tertiary rocks that they intruded, creating a series of domes that have cores of Tertiary intrusive rocks. One of the domes of the northern Black Hills is the Lead-Deadwood dome. It is about 12 miles by 10 miles, the longer dimension extending in a westerly direction. Near the center of the dome stands a very ragged stock, the Cutting Stock, about 2 by 4 miles. There are also several other smaller stocks and vast numbers of large and small dikes in the northern Black Hills.

3. N. H. Darton and S. Paige, Central Black Hills Folio (219), USGS Geologic Atlas, 1925, 35pp.

4. J. A. Noble, J. O. Harder, and A. L. Slaughter, Structure of a Part of the Northern Black Hills and the Homestake Mine, Lead, South Dakota, Geol. Soc. Amer. Bull. V. 60, 1949, pp. 321-352.

5. L. H. Shapiro and J. P. Gries, Ore Deposits in Rocks of Paleozoic and Tertiary Age of the Northern Black Hills, South Dakota, USGS Heavy Metals Program, Contract No. 14-08-0001-10650, 1970, 235pp.

R. W. Bayley of the U.S. Geological Survey has just finished a seven-year mapping project (1965-1972) in which he revised the Precambrian geology of the northern Black Hills. The results of his mapping are available as an open file map and two publications [1, 6]. Except for the Lead region, the Precambrian geology of the northern Black Hills generally was not well known before Bayley's mapping. Bayley has made the only overall correlation of Precambrian rocks in different parts of the northern Hills, although some correlations between different districts had been done previously.

Bayley's recent mapping in the northern Black Hills has shown that the Precambrian rock types present include granite, graywacke, slate, phyllite, schists, chert, quartzite, conglomerate, arkose, limestone, banded iron formation (taconite), metagabbro and/or amphibolite, and metabasalt. Three well-defined zones of metamorphism in the Precambrian rocks of the Lead region, which have been described by Noble and Harder [2], have an increasing degree of metamorphism from southwest to northeast.

The sedimentary rocks in the northern Black Hills mainly range in age from Late Cambrian to Early Cretaceous, but some are as young as Tertiary. The Phanerozoic formations consist of sandstone and quartzite, shale, limestone, dolomite, siltstone, clays, conglomerate, and some thin coal seams.

At many places around the eastern side of the northern Black Hills (and in scattered localities in the Hills) are deposits of the Middle Oligocene White River Group laid down by streams after the uplift of the Black Hills. These deposits are erosional remnants of a former wide-spread mantle of sand and coarse gravel underlain in places by fuller's earth and clay. Also around the northern Black Hills are different levels of Quaternary sand, gravel, and loam terrace deposits. Quaternary alluvium occurs in the major, wider stream valleys both in and around these northern Hills.

Tertiary acidic volcanics, probably Eocene in age, are found in at least four general areas in the northern Hills.

No comprehensive study has been done of the petrology and petrography of the Tertiary intrusives in the northern Black Hills. Identified intrusive rock types include rhyolite, quartz latite, monzonite, quartz monzonite, phonolite, and granodiorite — porphyries of these intrusive

6. Richard W. Bayley, Preliminary Geologic Map of the Nemo District, Black Hills, South Dakota, Misc. Geologic Investigations, Map I-712, 1972.

types are common. There seem to be gradations from one type to another. Most of the larger intrusives are multiple intrusions of several different types of rock; and it seems safe to say that most of the multiple intrusion bodies have not been mapped correctly.

The structural geology of the northern Black Hills is known in detail only for scattered localities where there has been concentrated mapping, such as Lead, Rochford, the Nemo district, and the Galena-Roubaix district. It is known that there is a series of large, isoclinal anticlines and synclines with smaller isoclinal folds on their limbs in the Precambrian rocks of the northern Black Hills, and that all these folds were formed during the Precambrian deformation. These large folds generally trend north to northwest and their limbs dip steeply northeast; the folds plunge at angles that are gentle to almost vertical. Sinuous refolded isoclinal folds (cross folds) occur in several regions of the northern Hills. The age of the cross folding is not known; it might be early Tertiary instead of Precambrian. Slaughter believes that the structural effects of the injection of Tertiary intrusive rocks were very important [7].

Bayley's mapping has shown the presence of several large generally northwest-trending, right-lateral, strike-slip faults. Major normal faults also have been mapped, as well as relatively few reverse faults; these reverse faults generally merge into other types of faults.

7. A. L. Slaughter, The Homestake Mine: Ore Deposits in the United States 1933-1967, AIME, 1968, pp. 1436-1459.

RATIO GATING LOGIC RECOGNITION MAPS PRODUCED FROM ANALOG RATIO IMAGES

Ratio images employed for the first time two years ago under a NASA task have been found useful for geological remote sensing [8-12]. Ratio images are useful because they (1) enhance the contrast between targets which have intersecting spectral reflectance curves; (2) suppress or reduce illumination variations across the scene; and (3) display spectral data from all points in the scene before automatic classifications have been made that result in some areas being classified "unrecognized." In addition, they are relatively simple for the photointerpreter to use—because of their similar appearance to aerial photos and the relative ease by which they can be qualitatively related to laboratory spectra. Ratio images also maintain the advantages of a multispectral scanner in that they have greater spectral range, are easier to process quantitatively, and require less mosaicking than aerial photos.

There are still needs, however, for recognition maps in geological remote sensing. Originally, the ratio gating logic described in this section was created simply to enable the geological user to produce recognition maps of some targets without having to forfeit the processing time already invested in producing the ratio images. Traditional analog multispectral recognition methods utilizing likelihood-ratio, statistical, decision-theory require several things before recognition maps are produced: a description of training sets (including location and spectral characteristics) by the user to a SPARC operator; the preparation of magnetic tape loops; and training of the SPARC computer on the training sets. In short, the user of ratio images would have to start from scratch to produce analog recognition maps in this manner. In the course of this investigation, however, several advantages of the ratio gating logic over the traditional multispectral recognition method have become more obvious, so this rather

8. R. K. Vincent, R. Horvath, F. Thomson, and E. Work, Remote Sensing Data-Analysis Projects Associated with the NASA Earth Resources Spectral Information System, The University of Michigan, Report No. 3165-77-T, NASA Contract NAS9-9784, 1972.

9. R. K. Vincent and F. Thomson, Spectral Compositional Imaging of Silicate Rocks, J. of Geophys. Res., Vol. 77, 1972, pp. 2465-2471.

10. R. K. Vincent, Rock-Type Discrimination from Ratio Images of the Pisgah Crater, California Test Site, The University of Michigan, Report No. 3165-77-T, NASA Contract NAS9-9784, 1972.

11. R. K. Vincent, F. Thomson, and K. Watson, Recognition of Exposed Quartz Sand and Sandstone by Two-Channel Infrared Imagery, J. of Geophys. Res., Vol. 77, 1972, pp. 2473-2477.

12. R. K. Vincent and F. Thomson, Rock Type Discrimination from Ratioed Infrared Scanner Images of Pisgah Crater, California, Science, Vol. 175, 1972, pp. 986-988.

simple technique has taken on greater significance. Although it theoretically cannot be as powerful an automatic decision-making method as the more complex statistical ones, its advantages outweigh the costs in decision making for those remote sensing problems characterized by relatively high spectral contrasts either among several targets of interest or between targets and background.

In Section 4.1, the recognition procedure involving ratio gating logic (hereinafter called RAGAL) will be described, followed in Section 4.2 by the experimental results from its first application to scanner data. In Section 4.3, traditional multispectral recognition results will be given and compared with RAGAL results. Finally, in the discussion and conclusions section (4.4), the advantages and disadvantages of the RAGAL procedure will be listed, along with suggestions for future improvement.

4.1 DESCRIPTION OF THE RAGAL PROCEDURE

Analog ratio images are produced by inputting signals from two channels of a multispectral scanner into an analog computer, which first modifies the signal voltage in each channel to be directly proportional to detected radiance and then divides the voltage of one channel by that of the other. The resulting ratio voltage, which is directly proportional to the ratio of radiances detected in the two channels, is then fed to a glow tube that scans over a moving strip of photographic film. Film density on the resulting photographic print is a direct function of the ratio of radiances in the two channels of interest. A gray-scale is printed with each ratio image to enable the user to relate film density to voltage, which is proportional to the ratio. Whenever ratio images are produced, the electronic settings required on the SPARC ratio processor are recorded, so that their reproduction at a later time is possible.

The user can treat ratio images as an end product in themselves. The RAGAL method is designed, however, to permit the user to make recognition maps based on the ratio images, if he so desires. If the user defines "m" training sets and has "n" ratio images, he must determine "n" voltage ranges for each of the "m" training sets. A training set can consist of any area in the ratio image or, if RAGAL can be developed to its final intended form, of a group of laboratory spectra. At the present time, only the former type of training set has been implemented.

Once a target of interest has been defined in the ratio imagery, the user determines the target voltage range for each of the "n" ratio images by comparing the film density over the target area with the corresponding gray-scale for each ratio. This can be accomplished either by visual examination or, more accurately, by a photodensitometer. The resulting set of voltage ranges for each target is communicated to the SPARC operator, who first reproduces the original electronic settings used to construct the ratio images and then creates a series of

AND gates on the SPARC. There is an AND gate for each of the "n" ratios, with the upper and lower voltage (proportional to radiance ratio) values on each gate defined by the voltage ranges of a given target. For any point in the scene to be recognized as that target, the ratios of that point must fall within the limits of every one of the AND gates. All points meeting these criteria are printed as white, and all non-target points are printed black. The AND gates are reset for each different target. Since statistical likelihood ratio decision rules are not used, there can be regions of target overlap — an area in the scene can be recognized as more than one target. However, with RAGAL there is no limit to the number of targets that can be attempted because each target is independent. On the other hand, SPARC can implement the statistical likelihood ratio decision rule only for a maximum of $\frac{48}{n}$ interdependent targets, where "n" is the number of input channels.

It was not possible to implement RAGAL exactly as desired on the SPARC computer because, in its present configuration, SPARC is not capable of simple gating. Therefore, a Euclidian distance criterion was used which approximates the gating logic. For a given mean voltage and given variance in a single input channel, the Euclidian distance rule weights the voltage from a given point in the scene according to its deviation from the mean voltage. Therefore, an approximation to the ratio gate voltages was made by the mean voltage (the average of the upper and lower ratio voltage limits) and a variance that was 1.5 times the difference between the mean and lower (or upper) limit voltages. Figure 1 is a schematic example of this approximation.

4.2 EXPERIMENTAL RESULTS

The preliminary testing of RAGAL has been with a data set from a region northwest of Rapid City, in the northern Black Hills of South Dakota. Data from this region were collected by the ERIM C-47 aircraft for the U.S. Bureau of Mines on May 21, 1972 beginning at approximately 9 A.M. Mountain Daylight Time. Altitude was 5000 ft above terrain. The sky was free of clouds, but a low haze was present throughout the flightline, which was about 24 mi in length and 2 mi (see Fig. 2) in width. Only visible and reflective-IR scanner channels were ratioed because of a malfunction in the two-element thermal detector used for ${}^{\circ}\text{SiO}_2$ and ${}^{\circ}(\text{SiO}_2\text{-Al}_2\text{O}_3)$ discrimination (see Section 5 of this report).

Figures 3 and 4 show six ratio images of flightline section 2A over Lead, South Dakota. Figures 5 and 6 show the same ratio images for section 2B, the second half of that flightline. North is approximately to the upper left corner in each figure. The six spectral channels used for these ratios are given in Table 1, where R_{ij} represents the radiance in the i-th channel divided by the radiance in the j-th channel. Considerable information is available from the ratio images alone. However, in this report the topic of interest is computer target recognition, which in the future may become a truly automatic function.

$$\text{Variance} = 1.5(V_u - V_m) \left\{ \begin{array}{l} \text{-----} V_m + 1.5(V_u - V_m) \\ \text{—————} V_u = \text{Desired Upper Voltage Limit} \\ \text{.....} V_m = \text{Mean Voltage} \\ \text{—————} V_l = \text{Desired Lower Voltage Limit} \\ \text{-----} V_m - 1.5(V_u - V_m) \end{array} \right.$$

FIGURE 1. EUCLIDIAN DISTANCE APPROXIMATION TO RATIO GATING LOGIC

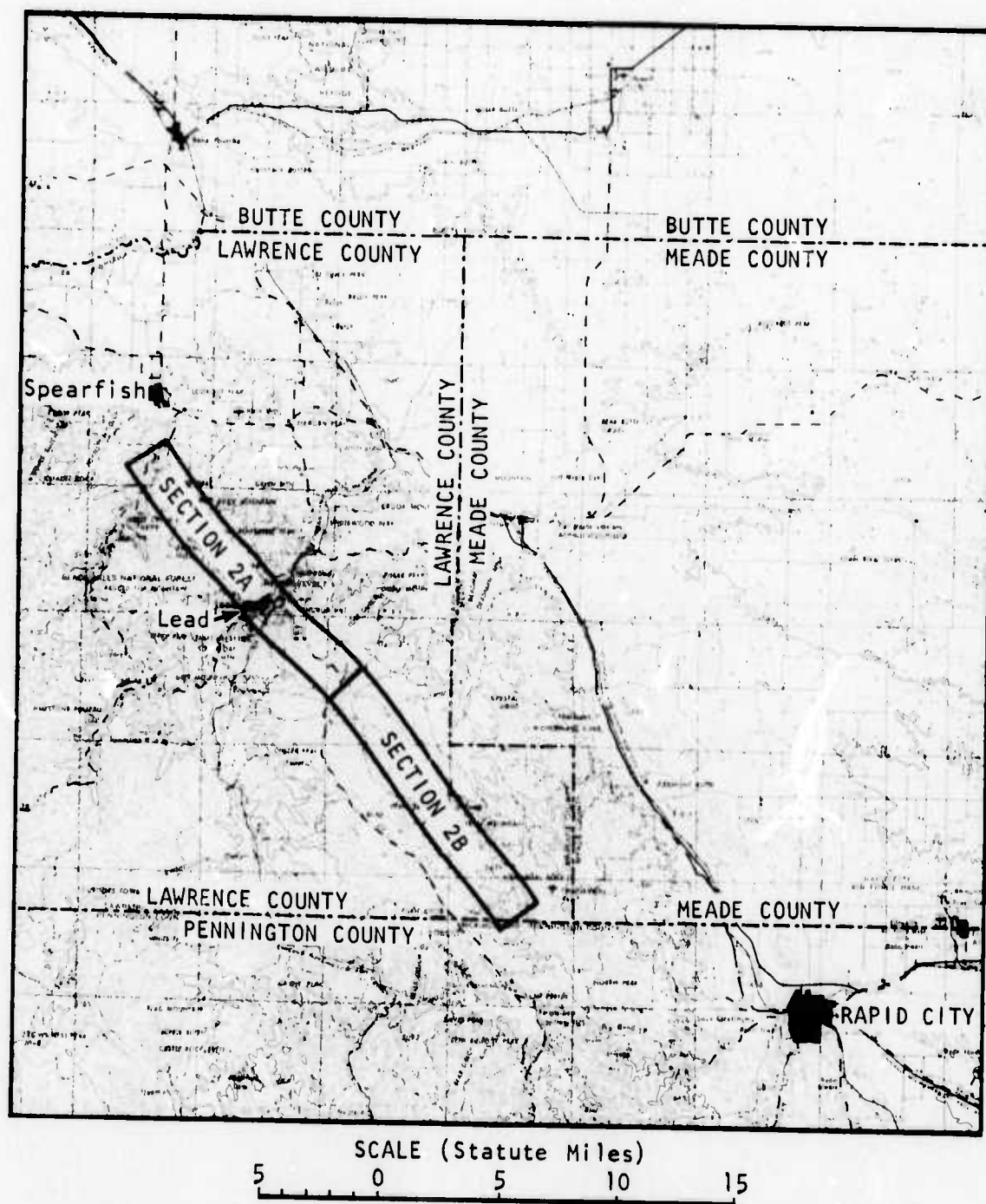


FIGURE 2. LOCATION OF MSS FLIGHT LINE FLOWN IN NORTHERN BLACK HILLS, SOUTH DAKOTA, ON MAY 21, 1972. Sections 2A and 2B of the flightline are both shown.

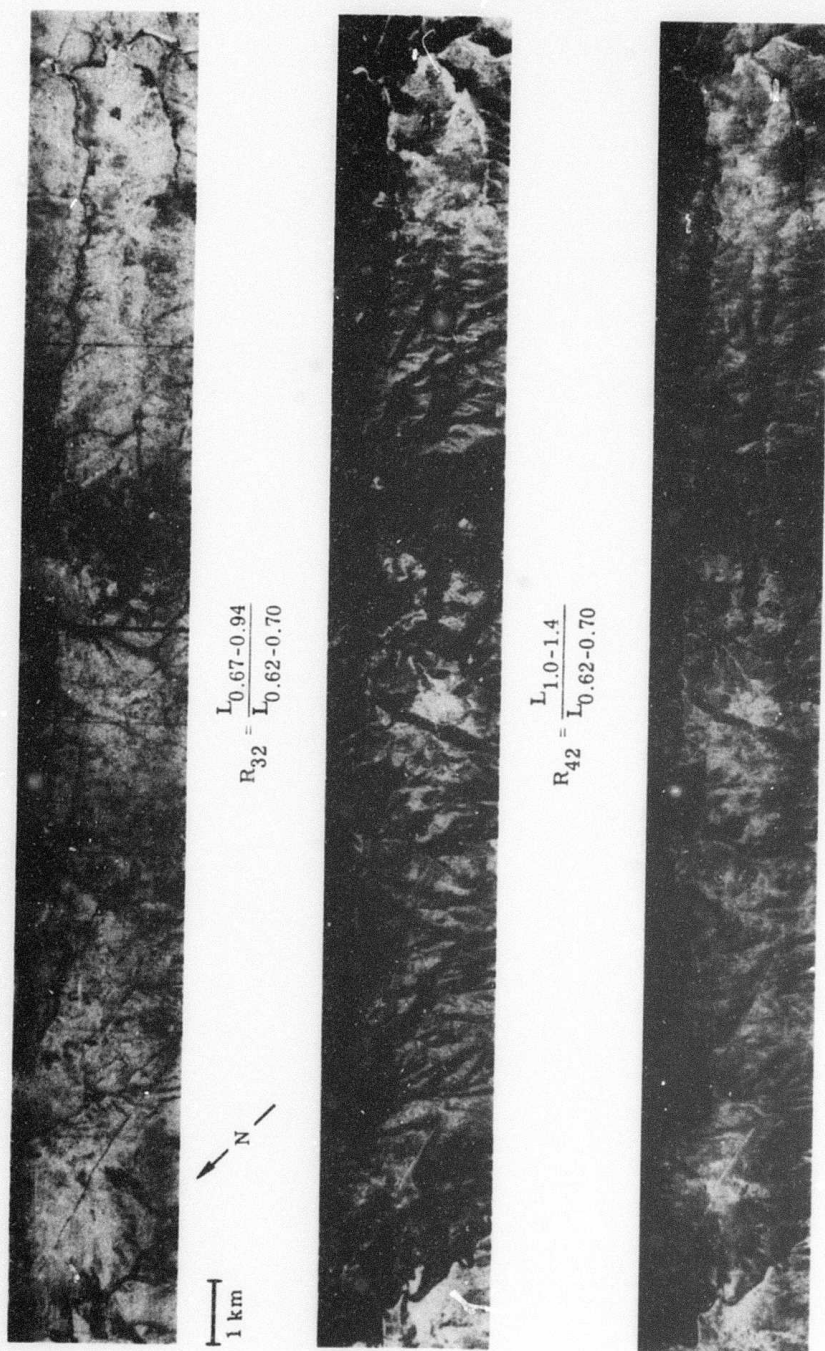


FIGURE 3. ANALOG IMAGES OF RATIOS R_{32} , R_{42} , AND R_{62} FOR FLIGHT SECTION 2A, NEAR LEAD, SOUTH DAKOTA

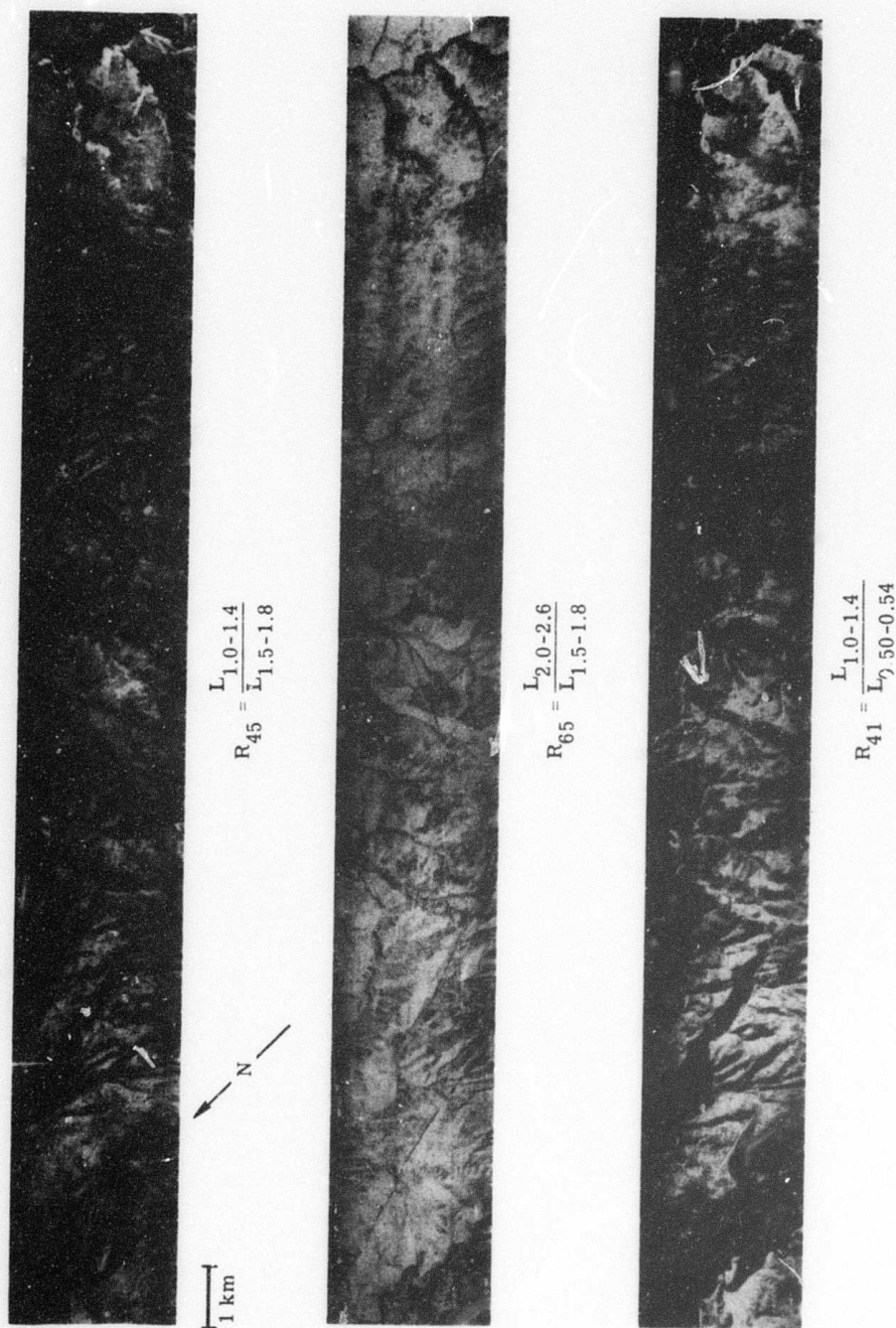


FIGURE 4. ANALOG IMAGES OF RATIOS R_{45} , R_{65} , AND R_{41} FOR FLIGHT SECTION 2A, NEAR LEAD, SOUTH DAKOTA

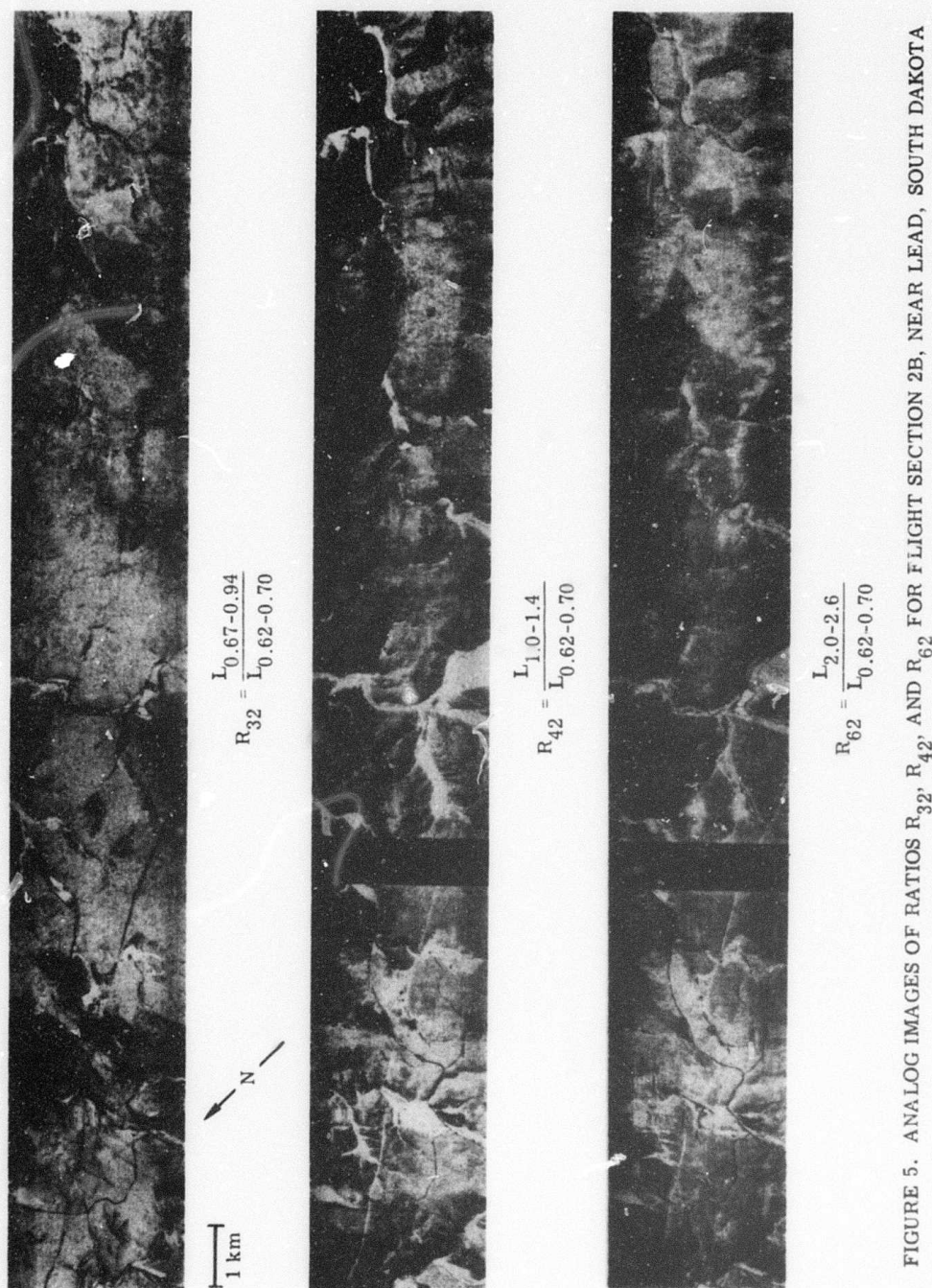


FIGURE 5. ANALOG IMAGES OF RATIOS R_{32} , R_{42} , AND R_{62} FOR FLIGHT SECTION 2B, NEAR LEAD, SOUTH DAKOTA

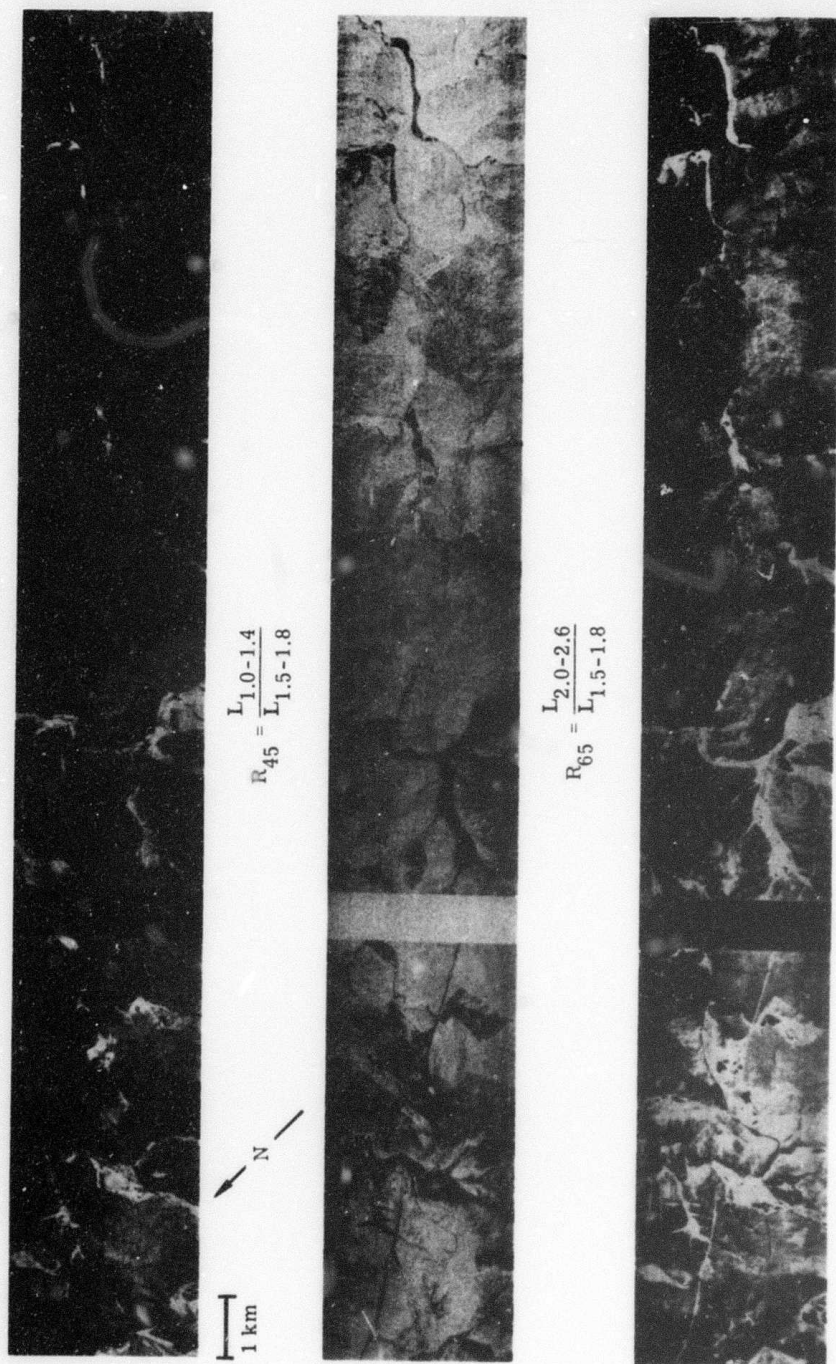


FIGURE 6. ANALOG IMAGES OF RATIOS R_{45} , R_{65} , AND R_{41} FOR FLIGHT SECTION 2B, NEAR LEAD, SOUTH DAKOTA

TABLE 1. LIST OF SPECTRAL CHANNELS AND RATIOS USED WITH THE BLACK HILLS DATA

Single Channel No.	Wavelength Region (μm)	Ratios Including that Channel
1	.50-.54	R_{41}
2	.62-.70	R_{32}, R_{42}, R_{62}
3	.67-.94	R_{32}
4	1.0-1.4	R_{41}, R_{42}, R_{45}
5	1.5-1.8	R_{45}, R_{65}
6	2.0-2.6	R_{62}, R_{65}

Figure 7 is a flow chart describing the attempted final categorization of targets in the Black Hills data. The extremum ratio ranges for each of these targets are given in Table 2. On the basis of the listed number of test areas given in the last column, these are the target classifications which appear to be uniquely discriminable from one another. Other target classifications were examined, but their ratio ranges were found to overlap the ranges of other targets. For instance, an effort was made to subcategorize the igneous intrusives into rhyolite, quartz latite, and phonolite; but they overlapped each other enough to force them into a single, more general category.

RAGAL recognition maps of the 10 targets listed in Table 2 are shown in Figs. 8 through 10 for flightline section 2A; for section 2B, they are shown in Figs. 11 through 13. The top-most image strips in Figs. 8 and 11 are R_{32} ratio images of sections 2A and 2B, respectively, upon which the test sites enumerated in Table 2 have been indicated. For instance, there are five vigorous-range-grass targets labeled "1," five quartzite targets labeled "7," etc. on sections 2A and 2B combined. Target 5, all non-vegetation, was a simple one-ratio threshold process for which no specific training set was used. That R_{32} threshold, 2.2 volts, was selected on the basis of data in the first column of Table 2, in which a natural separation occurs between vegetative and non-vegetative targets at 2.2 volts.

Three types of experimental artifacts must be pointed out. First, the dark vertical regions in all of the section-2B recognition maps and ratio images including the ratios R_{42} , R_{62} , R_{45} , R_{65} , and R_{41} were caused by a temporary failure of the three-element detector responsible for spectral channels 4, 5, and 6. Second, in R_{41} ratio images and vigorous-range-grass (target 1) recognition maps of both flightline sections, some areas of the vigorous range grass are brighter than the brightest gray-scale level of ratio R_{41} . This is typified in R_{41} ratio images by black regions and in the target 1 recognition map as unidentified (black) vigorous-range-grass test sites. Only the most vigorous grasses were unrecognized in this manner, however. This problem is trivial and can be corrected in future applications of RAGAL. Third, there is some noise in the target-1 recognition map of section 2A (white vertical streaks) caused by non-recurring tape recorder noise while the recognition map was being generated.

In addition to the above errors, the reader is again reminded that the human eye was used to determine voltages from the ratio image gray-scales, and that the gating logic was approximated by a Euclidian distance method. The former, which was probably accurate only to approximately ± 0.2 volt (with a bias toward wider ratio ranges so the target cannot be missed), can be greatly improved with a photodensitometer. The latter error, which is impossible to estimate, can be corrected by building a cheap AND-gate processor to replace the SPARC logic for RAGAL application.

A brief evaluation of each of the 10 target recognition maps is given in Table 3. The worst recognition occurred for targets 1, 4, and 10. The target-1, vigorous-range-grass errors are

TABLE 2. RATIO RANGES OF BLACK HILLS TARGETS

Target No.	Target Name	Ratio Voltage Limits (Volts)						No. of Test Areas
		R ₃₂	R ₄₂	R ₆₂	R ₄₅	R ₆₅	R ₄₁	
1	Vigorous Range Grass	6.6-7.0	4.9-5.3	3.7-4.3	4.1-4.7	2.9-3.5	5.3-5.5	5
2	Dormant and Low Vegetation	2.2-3.4	2.0-3.0	2.4-2.8	2.3-3.1	3.5-4.3	3.5-4.3	7
3	Conifer Trees	4.3-5.9	2.7-3.7	2.6-3.6	3.5-4.5	2.7-3.5	3.6-4.4	3
4	Deciduous Trees	3.0-4.2	2.6-3.6	2.9-3.9	2.3-3.1	3.4-4.2	3.7-4.5	1
5	All Non-Vegetation	0.6-2.2	-	-	-	-	-	-
6	Water	0.6-2.2	0.2-0.8	0.5-2.5	1.4-2.8	0.8-3.4	0.9-2.3	4
7	Quartzite	0.6-2.2	0.4-2.0	2.4-2.8	1.3-2.1	3.7-4.9	0.7-1.9	5
8	Slate, Phyllite, Schist	0.6-1.4	0.5-1.3	0.4-1.4	1.5-2.7	3.7-5.5	0.8-3.0	5
9	Igneous Intrusives (Rhyolite, Quartz Latite, & Phonolite)	0.7-1.3	1.0-1.2	2.0-3.0	1.3-1.9	4.7-5.5	2.2-2.6	7
10	Deadwood Sandstone	0.6-2.2	1.7-1.8	2.2-2.7	2.0-2.5	4.3-5.5	3.0-3.2	2

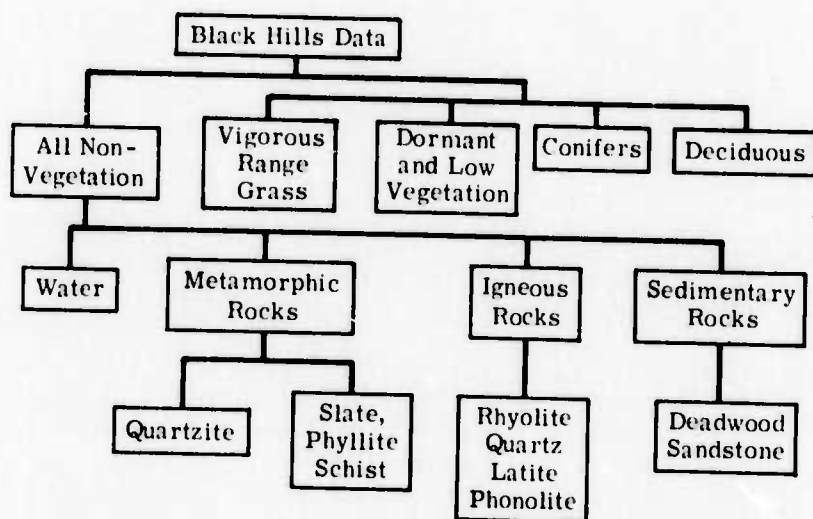


FIGURE 7. TARGET CATEGORIES FOR BLACK HILLS, SOUTH DAKOTA DATA SET

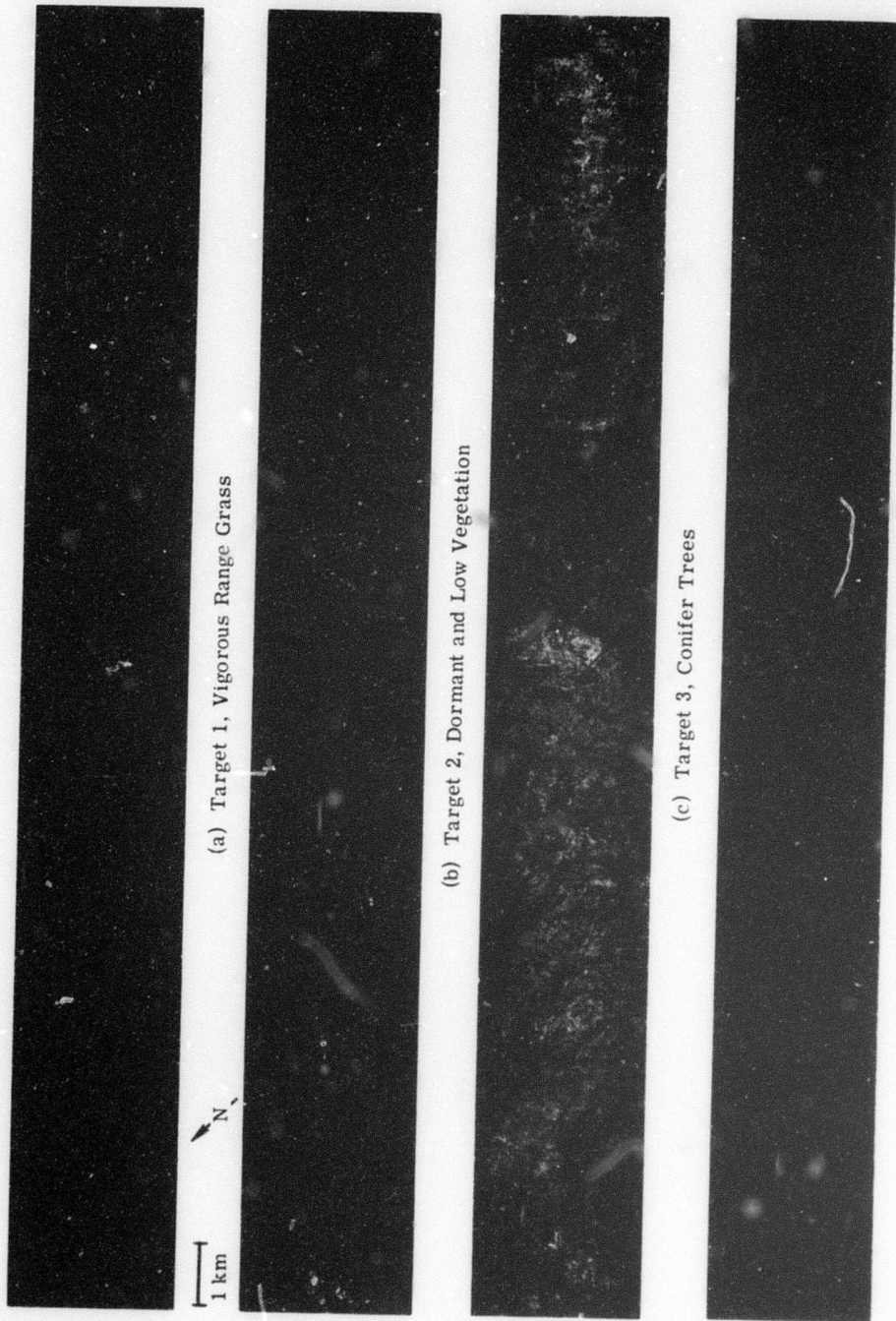


FIGURE 8. RATIO GATING LOGIC RECOGNITION MAPS OF VEGETATIVE TARGETS IN FLIGHT SECTION 2A OF BLACK HILLS DATA

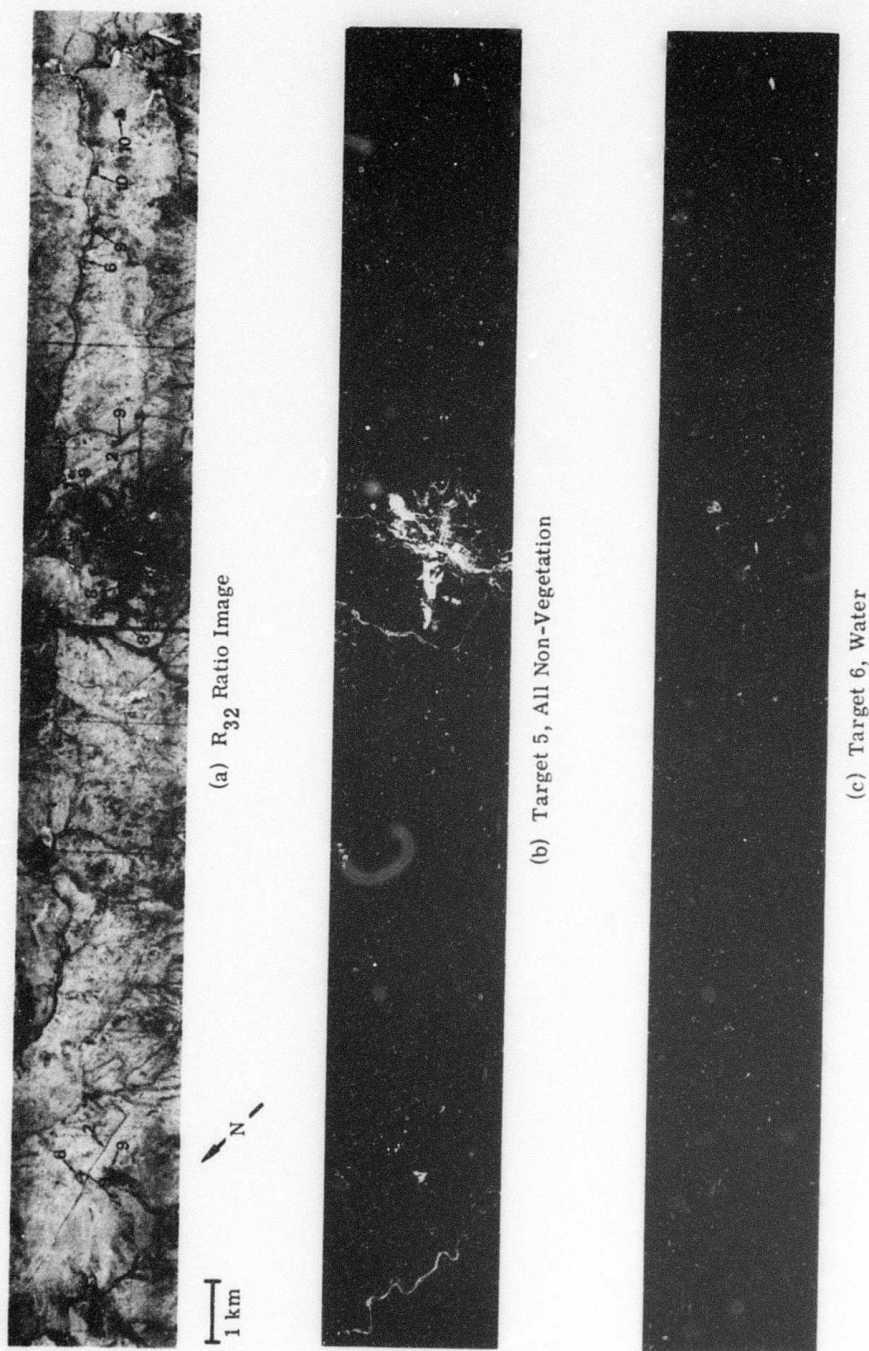


FIGURE 9. RATIO IMAGE (R_{32}) AND RATIO GATING LOGIC RECOGNITION MAPS OF ALL NON-VEGETATION AND WATER IN FLIGHT SECTION 2A OF BLACK HILLS DATA

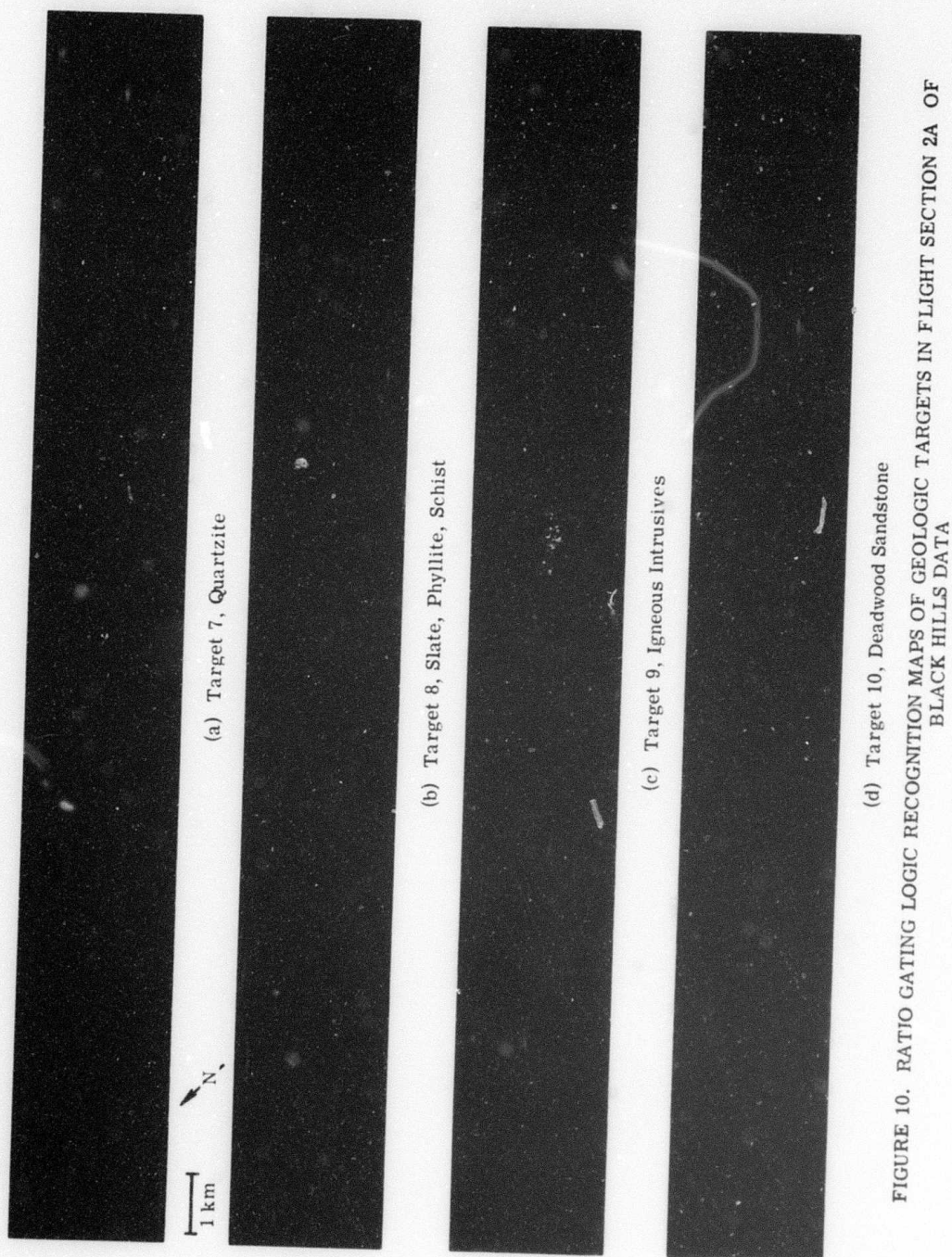


FIGURE 10. RATIO GATING LOGIC RECOGNITION MAPS OF GEOLOGIC TARGETS IN FLIGHT SECTION 2A OF BLACK HILLS DATA

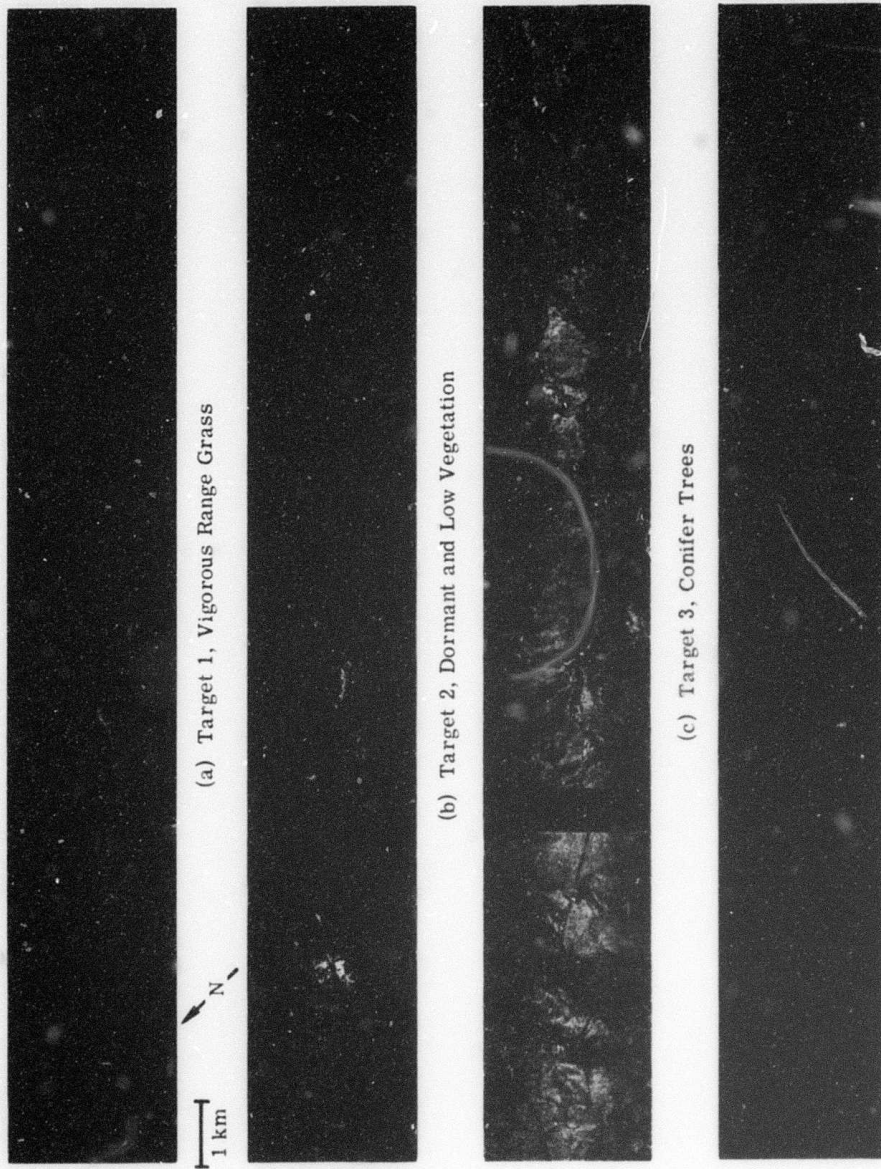


FIGURE 11. RATIO GATING LOGIC RECOGNITION MAPS OF VEGETATIVE TARGETS IN FLIGHT SECTION 2B OF BLACK HILLS DATA

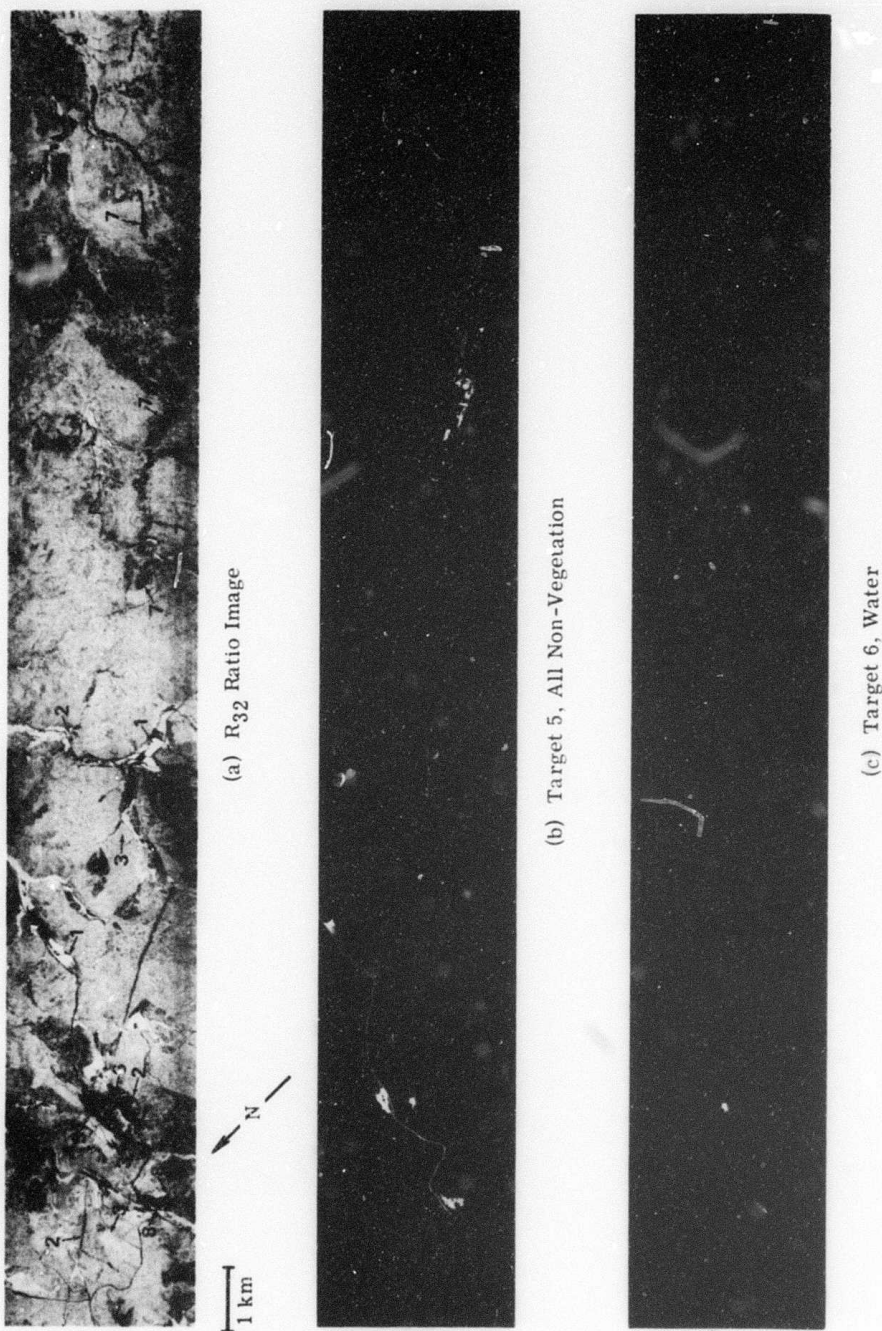


FIGURE 12. RATIO IMAGE (R_{32}) AND RATIO GATING LOGIC RECOGNITION MAPS OF ALL NON-VEGETATION AND WATER IN FLIGHT SECTION 2B OF BLACK HILLS DATA

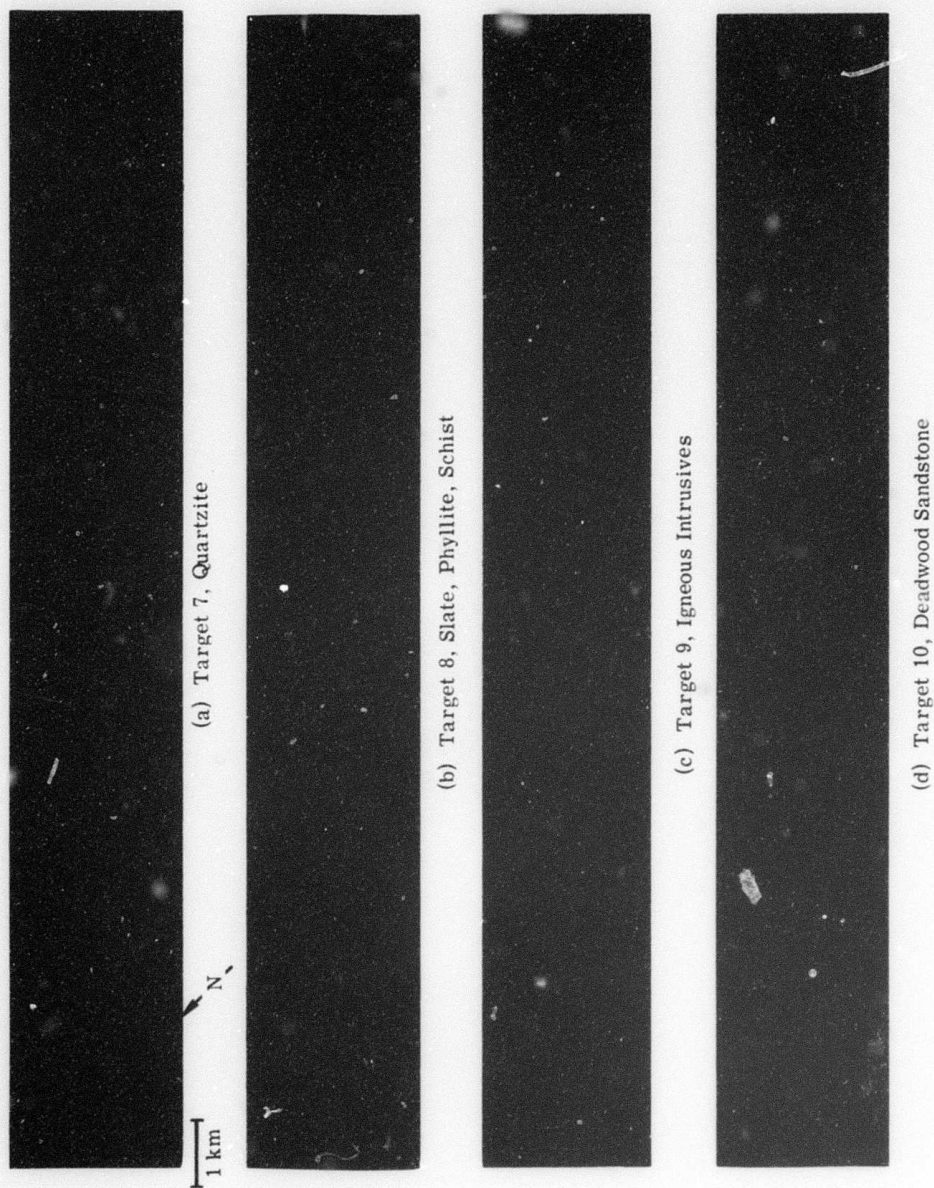


FIGURE 13. RATIO GATING LOGIC RECOGNITION MAPS OF GEOLOGIC TARGETS IN FLIGHT SECTION 2B OF BLACK HILLS DATA

TABLE 3. EVALUATION OF RAGAL RECOGNITION MAPS OF THE BLACK HILLS DATA

Target No.	Target Name	Comments
1	Vigorous Range Grass	Failed to recognize 2 of available 4 test sites (one in the noisy region of section 2B) and all other very vigorous grass because the R41 ratio for these targets exceeded the maximum grey-scale value. This problem is easily correctible. Rest of vigorous grass recognized appears consistent with air photos, except for appreciable overlap with target 14, conifers.
2	Dormant and Low Vegetation	All of the 7 test sites were at least partially recognized. There is slight overlap with rocks ($\approx 5\%$) in sec. 2A and some overlap ($\approx 10\%$) with deciduous trees in sec. 2B. The latter is understandable, since much of the low vegetation and deciduous trees characteristically have broad leaves.
3	Conifer Trees	Recognized at least 70 to 80% of all conifers (including all 3 test sites), but including some vigorous grass ($\approx 15\%$), deciduous ($\approx 5\%$) and dormant vegetation ($\approx 5\%$). Missed conifers are mostly on northern slopes, caused by vegetative differences on slopes and some possible shadowing or bidirectional effects. Ratio ranges could be narrowed and tightened by 10% or more.
4	Deciduous Trees	Difficult to evaluate, because of lack of ground truth concerning deciduous trees. Did not recognize only test site. Some overlap ($\approx 10\%$) with dormant and low vegetation, some of which may be real. Deciduous trees near quartzite outcroppings are fairly accurate.
5	All Non-Vegetation	Excellent recognition (better than 95% accurate) with less than 5% false alarms, caused by some dormant vegetation.

TABLE 3. EVALUATION OF RAGAL RECOGNITION MAPS OF THE BLACK HILLS DATA (Concluded)

Target No.	Target Name	Comments
6	Water	Recognized 3 test sites well and one (shallow beaver pond) only partially. Also includes almost all of slate, phyllite, schist targets (no.8), but no other targets. All bodies of water deeper than about 10 feet are correctly recognized, including portions of streams.
7	Quartzite	Recognized all 5 test sites and appears to be about 90% accurate. Some overlap with igneous intrusives in section 2A.
8	Slate, Phyllite, Schist	Recognized 4 test sites well and one partially, but appears to be quite accurate. Includes some roads and some overlap in rhyolite quarry of section 2B, but this quarry <u>did</u> contain some schist outcrops in it.
9	Igneous Intrusives (Rhyolite, Quartz Latite, and Phonolite)	Recognized 3 test sites well, 2 partially, and missed 2. Includes almost all roads (which most likely are built with rhyolite and quartz latite), most of deadwood sandstone (target 10); some overlap with quartzite and slate, phyllite, schist.
10	Deadwood Sandstone	Missed both test sites and includes only some dormant vegetation.

understood, however, and can easily be corrected (as explained earlier). Errors in target 1 (deadwood sandstone) are understandable in that the ratio ranges in R_{42} and R_{41} for that target are very narrow (0.1 and 0.2 volt, respectively), well within the experimental error (roughly ± 0.2 volt of the mean voltages) of this investigation. Errors in target 4 are the most difficult to assess because of the small amount of ground truth available for deciduous trees and the realistic overlap between deciduous trees and broad-leaf low vegetation (part of target 2). Recognition of both targets 4 and 10 can be considerably improved by the use of a photodensitometer and a more exact implementation of the ratio gating logic, without the Euclidian distance approximation.

The target-5 recognition map, the best one produced, was accomplished by thresholding a single ratio, R_{32} . In fact, Table 2 indicates that a simple thresholding of ratio R_{32} may be sufficient to discriminate among targets 1, 3, 5, and a combined target of 2 and 4. This will be pursued further in the next RAGAL investigation. Other recognition maps which appear to be good are those for targets 2, 7, and 8. Recognition maps for targets 3 and 6 were downgraded mostly by false alarms, which in both cases were primarily targets that had been recognized in other recognition maps.

4.3 COMPARISON OF TRADITIONAL MULTISPECTRAL RECOGNITION WITH RATIO GATING LOGIC

In order to compare RAGAL results with traditional analog multispectral recognition techniques, recognition maps of six targets were produced for flightline section 2B, with the statistical likelihood ratio decision rule. Magnetic tape belt loops (containing the training sets) were prepared for each of the six targets in lieu of using the ratio images. The SPARC operator then recorded the input voltages for each input channel over each test site. Two sets of recognition maps were made in this manner, one with single-channel radiances as inputs and the other with ratio inputs (ratio preprocessing). Figures 14 and 15 show the results of using the single channels of Table 1 as inputs. Figures 16 and 17 show the results of using ratio inputs, the same ones used for the RAGAL procedure. Table 4 gives a comparison of the three results for each of the six common targets. Since some of the training sites (tape loops) are in flightline section 2A, it is possible for a target to be absent completely—as in the slate, phyllite, schist case (target 8). The training sets used were common to all three types of recognition maps, except for dormant and low vegetation (target 2), which were different for the RAGAL maps.

It is clear from Table 3 that the statistical decision theory with single-channel inputs is inferior to the other two methods. This indicates that ratio preprocessing and ratio imaging significantly reduce the effect of unwanted environmental factors, such as shadowing, illumination, and scan angle variations. The statistical decision theory with ratio preprocessing was

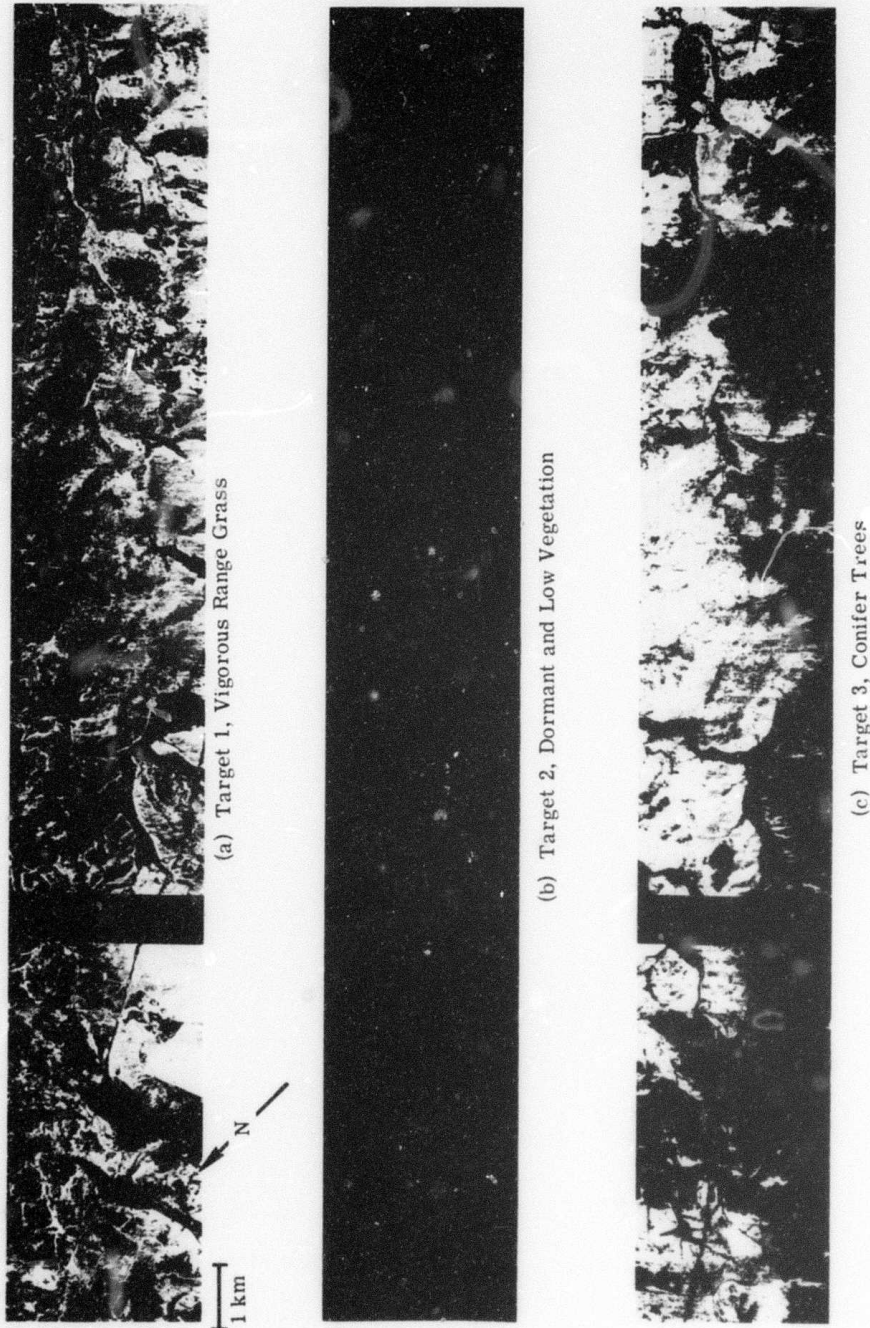


FIGURE 14. RECOGNITION MAPS PRODUCED BY STATISTICAL DECISION THEORY WITH SINGLE-CHANNEL INPUTS FOR VEGETATIVE TARGETS IN FLIGHT SECTION 2B OF BLACK HILLS DATA SET

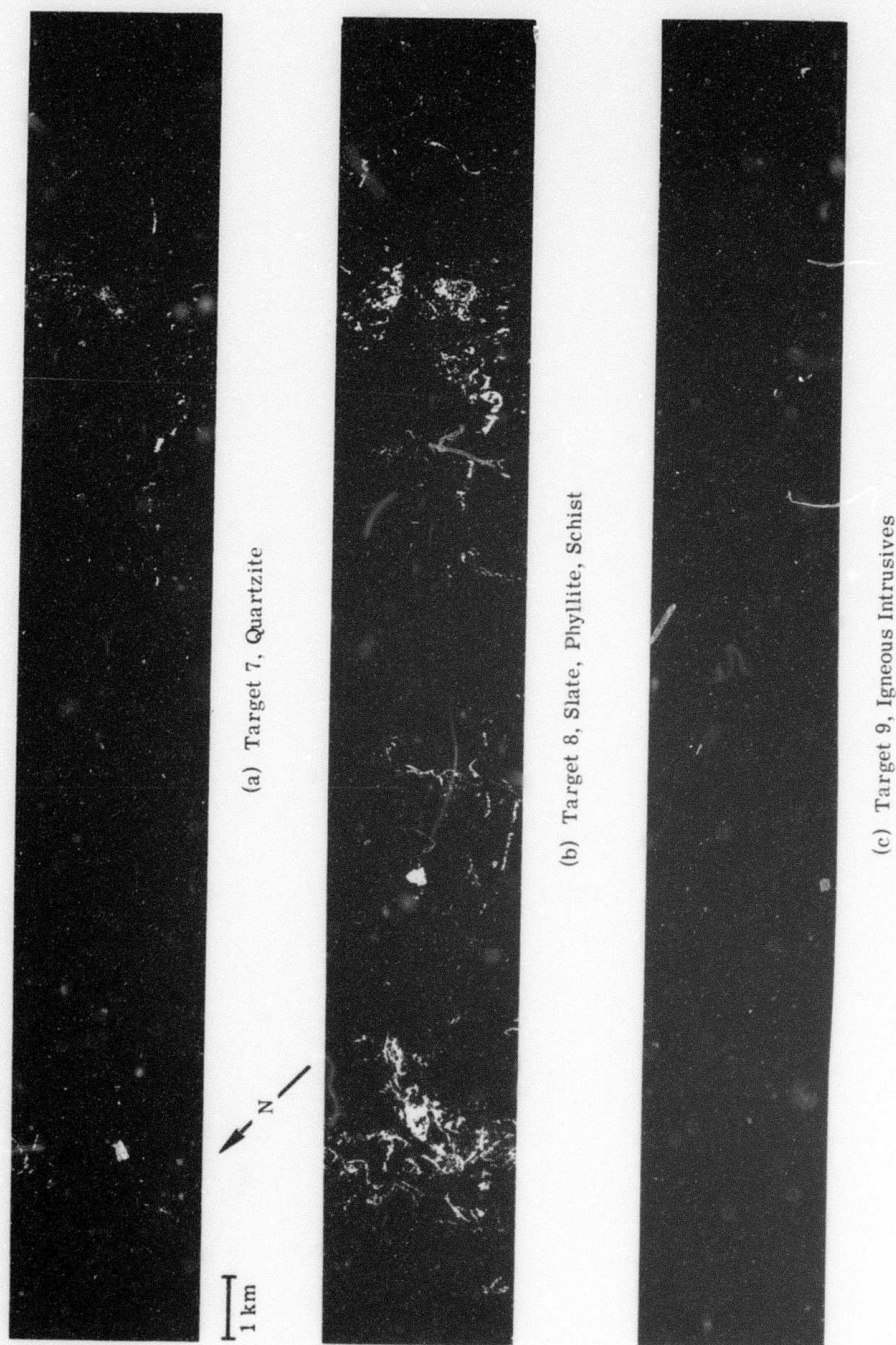


FIGURE 15. RECOGNITION MAPS PRODUCED BY STATISTICAL DECISION THEORY WITH SINGLE-CHANNEL INPUTS FOR GEOLOGIC TARGETS IN FLIGHT SECTION 2B OF BLACK HILLS DATA SET

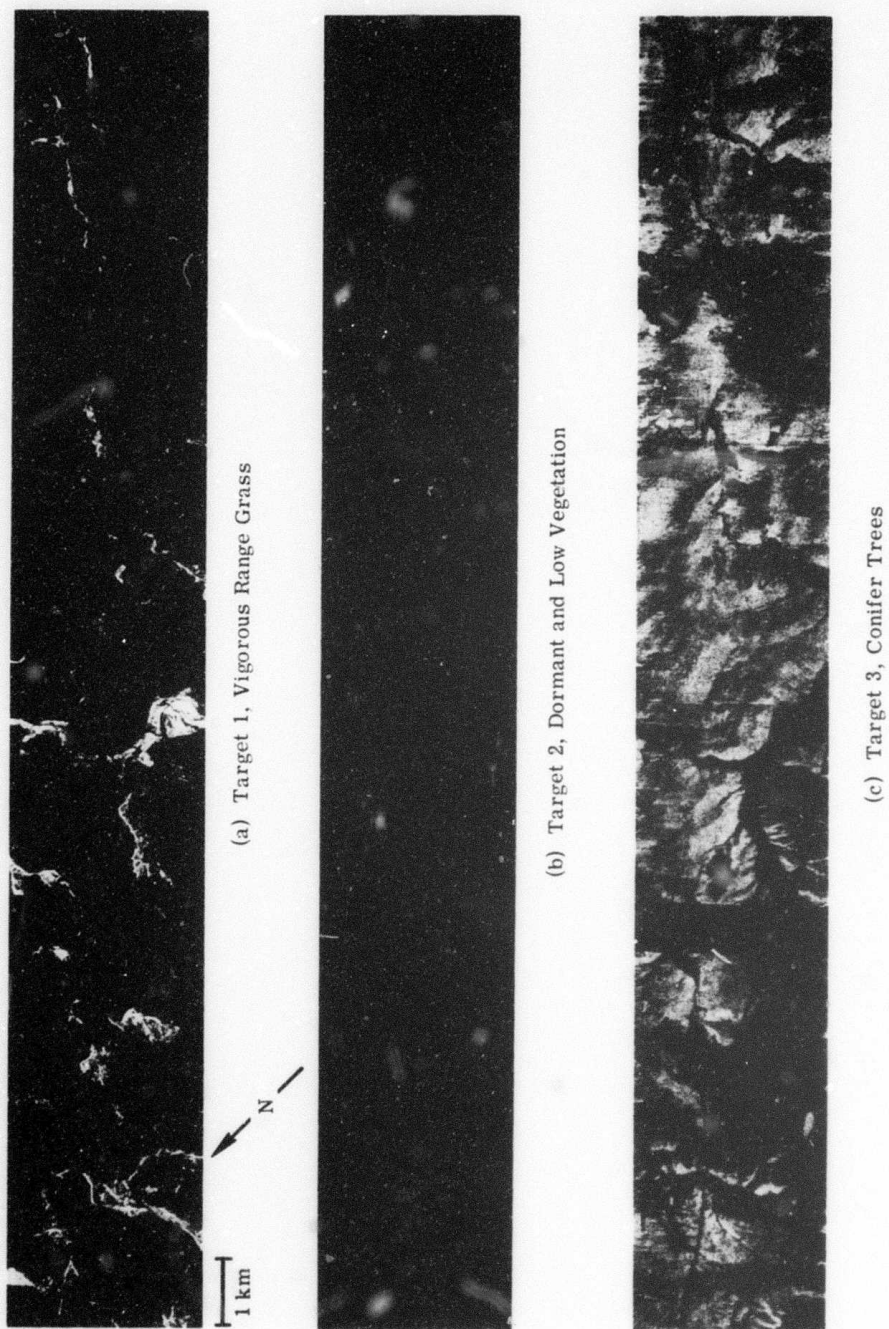


FIGURE 16. RECOGNITION MAPS PRODUCED BY STATISTICAL DECISION THEORY WITH RATIO INPUTS FOR VEGETATIVE TARGETS IN FLIGHT SECTION 2B OF BLACK HILLS DATA SET

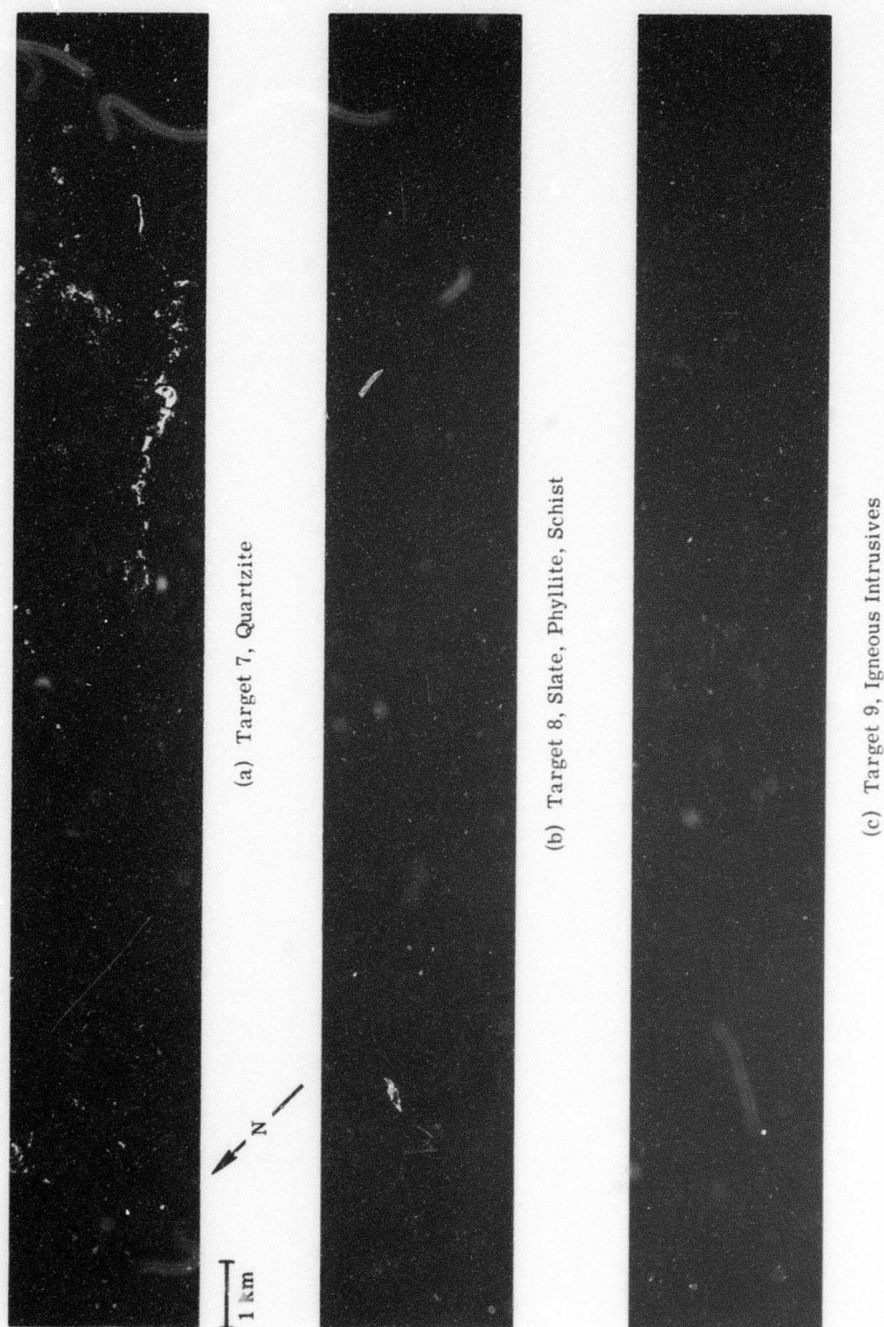


FIGURE 17. RECOGNITION MAPS PRODUCED BY STATISTICAL DECISION THEORY WITH RATIO INPUTS FOR GEOLOGIC TARGETS IN FLIGHT SECTION 2B OF BLACK HILLS DATA SET

TABLE 4. QUALITATIVE COMPARISON OF RECOGNITION RESULTS OF STATISTICAL DECISION THEORY WITH RATIO GATING LOGIC

Target No.	Target Name	Statistical Decision Theory with Single Channel Inputs	Statistical Decision Theory with Ratio Inputs	Ratio Gating Logic
1	Vigorous Range Grass	Recognizes more Conifers than grass.	Recognizes both grass test sites, but misses a lot of vigorous grass.	Good except for the easily correctible problem mentioned in test which misses much grass; has a moderate false alarm rate.
2	Dormant and Low Vegetation	Misses most dormant and low vegetation. (Test site different from that used with RAGAL procedure).	Misses all dormant and low vegetation, except some near rhyolite quarry. (Test site different from that used with RAGAL procedure)	Recognizes most dormant and low vegetation with moderate false alarm.
3	Conifer Trees	Recognizes 2 of 3 test sites, but much shadow and scan-angle effect obvious. Misses many conifers, moderate false alarm rate.	Recognizes 2 of 3 test sites, and misses some other conifers. Not many false alarms, but in general not enough conifers recognized.	Recognizes 3 of 3 test sites, but has moderate false alarm rate, especially with grasses misclassified.
7	Quartzite	Recognizes 3 of 5 test sites, misses about 30% of quartzite and has a moderate false alarm rate.	Recognizes all 5 test sites, but has moderate false alarm rate, mostly with dormant & low vegetation being misclassified. All of quartzite recognized.	Recognizes all 5 test sites, but misses a little quartzite. Very few false alarms.

TABLE 4. QUALITATIVE COMPARISON OF RECOGNITION RESULTS OF STATISTICAL DECISION THEORY
WITH RATIO GATING LOGIC (Concluded)

Target No.	Target Name	Statistical Decision Theory with Single Channel Inputs	Statistical Decision Theory with Ratio Inputs	Ratio Gating Logic
9	Igneous Intrusives (Rhyolite, quartz latite, & Phonolite)	Recognizes rhyolite, but has a high false alarm rate.	Excellent results, with only rhyolite detected; misses a small amount of rhyolite.	Recognizes rhyolite but has moderate false alarms, including some of target 8 & 2 shallow ponds.
8	Slate, Phyllite, Schist	Nothing recognized.	Nothing recognized.	Recognizes test site, but includes some rhyolite, water, and road as false alarms.

best for target 9, but RAGAL was best for targets 2 and 8. Targets 1, 3, and 7 were different for these two types of recognition logic, but neither type could be called superior for those targets. Therefore, the statistical decision theory with ratio preprocessing and RAGAL were approximately equal in this experiment. The former probably could have been further improved by using the same number of test sites for each target as were used with the latter method. However, that would have required more tape loops and SPARC time than could be afforded for this investigation.

This investigation was too economically limited to permit a more exhaustive, quantitative comparison of these recognition methods. A better comparison can be made in the future when the RAGAL procedure is past the prototype stage.

4.4 DISCUSSION AND CONCLUSIONS

A new method for producing automatic recognition maps has been presented and applied to scanner data for the first time. The ratio gating logic (RAGAL) method involves the following: (1) production of selected analog ratio images, (2) the user's determination of a series of ratio ranges for each target from the analog ratio images and their gray-scales, (3) setting these ranges for each ratio on the SPARC computer to form a series of ratio AND gates, and (4) the production of an automatic recognition map for each target via AND-gate logic. This procedure is primarily useful for targets that have distinctive reflective minima (absorption bands) related to chemical composition. Since one of the most useful parameters in geologic mapping is chemical composition, this method is particularly useful for geologic (and possibly soil) mapping.

The procedure was not implemented exactly as desired in this first application, but the two main sources of error can be diminished in future applications of RAGAL by using a photodensitometer instead of visual inspection to compare ratio images with gray-scales and by substituting a simple AND-gate logic black box for the SPARC computer to produce automatic recognition maps with extremum ratio ranges. An alternative to the last step would be the substitution of ratio means and standard deviations for extremum ratio ranges, such that the Euclidian distance decision logic of the SPARC would be more suitable than it is now.

The RAGAL procedure was qualitatively compared with statistical decision theory (for two types of inputs) by producing recognition maps of several geologic and vegetative targets. In general, RAGAL performed about as well as statistical decision theory with ratio preprocessing, and it was much better than statistical decision theory with no preprocessing (single-channel radiance inputs). The data set used for this comparison is from an area in South Dakota with sharp topographic relief, which may in part be why ratio preprocessing (which suppresses illumination variations induced by changes in slope) improved the automatic decisions. In this test the same scanner channels were used for all three types of recognition maps.

Although the RAGAL procedure is not as powerful a decision maker as the statistical decision theory, it has several advantages for the types of targets sought in the Black Hills data set:

- (1) RAGAL results are relatively easy to relate to laboratory spectra because of the ratio suppression of environmental effects (slopes, shadows, atmospheric effects, etc.) and because of the simple logic involved.
- (2) Because of this relatability to laboratory spectra and because the ratio images allow the user to determine the ratio values of a target prior to making an automatic recognition map, the RAGAL procedure is more predictive in the sense that the user has a good idea about what targets can and cannot be discriminated before the automatic recognition maps are produced.
- (3) Feature selection is relatively simple because the user can determine what ratio pairs are best for which target from lab data, instead of from scanner data.
- (4) Ratio preprocessing, an important part of RAGAL, should yield more repeatable results from one data set to another than any decision process based on single-channel radiances. This has yet to be proven, however.
- (5) Ratio images, also an important constituent of RAGAL, are useful research tools for seeking new physical phenomena to monitor by remote means. Patterns which the observer can see in ratio images are sometimes unrecognizable in single-channel images or in automatic recognition maps. Ratio images are attention-focusing tools.
- (6) RAGAL is less expensive than statistical decision theory because SPARC training is replaced by a cheaper training operation.
- (7) Because of the relatability to lab data, RAGAL should be capable of automatic training in the future — with lab data as training sets.
- (8) Finally, since RAGAL uses a much simpler logic than statistical decision theory, it can be made operational more easily. In fact, ratio gating logic could be done by a small, inexpensive on-board processor in future aircraft and satellites.

Efforts are now being made to incorporate the ERSIS data band into the RAGAL procedure and to test the procedure again with one or more different geological data sets.

DISCRIMINATION OF COMPOSITIONAL DIFFERENCES BY THE RATIO METHOD

Aerial Photography has long been an extremely useful tool for geologists. The spectral range of photographic film sensitivity, however, is limited to electromagnetic spectrum wavelengths shorter than approximately $0.9 \mu\text{m}$. Because of this restricted spectral range, photography is limited in two important aspects. First, the sun or some other external source of light is always required since only reflected radiation from a target can be observed. Under average day time conditions, with temperatures on the order of 300°K , the radiation emanating from targets at wavelengths shorter than $3 \mu\text{m}$ is primarily reflective, and at longer wavelengths is primarily emitted by the target itself. Secondly, from a geochemical standpoint, photography is limited to observing compositional differences in targets related to intra-atomic phenomena. Electronic transitions in the outer shells of certain ions (such as Fe^{+3} , Fe^{+2} , Cu^{+2} , and OH^{-1}) produce spectral reflectance minima at wavelengths up to approximately $2.3 \mu\text{m}$. However, there are important spectral features of silicates and other geological targets (carbonates, sulfates, etc.), related primarily to interatomic phenomena, which occur at wavelengths longer than approximately $2.0 \mu\text{m}$. In particular, interatomic vibrations of silicate rocks produce characteristic spectral emittance minima in the $8.0\text{-}\mu\text{m}$ to $14\text{-}\mu\text{m}$ region; these minima contain information concerning both the chemical composition and lattice structure of crystalline rocks.

Over the last decade, a new means of collecting spectral information in imaged form has been developed: the multispectral scanner. Instead of detecting radiation simultaneously from all elements in the scene to be imaged in only three or fewer spectral regions, as a camera does, the multispectral scanner detects radiation from many narrow spectral regions for only one point in the scene at a time. The final image is produced through point-by-point scanning. Finer spectral resolution and much greater spectral range (out to $14 \mu\text{m}$ for terrestrial applications) are obtained with scanners than with cameras. Therefore, the multispectral scanner offers a new and valuable source of diagnostic information about chemical composition that can be useful for geologic mapping.

The first part of this section (which comprises part of Robert Vincent's Ph.D. dissertation [13]) is limited to igneous silicate rocks and to the $8\text{-}\mu\text{m}$ to $14\text{-}\mu\text{m}$ spectral region, a thermal infrared atmospheric "window" which contains some of the most compositionally diagnostic spectral information on silicates. Working with an infrared ratio method devised earlier and a detailed knowledge of how detected radiances from a given rock are related to

13. Robert Vincent, A Thermal Infrared Ratio Imaging Method for Mapping Compositional Variations Among Silicate Rock Types, Unpublished Ph.D. dissertation, The University of Michigan, 1973.

its chemical and mineralogical compositions, the objective of this first part of the investigation is to define a better basis of discrimination for imaging compositional differences among silicate rocks.

The second part deals with experimental ratioed imagery only in the 0.4 to 2.5- μ m wavelength region, collected during a 1972 flight over a region in the Black Hills of South Dakota. The rock types include igneous, metamorphic, and sedimentary. The objectives of this part of the investigation are to determine empirically which rocks in that test area can be discriminated from one another and to develop a simpler method for producing automatic recognition maps of geologic targets.

5.1 DEFINITION OF THE BASIS FOR DISCRIMINATION OF THE INFRARED RATIO AMONG IGNEOUS SILICATES

In last year's final report under this contract [14] and in three other publications [9, 11, 12], a two-channel, infrared-ratio-imaging technique was described which produces ratio images that both enhance spectral emittance variation related to compositional differences and suppress temperature variations across a given scene. The infrared ratio (called $R_{1,2}$) was found to be crudely correlated (correlation coefficient = 0.74) to %SiO₂ of igneous rocks. The purpose of this part of the investigation is to define one or more bases of discrimination of the infrared ratio method which are better correlated than %SiO₂ with $R_{1,2}$.

In last year's report [14] an experiment was described which provided new laboratory data for silicate rocks. The spectral emittance curves resulting from that experiment are shown in Fig. 18. The chemical composition of each of the 26 igneous rocks, determined from rapid rock analysis by the U.S. Geological Survey, is given in Table 5. From these spectra and an atmospheric model [15], the $R_{1,2}$ ratio was calculated for each rock for the case of the two-element infrared detector (described in last year's report [14]) flown at an altitude of 1 km above ground on a clear dry day.

The equations for calculating $R_{1,2}$ are given below. The total spectral radiance received by the detector from the direction of the target can be calculated from Eq. (1) [16]:

14. T. Wagner, R. K. Vincent, B. Drake, R. Mitchell, and P. Jackson, Tunnel-Site Selection by Remote Sensing Techniques, The University of Michigan, Technical Report No. 10018-13-F, U.S. Bureau of Mines Contract HO210041 (ARPA Order No. 1579, Amend. 2, Program Code IF10), 1972.

15. D. Anding, R. Kauth, and R. Turner, Atmospheric Effects on Infrared Multispectral Sensing of Sea Temperature from Space, Willow Run Laboratories, Report No. 2676-5-F, 1970.

16. W. L. Wolfe, ed., Handbook of Military Infrared Technology, U.S. Office of Naval Research, Department of the Navy, Washington, 1965, pp. 9-20.

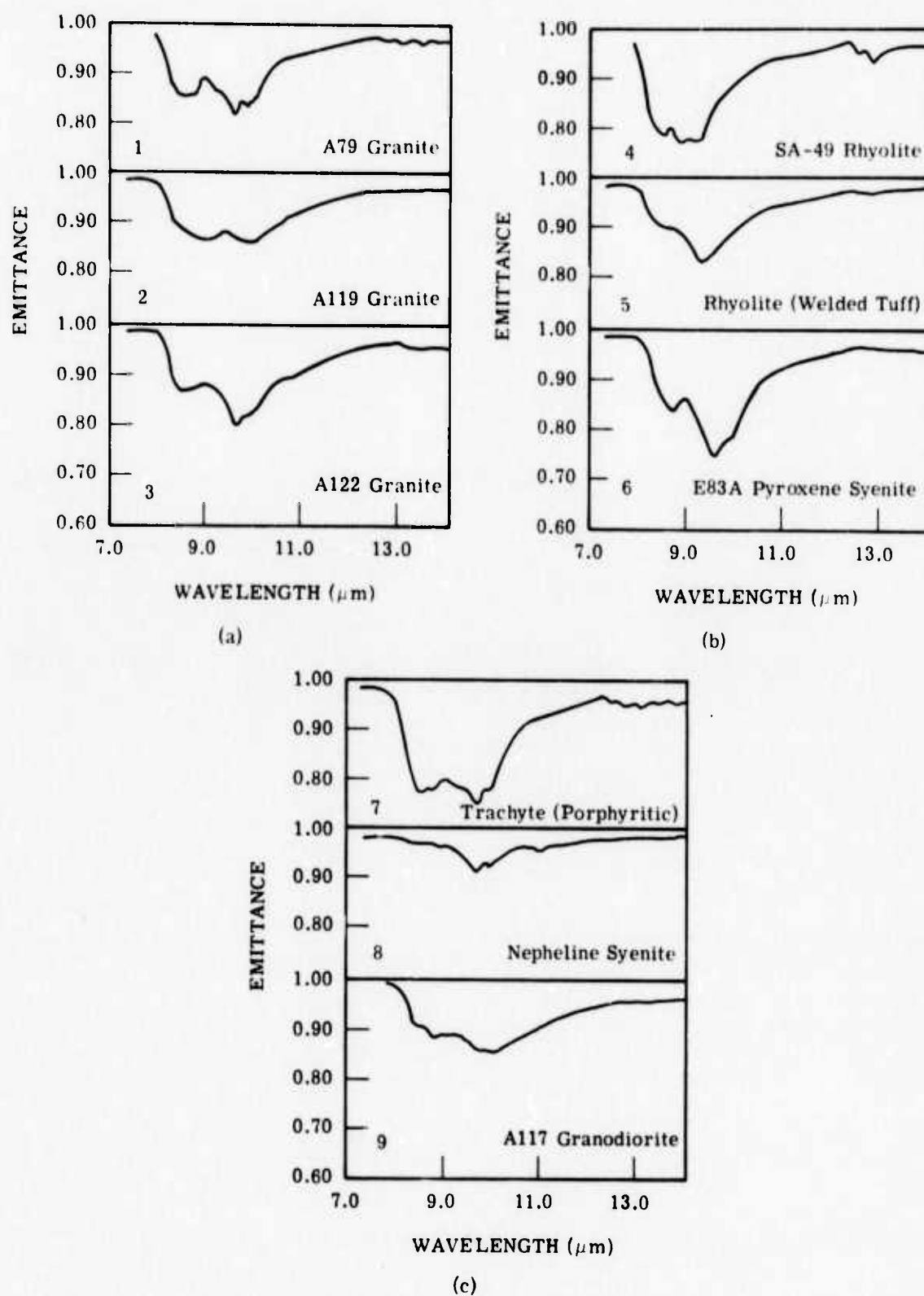
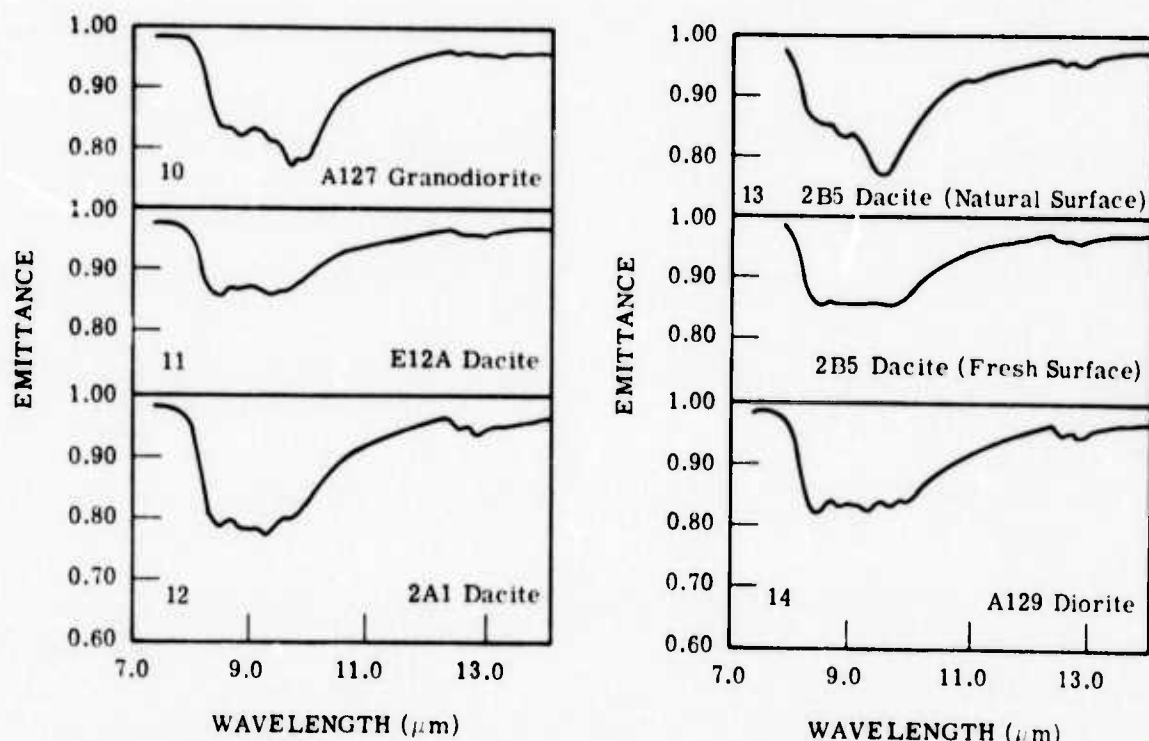
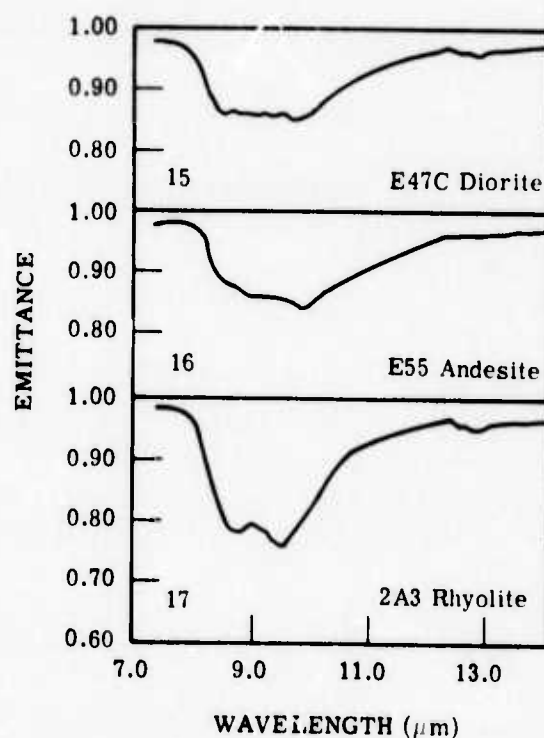


FIGURE 18. INFRARED SPECTRA OF IGNEOUS SILICATE ROCKS



(d)

(e)



(f)

FIGURE 18. INFRARED SPECTRA OF IGNEOUS SILICATE ROCKS (Continued)

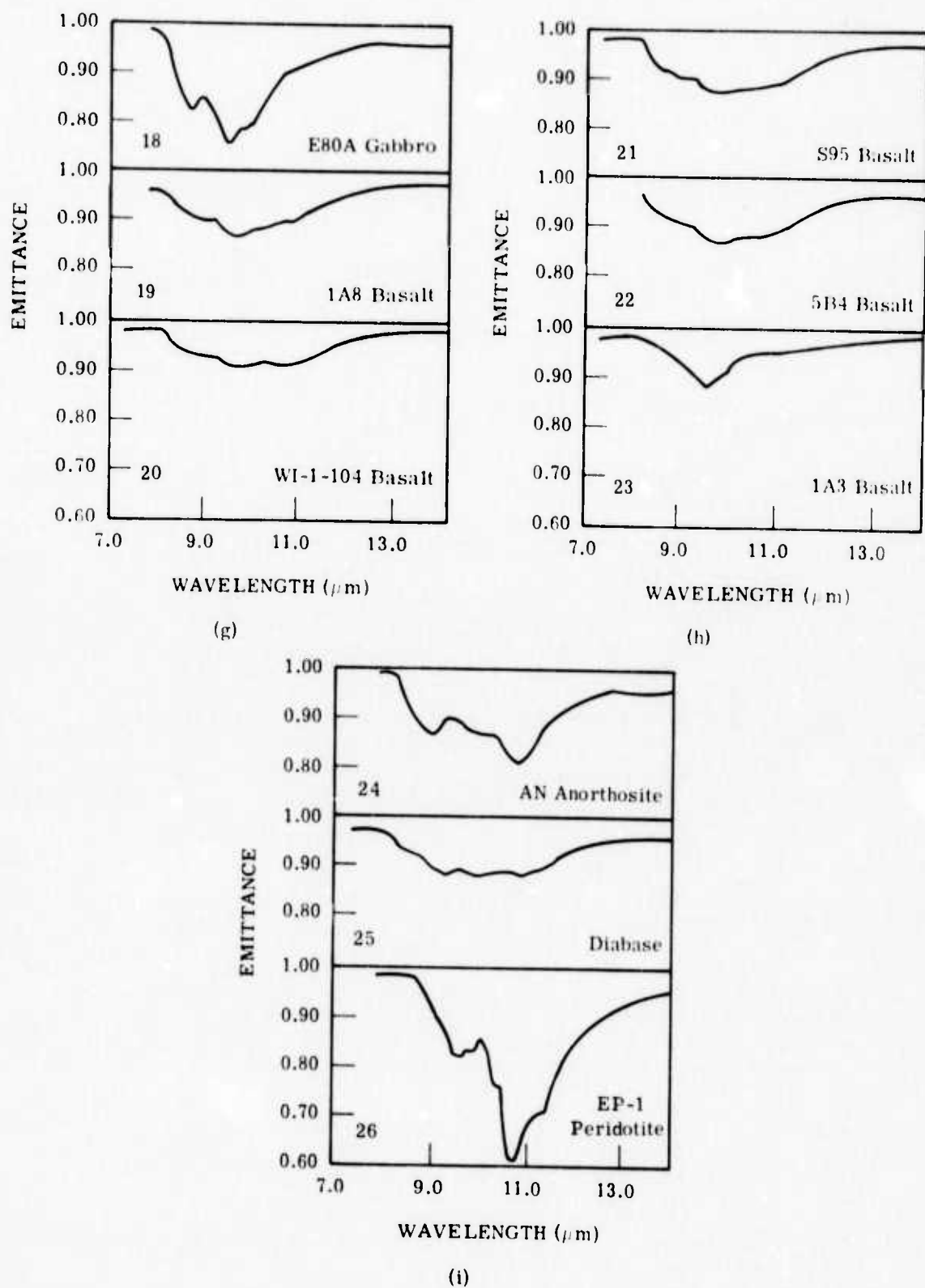


FIGURE 18. INFRARED SPECTRA OF IGNEOUS SILICATE ROCKS (Concluded)

TABLE 5. CHEMICAL COMPOSITION OF IGNEOUS SILICATE ROCK SAMPLES IN WEIGHT PERCENT

Sample No.	Sample Name	SiO ₂	Al ₂ O ₃	Fe ₂ O ₃	FeO	MgO	CaO	Na ₂ O	K ₂ O	H ₂ O	TiO ₂	P ₂ O ₅	MnO	CO ₂
1	Granite	76.7	12.8	0.49	0.05	0.15	0.11	4.50	4.30	0.39	0.06	0.01	0.02	<.05
2	Granite	66.2	16.5	0.82	2.80	1.10	2.60	3.90	4.90	0.72	0.53	0.16	0.08	<.05
3	Granite	72.4	14.2	0.88	1.20	0.31	1.20	3.60	5.00	0.74	0.20	0.04	0.06	<.05
4	Rhyolite	75.1	11.5	1.80	0.80	0.23	0.51	4.00	4.40	1.40	0.25	0.04	0.00	<.05
5	Rhyolite (Welded)													
6	Tuff	76.1	12.1	1.00	0.56	0.15	0.21	3.50	4.60	1.57	0.12	0.00	0.00	<.05
7	Syenite	61.4	20.3	1.60	0.52	0.24	0.99	3.60	9.70	0.86	0.22	0.03	0.04	0.21
8	Trachyte	68.3	17.7	1.00	0.60	0.26	0.31	4.80	5.10	0.82	0.24	0.03	0.13	0.24
9	Nepheline													
10	Syenite	58.3	19.7	1.90	1.30	0.53	1.50	7.40	6.40	0.98	0.82	0.09	0.30	<.05
11	Granodiorite	53.6	18.7	1.30	7.00	3.80	6.20	3.90	2.80	1.20	0.99	0.18	0.17	<.05
12	Granodiorite	62.8	16.0	0.64	1.60	0.90	1.80	3.90	4.40	0.99	0.56	0.09	0.04	<.05
13	Dacite	65.7	15.0	1.20	1.30	1.50	3.00	3.90	3.40	1.24	0.35	0.16	0.04	2.70
14	Dacite	66.9	15.3	1.10	1.60	1.40	3.80	3.80	2.40	2.02	0.59	0.14	0.00	0.21
15	Dacite	67.0	16.0	1.60	1.60	1.80	2.10	4.10	2.80	2.07	0.63	0.16	0.00	<.05
16	Diorite	61.0	16.4	1.80	5.60	1.40	4.60	4.30	2.50	1.00	0.92	0.36	0.16	<.05
17	Diorite	56.2	17.4	1.80	5.40	4.40	7.10	3.90	1.80	0.71	0.84	0.29	0.12	<.05
18	Andesite	57.8	15.2	2.20	3.30	5.00	5.50	3.20	1.80	2.40	0.51	0.20	0.09	2.60
19	Rhyolite	67.9	14.5	1.80	0.40	0.53	1.10	0.59	10.00	1.71	0.44	0.09	0.02	0.38
20	Gabbro	50.6	15.7	4.00	6.50	6.90	10.7	2.40	0.70	0.94	0.86	0.12	0.17	<.05
21	Basalt	47.5	16.3	2.20	7.90	7.90	8.90	3.70	1.60	0.74	2.10	0.62	0.13	<.05
22	Basalt	48.0	15.1	2.90	7.60	9.40	9.50	3.20	1.10	0.74	1.80	0.60	0.12	<.05
23	Basalt	48.4	16.6	2.20	8.00	7.30	9.40	3.50	1.30	0.55	2.00	0.51	0.13	<.05
24	Basalt	48.3	16.5	1.60	8.60	7.60	8.10	3.70	1.70	0.71	2.30	0.73	0.13	<.05
25	Anorthosite	47.8	16.9	2.10	8.10	6.20	10.1	3.10	1.00	0.97	1.90	0.38	0.12	0.76
26	Diabase	49.7	28.3	0.84	1.60	1.50	13.9	2.50	0.13	0.71	0.30	0.02	0.00	<.05
27	Peridotite	52.4	15.0	1.10	8.50	7.10	10.7	2.00	0.64	1.21	1.00	0.13	0.13	<.05
28	Peridotite	44.5	01.5	0.23	7.70	43.3	1.80	0.13	0.08	0.56	0.10	0.04	0.07	<.05

$$L_{\lambda}(T) = [\epsilon_{\lambda} L_{\text{bb}\lambda}(T) + \rho_{\lambda} L_{\text{sky}}] \tau_{A\lambda} + L_{V\lambda} = \{\epsilon_{\lambda} [L_{\text{bb}\lambda}(T) - L_{\text{sky}\lambda}] + L_{\text{sky}\lambda}\} \tau_{A\lambda} + L_{V\lambda} \quad (1)$$

where $L_{\lambda}(T)$ = the total spectral radiance of wavelength λ arriving at the detector

$\epsilon_{\lambda} = 1 - \rho_{\lambda}$ = the rock emittance taken from laboratory data

$L_{\text{bb}\lambda}(T)$ = the spectral radiance of a blackbody at the same temperature, T , as the rock

$L_{\text{sky}\lambda}$ = the spectral radiance from the sky incident on the diffuse rock surface

$\tau_{A\lambda}$ = the spectral atmospheric transmittance

$L_{V\lambda}$ = the spectral radiance from emission and scattering into the beam by the atmosphere in the path between rock and detector

For two bands of approximately 8.2-10.9 μm and 9.4-12.1 μm and an assumed rock temperature of 300°K, Eq. (1) was integrated over the respective spectral regions, and a ratio of radiances in the two bands for each of the laboratory rock samples was calculated from the following equation:

$$R_{1,2} = \frac{L_1(T)}{L_2(T)} = \frac{\int_{\lambda_a}^{\lambda_b} f_1(\lambda) L_{\lambda}(T) d\lambda}{\int_{\lambda_c}^{\lambda_d} f_2(\lambda) L_{\lambda}(T) d\lambda} \quad (2)$$

where λ_a and λ_b = limits of band 1

λ_c and λ_d = limits of band 2

$f_1(\lambda)$ and $f_2(\lambda)$ = the exact detector spectral responses

$L_1(T)$ and $L_2(T)$ = the total detected radiances in the two respective bands

This calculated $R_{1,2}$ (given in Table 6 for each rock) should agree with scanner-measured $R_{1,2}$ under the altitude and atmospheric conditions prescribed above.

The question to be answered is, What chemical and/or mineralogical parameters of these igneous rocks are best correlated with $R_{1,2}$? Before the answers are given, however, the statistical procedures used to obtain them will be explained.

5.1.1 STATISTICAL PROCEDURES

The statistical method chosen to determine the best regression equations for this investigation is a stepwise regression [17], which is available in The University of Michigan's MIDAS

17. N. Draper and H. Smith, Applied Regression Analysis, John Wiley and Sons, Inc., New York, 1967, pp. 171-172.

TABLE 6. THERMAL INFRARED RATIOS ($R_{1,2}$) CALCULATED FROM
LABORATORY SPECTRA

<u>Sample Number</u>	<u>Sample Name</u>	<u>Calculated $R_{1,2}$</u>
1	Granite (A79)	1.1761
2	Granite (A119)	1.1946
3	Granite (A122)	1.1987
4	Rhyolite (SA-49)	1.1266
5	Rhyolite	1.1741
6	Pyroxene Syenite (A83E)	1.1784
7	Trachyte	1.1442
8	Nepheline Syenite	1.2094
9	Granodiorite (A117)	1.2134
10	Granodiorite (A127)	1.1723
11	Dacite (E12A)	1.1724
12	Dacite (2A1)	1.1436
13	Dacite (2B5) W	1.1574
	Dacite (2B5) F	1.1686
14	Diorite (A129)	1.1685
15	Diorite (E47C)	1.1795
16	Andesite (E55A)	1.1962
17	Andesite (2A3)	1.1394
18	Gabbro (E80A)	1.1810
19	Basalt (1A8)	1.2154
20	Basalt (WI-1-104)	1.2204
21	Basalt (S95)	1.2246
22	Basalt (5B4)	1.2255
23	Basalt (1A3)	1.2018
24	Anorthorite	1.2458
25	Diabase	1.2204
26	Peridotite	1.3723

Statistical Laboratory software system. The stepwise regression method seeks to find the best linear combination of independent variables, (X_i), for prediction of the dependent variable, (Y), through the following steps:

- (1) Prescribed significance levels are chosen for the acceptance and rejection of X_i variables from the regression equation—for instance, a significance level (the higher the significance level the more insignificant the variable) of 0.6 for acceptance would mean that to be selected for regression, an X_i variable has to account for at least 40% of all the residual error in \hat{Y} , the predicted value of Y .
- (2) The X_i variable (for example, X_1) which is most highly correlated with Y is found and a least squares equation of the predicted value of Y is calculated, such that $\hat{Y} = f(X_1)$.
- (3) The remaining X_i variables are searched, and the one with the highest partial correlation coefficient with Y (which will be called X_2) is used to calculate a second least squares equation, $\hat{Y} = f(X_1, X_2)$ —this procedure is continued for the other X_i .
- (4) After each new X_i variable is selected, a partial F-test on the X_i variables selected in previous steps is conducted, and if the significance level of one of the earlier selected variables becomes higher than the prescribed significance level for rejection, the variable is dropped, and a least squares equation is calculated without it—for instance, if the addition of X_3 increases the significance of X_1 above a certain prescribed level, the new least squares equation would be of the form $\hat{Y} = f(X_2, X_3)$.
- (5) The procedure terminates when there are no other X_i variables with a significance level less than the prescribed significance level of acceptance.

This stepwise regression procedure was performed primarily for equal significance levels of acceptance and rejection. The procedure was performed once for each of the following significance levels of acceptance and rejection: 0.5, 0.6, 0.7, 0.8, and 0.99. The 0.99 level accepts all of the variables and rejects none for almost any data set.

Applying the stepwise regression procedure for the five prescribed significance levels resulted in from one to five regression equations, each with a different number of variables. Three criteria were used to judge which of these regression equations was best for a given set of variables. First, the significance level of the regression equation (this is different from the partial significance levels for X_i variables mentioned in the above procedure) was required to be ± 0.01 , which means that there is a 99% or greater probability that the resulting regression equation was not caused by a set of random data points. Second, the multiple correlation coefficient, (r), and standard error, (s.e.)—at the mean (\bar{Y}) value of Y —for the final regression equation had to be improved over other regression equations with fewer

variables to justify the use of one more variable. For n rock samples, r and s.e. are given by

$$r = \frac{\sum_{j=1}^n (\hat{Y}_j - \bar{Y})^2}{\sum_{j=1}^n (Y_j - \bar{Y})^2} \quad (3)$$

$$\text{s.e.} = \left[\frac{1}{(n - p - 1)} \sum_{j=1}^n (Y_j - \hat{Y}_j)^2 \right]^{1/2} \quad (4)$$

Thirdly, the regression equations had to be physically reasonable. The latter two criteria were substantially subjective.

Three of the regressions performed later in this investigation involve only one independent and one dependent variable. For those cases, a simple correlation coefficient, (r_{XY}), will be cited:

$$r_{XY} = \frac{\sum_{j=1}^n (X_{ij} - \bar{X})(Y_j - \bar{Y})}{\left[\sum_{j=1}^n (X_{ij} - \bar{X})^2 \right]^{1/2} \left[\sum_{j=1}^n (Y_j - \bar{Y})^2 \right]^{1/2}} \quad (5)$$

The values of r_{XY} can range from +1.0 to -1.0, whereas the values of r in Eq. (3) range only from +1.0 to 0.

5.1.2 CORRELATION OF CALCULATED RATIOS WITH CHEMICAL PARAMETERS

The two infrared channels for which $R_{1,2}$ have been calculated are available on an existing infrared scanner (the NASA M-7 scanner aboard the Environmental Research Institute of Michigan's C-47 aircraft). The question to be addressed in this section is, With what chemical parameters can a ratio of these two channels be significantly correlated? Because these channels are broad and overlapping, the answers will be pertinent to ratios for other, possibly narrower, channels in the general vicinity of 8.2-10.9 μm and 9.4-12.1 μm . A better combination of measured parameters, given other infrared channels of data, is determined in the thesis mentioned earlier [13]. There, a linear combination of several infrared ratios is used to identify rock type on the basis of a commonly used igneous rock classification chart.

In the discussion to follow, three subsets of the data in Table 5 will be referred to. Set A includes samples 1-25, excluding only 26. Set B includes all but four samples (1, 3, 5, and 26). These two subsets are used only with chemical parameters. Sample 26, peridotite, was excluded from consideration with the chemical parameters because it is outside the range of % SiO₂ for which a linear correlation between % SiO₂ and R_{1,2} is expected from previous laboratory data and because its R_{1,2} ratio is sufficiently distinct from the other rock samples to be unique. Set C, used only for the mineralogical parameters, includes all samples except for 22 (for a reason given later).

Table 7 lists the results of a stepwise regression performed on Set A with oxides listed in the order of descending selection. Similar results are also shown for Set B. The best regression equation relating predicted R_{1,2} values (which will be called C₁₂) to 12 oxides from Table 5 can be expressed as

$$C_{12} = A_0 + \sum_{i=1}^{12} A_i O_i \quad (6)$$

where A₀ = constant coefficient (Table 7)

A_i = coefficient for i-th oxide (Table 7)

O_i = weight % of i-th oxide (e.g., % SiO₂, % Fe₂O₃, etc.)

For Set A, the correlation coefficient, (r), between the chemical parameter C₁₂ from Eq. (6) and experimental R_{1,2} values from Table 2 is 0.9131, with an approximate 0.018 standard error in R_{1,2}. Part of the reasoning which led to the use of all 12 oxides was based on the fact that a geologist who has a rapid rock analysis performed on his samples can have all 12 of these oxides measured as cheaply as it would cost him to have only nine or ten measured.

The best single chemical parameter is % SiO₂, which is plotted versus R_{1,2} in Fig. 19 for all 26 rock samples. The simple correlation coefficient between % SiO₂ and R_{1,2} for Set A is -0.74, with a standard error in % SiO₂ of 6.39, where R_{1,2} is taken to be the independent variable. From Fig. 19 it is obvious that samples 1, 3, and 5 are responsible for much of the error. Hence, a regression between % SiO₂ and R_{1,2} was performed for Set B (excluding samples 1, 3, and 5 as well as 26), with the resulting simple correlation coefficient of -0.87 and standard error in % SiO₂ of 4.06, where R_{1,2} is once again the independent variable. Samples 1 and 3 are coarse crystalline granites. Part of the reason they are atypical may be their large grain size in relation to the spot-size used for the infrared laboratory measurements (as discussed in the previous section). Sample 5 is a rhyolitic welded tuff. It cannot be conclusively determined from this data set whether these samples are atypical for natural

TABLE 7. REGRESSION OF THE C_{12} (SET A) and C_{12} (SET B)
 CHEMICAL PARAMETERS WITH $R_{1,2}$

Oxide		C_{12} (Set A) Coefficients	C_{12} (Set B) Coefficients
Name	No.		
SiO_2	1	-.000153	-.002149
Fe_2O_3	2	-.020216	-.017907
H_2O	3	-.000126	.004483
Na_2O	4	.009202	.009342
CaO	5	.007289	.006034
K_2O	6	.005383	.005443
MgO	7	.008184	.004965
TiO_2	8	-.010045	-.019345
FeO	9	-.002312	-.001141
MnO	10	.050832	.030810
P_2O_5	11	.015214	.036184
Al_2O_3	12	.000740	.000311
Constant	0	1.111000	1.242200
Correlation (r)		.91	.95
Standard Error (s.e.)		.018	.016

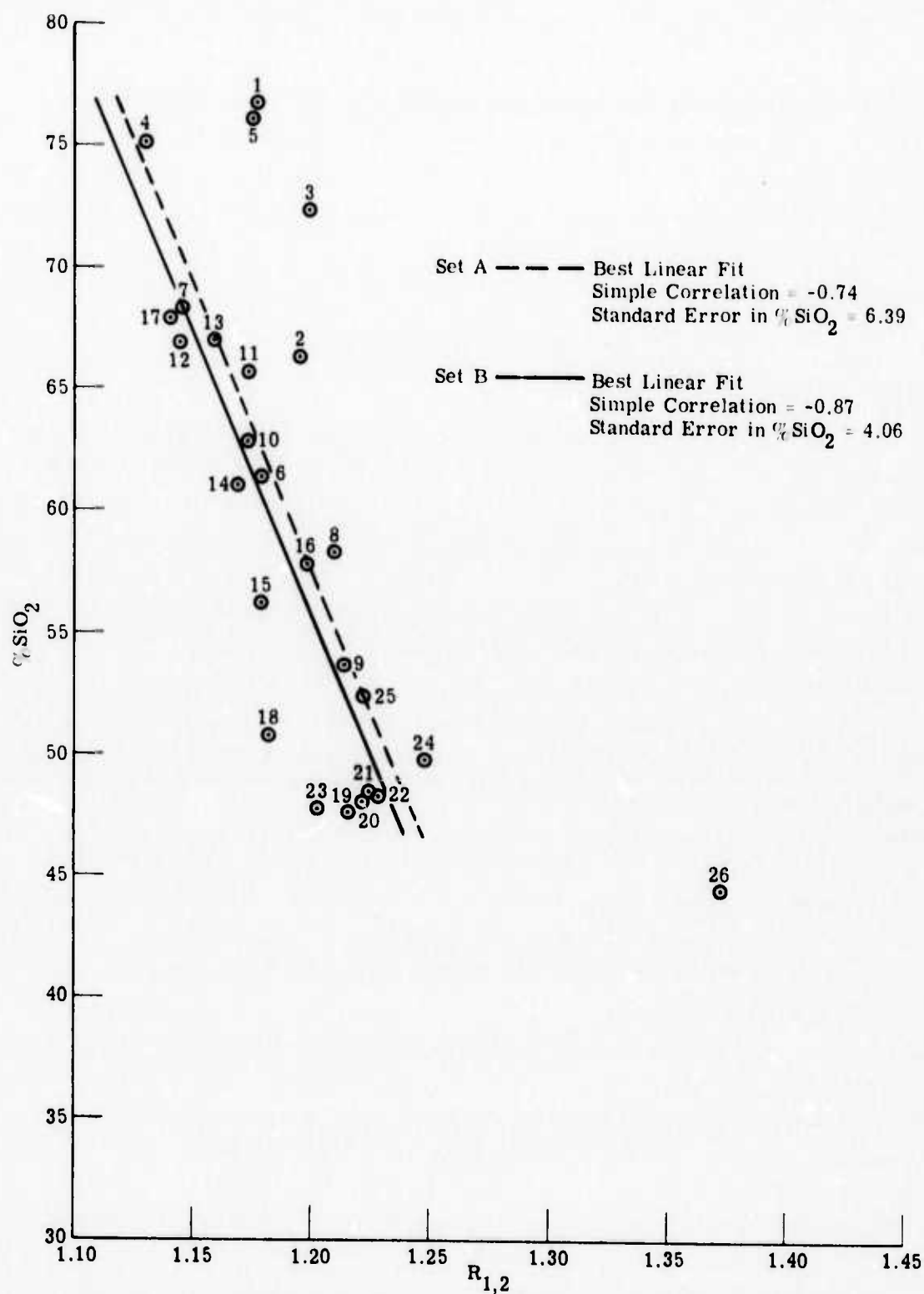


FIGURE 19. CORRELATION OF %SiO₂ WITH R_{1,2} FOR SET A AND SET B

reasons or for reasons related to laboratory measurements. Nevertheless, the relatively high correlation between % SiO₂ and R_{1,2} for the remaining 22 silicate rocks (excluding peridotite) is significant.

The second chemical parameter chosen by the stepwise regression was % Fe₂O₃, such that for Set A the equation for the predicted value of R_{1,2} on the basis of % SiO₂ and % Fe₂O₃ is given by

$$R_{1,2} = 1.3984 - 0.003069(\% \text{ SiO}_2) - 0.016486(\% \text{ Fe}_2\text{O}_3) = 1.3984 - 0.003069\{\% [\text{SiO}_2 + 5.4(\text{Fe}_2\text{O}_3)]\}$$

This indicates that the best two-oxide parameter combination is approximately % [SiO₂ + 5.4(Fe₂O₃)]. This parameter is plotted versus R_{1,2} in Fig. 20. The simple correlation of % [SiO₂ + 5.4(Fe₂O₃)] versus R_{1,2} is -0.82, with a standard error in the two-oxide parameter of 4.63, where R_{1,2} is the independent variable. Similar results were obtained for Set B, except that the coefficient of % Fe₂O₃ which produced the highest correlation was 3.7. The new parameter is plotted in Fig. 21 for members of Set B only. The simple correlation for Set B is -0.92, with a standard error in % [SiO₂ + 3.7(Fe₂O₃)] of 2.94, where R_{1,2} is again the independent variable.

In Table 7, % Al₂O₃ is the last chemical parameter to be selected by the forward regression procedure. However, if % Fe₂O₃ is omitted from the list and a regression is performed on the remaining 11 chemical parameters, % Al₂O₃ is the second parameter selected. The coefficients of % SiO₂ and % Al₂O₃ are almost equal but of opposite sign for this case. Hence, the parameter % (SiO₂ - Al₂O₃), which is plotted versus R_{1,2} for both Set A and Set B in Fig. 22, is a better parameter than % SiO₂ and only slightly worse than % [SiO₂ + 3.7(Fe₂O₃)] for Set B. The simple correlation for Set A is -0.76, with a standard error of 7.43 in % (SiO₂ - Al₂O₃); for Set B it is -0.90, with a standard error of 4.24 in % (SiO₂ - Al₂O₃).

The fact that % Fe₂O₃ should be such an important oxide for relating the chemical and infrared emittance properties of silicate rocks is difficult to understand, since Fe₂O₃ itself exhibits few, if any, spectral features in the 8- to 12-μm wavelength region. Ferric oxide (Fe₂O₃) is a late differentiate of magma, as well as a product of the weathering of mafic minerals. However, since the coefficients of % Fe₂O₃ and % SiO₂ have the same sign, the effect of more Fe₂O₃ is the same as the effect of higher % SiO₂ (i.e., an increase in R_{1,2} — in the direction of more acidic rocks). This may indicate that the late differentiation of Fe₂O₃ is more important with regard to infrared spectral features than the fact that ferric oxide is also a weathering product of mafic minerals. The H₂O, also associated with late differentiation, is also negatively correlated with R_{1,2}. There is a possible correlation between % Fe₂O₃

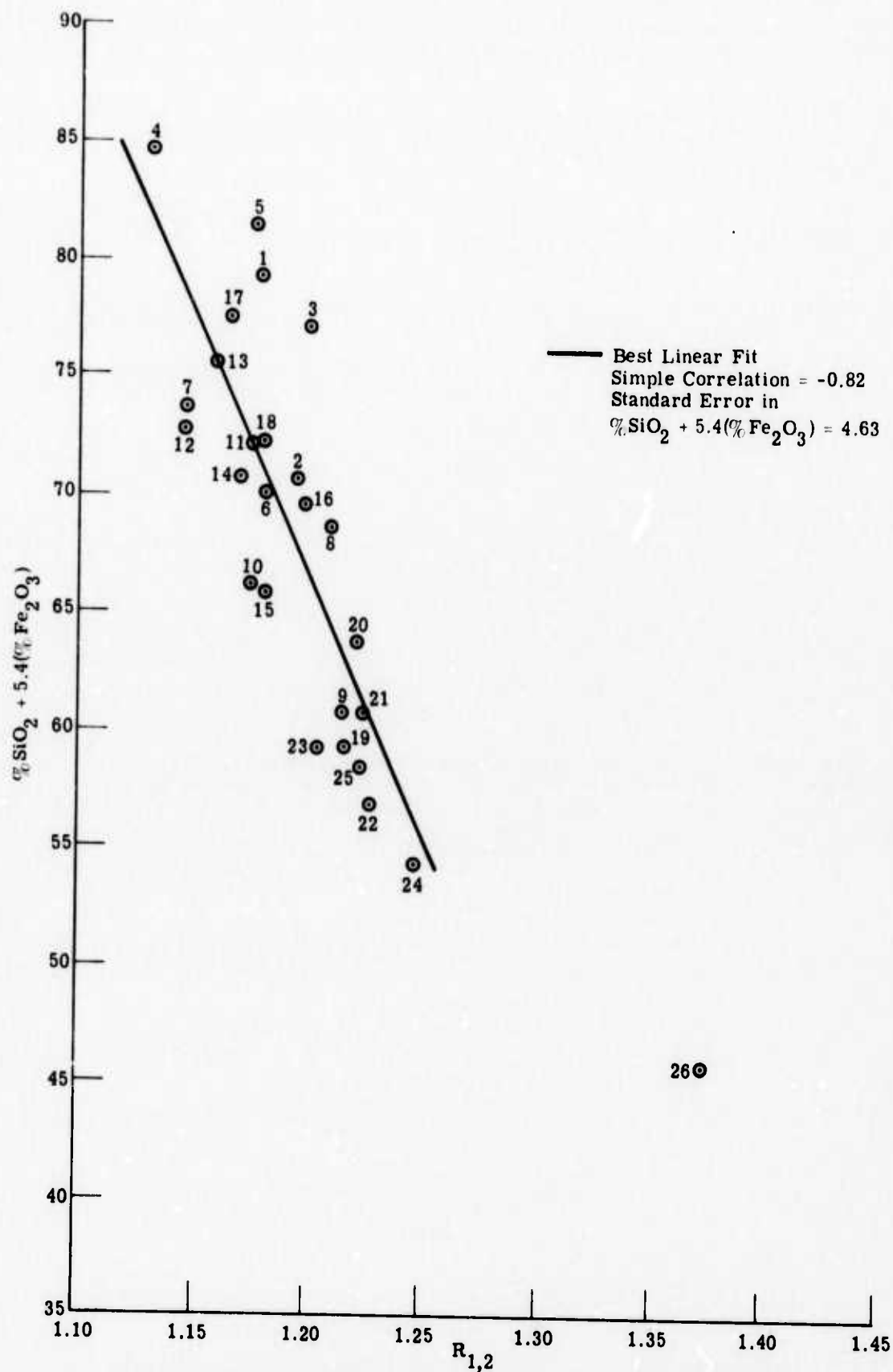


FIGURE 20. CORRELATION OF $\% \text{SiO}_2 + 5.4(\% \text{Fe}_2\text{O}_3)$ WITH $R_{1,2}$ FOR SET A

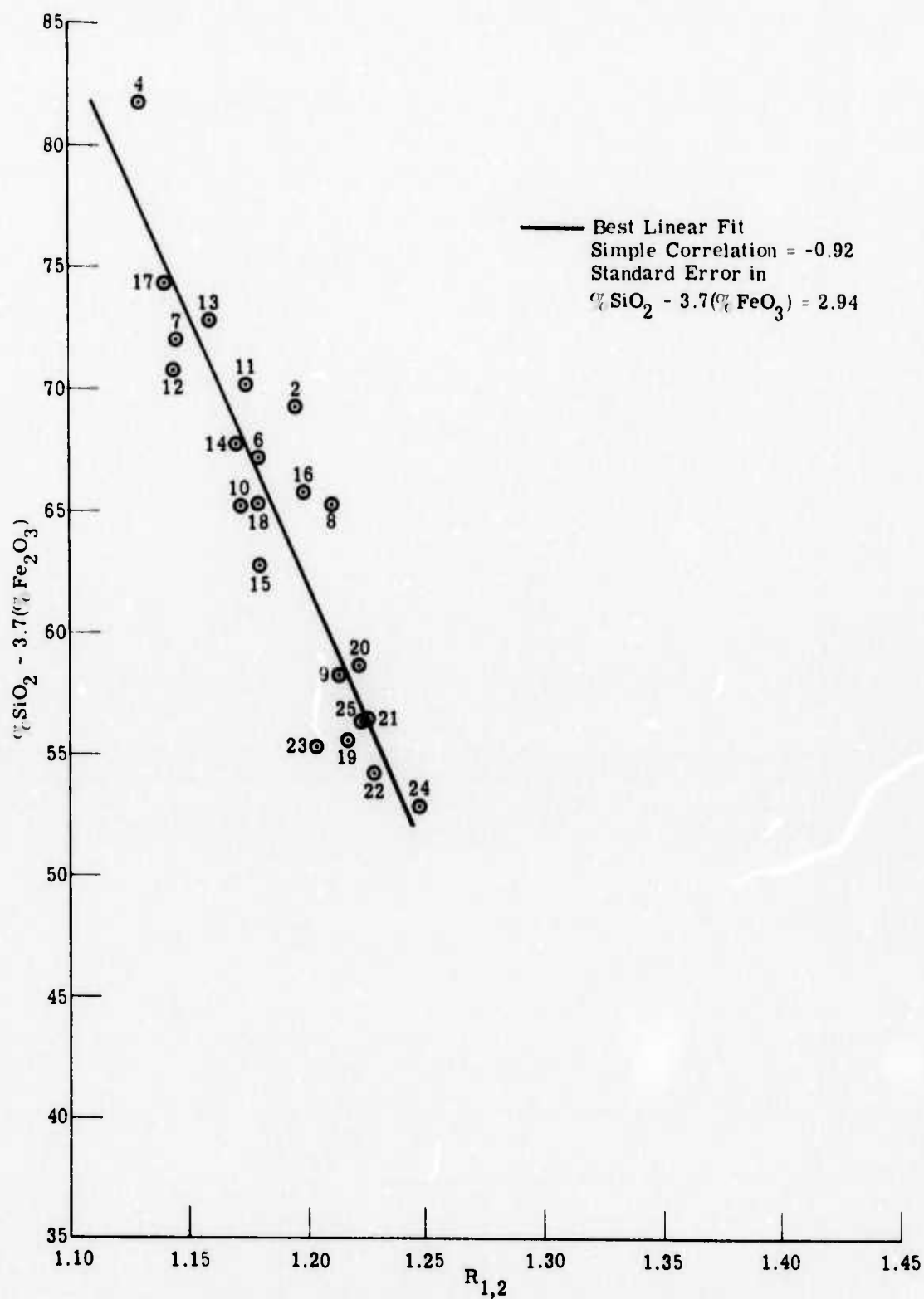


FIGURE 21. CORRELATION OF $\% \text{SiO}_2 - 3.7(\% \text{Fe}_2\text{O}_3)$ WITH $R_{1,2}$ FOR SET B

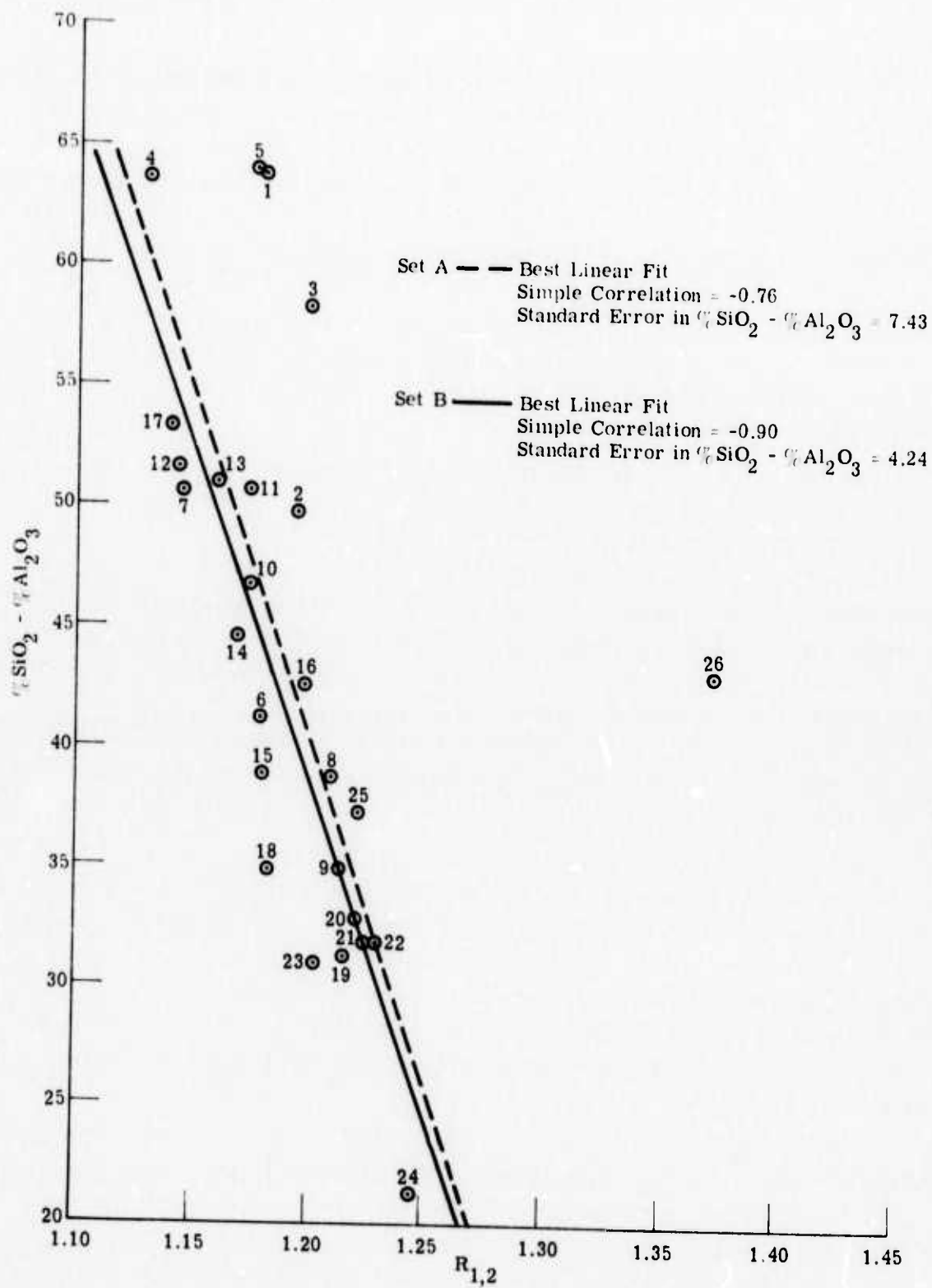


FIGURE 22. CORRELATION OF %SiO₂ - %Al₂O₃ WITH $R_{1,2}$ FOR SET A AND SET B

and the texture of acidic rocks, as evidenced by the fact that the average % Fe_2O_3 is approximately twice as high for the acidic fine- and medium-grained rocks (samples 4, 5, 7, and 17) as it is for the coarse-grained acidic rocks (samples 1, 2, 3, and 10) — according to the new rock classifications in Table 9 of the next section. The intermediate and basic rock samples show about the same % Fe_2O_3 for coarse- and fine-grained rocks. Hence, the importance of % Fe_2O_3 in C_{12} could possibly be an indication of some textural effect on the $R_{1,2}$ ratio for acidic rocks. The correlation of greater % Fe_2O_3 with smaller grain size in acidic rocks could be related either to the near-surface origin of the magma (where sedimentary Fe_2O_3 could enrich the magma) or to disseminated thin coatings formed preferentially on small crystals. The fact that the intermediate and basic rock samples showed no such correlation is evidence contrary to the latter hypothesis.

The relatively high correlation of % $(\text{SiO}_2 - \text{Al}_2\text{O}_3)$ with $R_{1,2}$ is not so surprising, since the infrared emittance minima (reststrahlen bands) of feldspars occur at longer wavelengths than quartz. The substitution of Al^{+3} for Si^{+4} in SiO_4 tetrahedra, which reduces the number of Si-O bonds and increases the Al-O bonds, is common. From our earlier discussion concerning the lower wavelength position of the Si-O reststrahlen bands relative to those caused by Al-O bonds, it is understandable that increased Al_2O_3 would cause the emittance minima to occur at longer wavelengths, thereby increasing $R_{1,2}$. Although the selection of % Fe_2O_3 in the forward regression renders the % Al_2O_3 insignificant, ferric oxide is chosen second to % $(\text{SiO}_2 - \text{Al}_2\text{O}_3)$ in forward regression if % $(\text{SiO}_2 - \text{Al}_2\text{O}_3)$ is treated as one parameter. Hence, the utilization of % Fe_2O_3 suppresses the importance of % Al_2O_3 , but the converse is not true.

Of these chemical parameters, C_{12} is the best for interpreting $R_{1,2}$ scanner ratio images, if the geologist has a collection of rocks for which the rapid rock analyses are known and if he has no normative calculation program to convert the oxides into mineralogical variables, or no modal analyses of the rocks. The C_{12} parameter can be calculated for his collection from Eq. (7) and Table 7, and the resulting C_{12} values can be compared with $R_{1,2}$ from scanner data. If either a normative calculation computer program or modal analysis results are available, however, the mineralogical parameters described in the next section are superior to C_{12} for that purpose.

The chemical parameters % $(\text{SiO}_2 - \text{Al}_2\text{O}_3)$, % $[\text{SiO}_2 + 5.4(\text{Fe}_2\text{O}_3)]$, and C_{12} for igneous rocks may be more relevant than mineralogical parameters for classifying soils by the $R_{1,2}$ ratio imaging method, because igneous rocks and soils are mineralogically different but contain similar oxides. The % $(\text{SiO}_2 - \text{Al}_2\text{O}_3)$ parameter would seem to have the best chance of these three for being applicable to both soils and igneous rocks, because the replacement of Al^{+3} for Si^{+4} is a common effect of weathering.

5.1.3 CORRELATION OF CALCULATED RATIOS WITH MINERALOGICAL PARAMETERS

Instead of stopping with the C_{12} chemical parameter, for two reasons it is also desirable to relate $R_{1,2}$ ratios with the volume percentage of minerals present in the rock samples. First, since the infrared spectral features in the 8- to 14- μ m wavelength region arise from intramolecular energy level transitions, mineral parameters should describe the molecules present better than chemical parameters can. For instance, % SiO_2 does not represent just the free quartz in a rock; it includes silicon and oxygen from other minerals that need not even have tectosilicate structures. Second, quantitatively accurate oxide percentages must be obtained through rapid rock analysis, which is moderately expensive and slow for geologists who do not have their own laboratory facilities for wet chemical analysis. It is desirable, therefore, from the standpoints of cost and convenience alone to relate the $R_{1,2}$ ratios to relative amounts of various common rock-forming minerals, most of which are identifiable by visual inspection and microscopy. Volume instead of weight percentages are desirable because the former are more relatable to area percentages in a thin section and a rock surface imaged by a multispectral scanner.

The mineralogical volume percentages for this experiment were calculated from a C.I.P.W. norm computer program of Rodgers, Cochrane, and LeCouteur [18], on the basis of the oxide percentages obtained from rapid rock analysis (see Table 5). The C.I.P.W. rock classification method was created by Cross, Iddings, Pirsson, and Washington [19]. It classified rocks according to the proportions of certain normative minerals, which are listed in Table 8. These are not all the same as the modal minerals that actually occur in rocks, though some are the same for both cases. The norm is the calculated mineral composition of a given rock, as opposed to the actual mineralogical composition or mode. Arbitrary divisions [20] are made from the proportions of the normative minerals. The inputs to the C.I.P.W. classification scheme are chemical oxides of a given rock such as those shown in Table 5, and the output is the calculated mineral composition of the rock, in terms of the normative minerals.

Table 9 gives the mineralogical parameters resulting from the Rodgers, Cochrane, and LeCouteur computer program (modified to yield volume percentages) for Set C. Sample 22,

18. K. A. Rodgers, R. H. A. Cochrane, and P. C. LeCouteur, Fortran II and Fortran IV Programs for Petrochemical Calculations, Mineralogical Magazine, 37, 1970, pp. 952-953.

19. W. Cross, J. P. Iddings, L. V. Pirsson, and H. S. Washington, A Quantitative Chemico-Mineralogical Classification and Nomenclature of Igneous Rocks, J. of Geology, 10, 1902, pp. 555-690.

20. A. Johannsen, A Descriptive Petrography of the Igneous Rocks, Vol. I, The University of Chicago Press, Chicago, 1931, pp. 85-88.

TABLE 8. NORMATIVE MINERALS

<u>Name</u>	<u>Abbreviation</u>
Quartz	QTZ
Orthoclase	ORTHO
Albite	ALB
Anorthite	ANOR
Nepheline	NEPH
Clinopyroxene (Calcium-rich)	CP(WO)
Clinopyroxene (Magnesium-rich)	CP(EN)
Clinopyroxene (Iron-rich)	CP(FS)
Orthopyroxene (Magnesium-rich)	OP(EN)
Orthopyroxene (Iron-rich)	OP(FS)
Wollastonite	WOL
Olivine (Forsterite)	OL(FO)
Olivine (Fayalite)	OL(FA)
Hematite	HEM
Magnetite	MAG
Ilmenite	ILM
Corundum	COR
Apatite	APA
Calcite	CAL
Water	WAT

TABLE 9. COMPUTED "NORMS" OF SET C ROCK SAMPLES
(VOLUME %, INCORPORATING WATER)

No.	Name	QTZ	ORTHO	ALB	ANOR	CP(WO)	CP(EN)	CP(FS)	OP(EN)	OP(FS)	OL(FO)
1	Granite(A79)	33.34	25.87	38.03	0.16				0.31		
2	Granite(A119)	16.67	30.20	33.77	11.21				2.30	2.49	
3	Granite(A122)	28.64	30.27	30.61	5.43				0.64	0.83	
4	Rhyolite(SA-49)	33.50	26.32	33.60	0.40	0.55	0.44		0.02		
5	Rhyolite(Weld.Tuff)	36.68	27.34	29.22	0.68				0.30		
6	Pyroxene Syenite (E83A)	0.49	58.37	30.43	3.21				0.49		
7	Trachyte	20.44	31.01	40.99					0.54	0.08	
8	Neph. Syenite		38.70	36.99	1.56	1.31	1.06	0.02			
9	Granodior.(A117)		17.97	35.14	25.53	1.50	0.67	0.67	4.40	3.88	2.22
10	Granodior.(A127)	17.75	26.81	33.38	7.70				1.86	1.03	
11	Dacite (E12A)	29.11	20.96	33.77					3.14	0.60	
12	Dacite(2A1)	25.59	14.47	32.18	15.78				2.87	0.69	
13	Dacite(2B5)	25.50	17.01	34.98	8.67				3.72	0.38	
14	Diorite(A129)	13.01	15.80	38.18	17.99	0.92	0.29	0.56	2.71	4.70	
15	Diorite(E47C)	4.57	11.68	35.52	25.20	3.50	1.73	1.04	7.92	4.19	
16	Andesite(E55A)	13.51	11.18	27.91	21.33	0.94	0.62	0.16	9.91	3.25	
17	Rhyolite(2A3)	23.75	59.47	4.92	2.31				1.07		
18	Gabbro(E80A)	2.82	4.73	22.80	31.97	8.70	5.35	2.13	10.36	3.62	
19	Basalt(1A8)		10.76	26.22	24.52	6.55	3.93	1.72			9.75
20	Basalt(WJ-1-109)		7.47	29.22	25.23	7.65	4.89	1.67			11.60
21	Basalt(S95)		8.77	29.95	27.37	6.80	3.96	1.94			8.82

TABLE 9. COMPUTED "NORMS" OF SE1 C ROCK SAMPLES
(VOLUME %, INCORPORATING WATER) (Continued)

No.	Name	QTZ	ORTHO	ALB	ANOR	CP(WO)	CP(EN)	CP(FS)	OP(EN)	OP(FS)	OL(FO)
23	Basalt(la3)		6.68	29.09	30.79	5.29	2.89	1.74	3.97	2.10	4.97
24	Anorthosite (AN)	2.75	0.82	22.17	65.27	1.07	0.65	0.27	2.55	0.95	
25	Diabase	4.39	4.31	18.91	31.89	8.60	4.49	3.07	11.62	6.96	
26	Peridotite(EP-1)		0.60	1.36	3.84	2.26	1.75	0.21	14.89	1.53	64.57

TABLE 9. COMPUTED "NORMS" OF SET C ROCK SAMPLES
(VOLUME %, INCORPORATING WATER) (Continued)

No.	Name	OL(FA)	HEM	MAG	ILM	APA	CAL	COR	WAT	NEPH	WOL
1	Granite(A79)		0.23	0.03	0.06	0.02	0.11	0.45	1.03		
2	Granite(A119)			0.61	0.57	0.31	0.11	0.37	1.66		
3	Granite(A122)			0.65	0.21	0.08		0.52	1.94		
4	Rhyolite(SA-49)		0.26	0.93	0.26	0.08	0.11		3.64		
5	Rhyolite(Weld.Tuff)			0.72	0.13		0.11	0.71	4.06		
6	Pyroxene Syenite (E83A)		0.39	0.60	0.23	0.06	0.46	1.74	2.25		
7	Trachyte			0.74	0.25	0.06	0.53	2.89	2.17		
8	Neph.Syen.			1.40	0.87	0.17	0.11		2.58	14.12	0.47
9	Granodior.(A117)	1.99		1.01	1.12	0.20	0.11		0.95		
10	Granodior.(A127)			0.47	0.60	0.19	1.25	2.62			
11	Dacite(E12A)			0.90	0.38	0.32	6.07	4.12	3.32		
12	Dacite(2A1)			0.81	0.63	0.27	0.46	0.24	5.30		
13	Dacite(2B5)W			1.19	0.67	0.31	0.11	1.93	5.47		
14	Diorite(A129)			1.38	1.02	0.61	0.12		2.75		
15	Diorite(E47C)			1.42	0.96	0.60	0.12		2.00		
16	Andesite(E55A)			1.66	0.56	0.40	0.60		6.48		
17	Rhyolite(2A3)		0.86	0.04	0.46	0.17	0.82	1.17	4.43		
18	Gabbro(E80A)			3.29	1.02	0.26	0.12		2.76		
19	Basalt(LA8)	3.80		1.80	2.48	1.34	0.12		2.16	4.75	
20	Basalt(WI-1-109)	3.53		2.39	2.15	1.30	0.12		2.19	0.38	
21	Basalt(S95)	3.85		1.81	2.38	1.10	0.12		1.61	1.75	
23	Basalt(LA3)	2.66		1.71	2.23	0.81	1.85		2.82		

TABLE 9. COMPUTED "NORMS" OF SET C ROCK SAMPLES
(VOLUME %, INCORPORATING WATER) (Concluded)

No.	Name	OL (FA)	HEM	MAG	ILM	APA	CAL	COR	WAT	NEPH	WOL
24	Anorthosite(AN)			0.65	0.33	0.04	0.12		1.95		
25	Diabase			0.90	1.18	0.28	0.12		3.54		
26	Peridotite(EP-1)	6.74		0.21	0.13	0.10			1.82		

a basalt, was omitted because its calculated norm included a normative mineral which is not found in nature, and since there were enough other basalts to represent that rock type adequately.

There were two major reasons why the norms were used instead of modes as mineralogical parameters. First, it is difficult to perform quantitatively accurate modal analysis on aphanitic ground masses, which are present in some of the samples. The resulting modes can, therefore, be more descriptive of the phenocrysts than of the ground mass. The normative calculation, by contrast, is influenced equally by phenocrysts and ground mass, because the chemical oxides on which the calculation is based are bulk oxides obtained from wet chemical analysis of crushed samples. Since an infrared scanner or spectrometer looks at both phenocrysts and ground mass, the bulk properties should be better correlated with the infrared spectral features. Secondly, since the normative calculations of Table 9 are derived solely from the oxides of Table 5, the correlations of mineralogical and chemical parameters with $R_{1,2}$ can be directly compared, with little probability of unequal treatment because of mineral mis-identification or mis-estimate of volume percentage.

The normative computer program was found to agree well with a separate normative program of N. G. Ware [21] for calculated norms of several basic rock samples [22]. The norm of a rock may not closely agree with its mode, especially for pyroxene-rich rocks [22]. However, the norms and modes usually agree within a few percent for most igneous rocks, within the context of the summations implicit to the normative minerals (e.g., orthoclase encompassing all potassic feldspars).

Stepwise regressions were performed between $R_{1,2}$ and the computer norms of Table 9, which represent all of the samples in Set C. The best regression equation coefficients are given in Table 10. The coefficients in Table 10 can be used to establish a mineralogical index defined by the following equation:

$$M_{16} = B_0 + \sum_{i=1}^{16} B_i M_i \quad (8)$$

where M_{16} = mineralogical index for 16 mineral parameters

B_0 = constant coefficient (Table 10)

B_i = coefficient for i -th mineral parameter (Table 10)

M_i = volume % of i -th normative mineral

21. N. G. Ware, Department of Geophysics, Australian National University, Canberra, Private Communication, 1973.

22. E. Essene, Department of Geology and Mineralogy, The University of Michigan, Ann Arbor, Private Communication, 1973.

TABLE 10. REGRESSION OF THE M_{16} MINERALOGICAL INDEX
WITH $R_{1,2}$ FOR SET C

Mineral	Parameter No.	Coefficient
Olivine (Forsterite)	1	-.002417
Wollastonite	2	.350000
Water	3	-.013110
Hematite	4	-.112930
Albite	5	-.002834
Quartz	6	-.001032
Olivine (Fayalite)	7	.022932
Ilmenite	8	-.090608
Apatite	9	.120840
Orthopyroxene (Magnesium Rich)	10	.005732
Nepheline	11	-.006352
Corundum	12	.008251
Clinopyroxene (Iron Rich)	13	.189930
Clinopyroxene (Calcium Rich)	14	-.129250
Clinopyroxene (Magnesium Rich)	15	.128740
Orthopyroxene (Iron Rich)	16	-.011553
Constant	0	1.3606
Correlation(r)		.99
Standard Error (s.e.)		.009

The M_{16} mineralogical index is actually the predicted value of $R_{1,2}$, based on the regression represented by Table 10. The multiple correlation coefficient between M_{16} and measured values of $R_{1,2}$ from Table 7 is 0.99, with a standard error of 0.009 in $R_{1,2}$ —if M_{16} is used to predict the measured $R_{1,2}$. A plot of M_{16} versus $R_{1,2}$ is shown in Fig. 23.

Up to this point, the names associated with the rock samples have been those assigned by their respective collectors,* who named them on the basis of either hand specimen inspection or modal analysis, and probably according to slightly different schemes. In an attempt to place these rock classifications on a more uniform basis, each rock was reclassified according to Travis's classification of igneous rocks [23], on the basis of the volume percentage of normative minerals given in Table 9. Whenever the rock was a borderline case in this classification scheme, the collector's name for the specimen was retained. Table 11 shows the resulting new sample names, along with the old names, arranged in order of increasing $R_{1,2}$. Sample 22, not a member of Set C, is also given, with unchanged classification. In the next-to-last column, a group name is assigned to each sample, according to Travis's nomenclature. The group names are explained in Table 12.

The most important point to be made from Table 11 is that (as shown by the last two columns of Table 9) the $R_{1,2}$ ratio is not well correlated with the rock groupings of Travis's nomenclature. On this basis, only the I and J groups seem to be identifiable in the presence of other silicates. This brings out an important point: the minerals on which geologists have chosen to place greatest importance in their traditional rock classification schemes do not have the same relative importance with regard to their effect on the infrared properties of rocks. For instance, Travis's classification places greatest importance on quartz, potassic feldspar, feldspathoids, pyroxene, and olivine, with secondary importance on the relative amounts of sodic and calcic plagioclase. However, when a stepwise regression was performed to find the eight minerals most significant for predicting the infrared ratio, the results were forsterite, anorthite, wollastonite, water, magnetite, hematite, albite, and quartz—in that order. Since water, magnetite, and hematite have almost no infrared spectral features, they must influence the infrared ratio in some indirect manner. Quartz and forsterite have reststrahlen bands at the shortest (8.1-10.1 μm) and longest (10.2-12.2 μm) wavelengths of all the silicates. Albite and anorthite reststrahlen bands fall at 9.6-10.1 μm and 8.7-10.9 μm , respectively. Wollastonite (CaSiO_4), a pyroxenoid with a 1:3 silicon to oxygen ratio, is expected to have reststrahlen bands just

* These rocks were collected by several geologists and loaned to Dr. Lawrence Rowan of the U.S. Geological Survey, who in turn loaned them to Robert Vincent.

23. R. B. Travis, *Classification of Rocks*, Quarterly of the Colorado School of Mines, 50, 1955, p. 12.

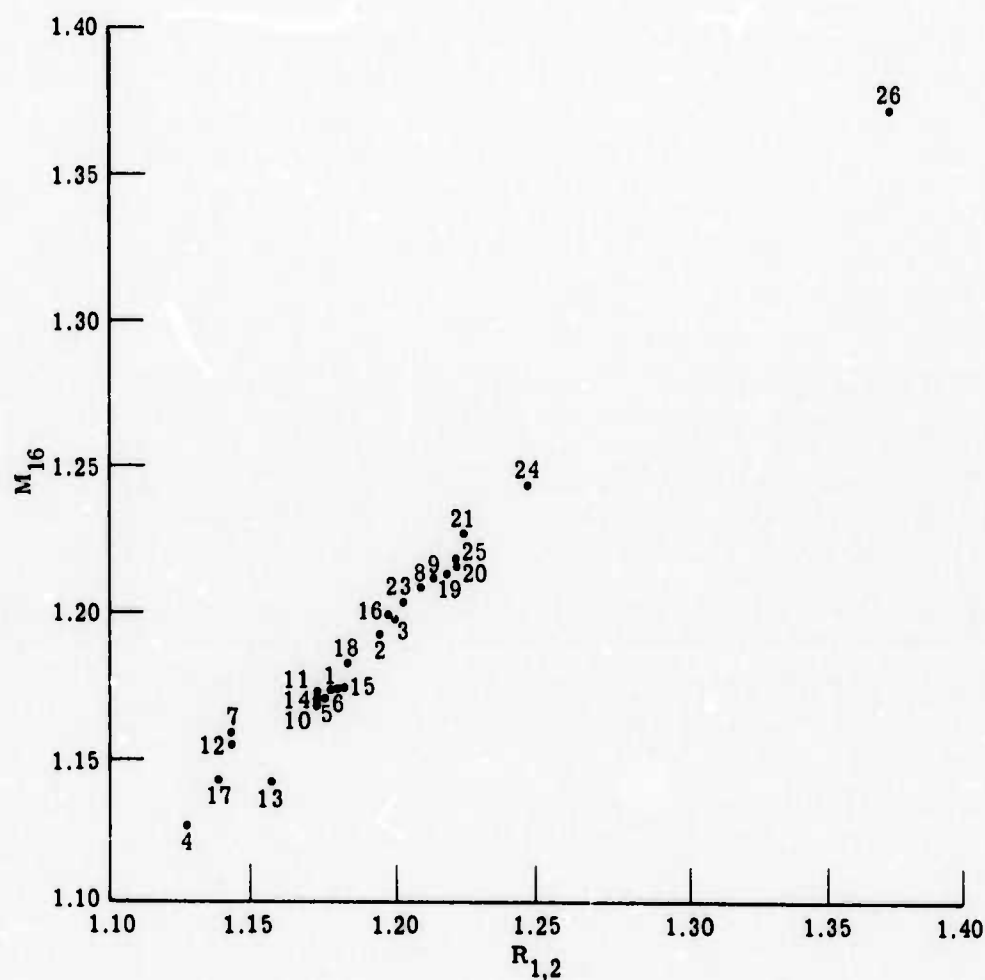


FIGURE 23. MINERALOGICAL PARAMETER M_{16} VERSUS $R_{1,2}$ FOR SET C

TABLE 11. RECLASSIFICATION OF ROCK SAMPLES ACCORDING TO
C.I.P.W. CALCULATIONS AND TRAVIS'S NOMENCLATURE

Sample No.	Sample Old Name	Sample New Name	Assigned Group	R _{1,2} Ratio
4	Rhyolite(SA-49)	Quartz Latite	D-3	1.1266
17	Rhyolite(2A3)	Rhyolite	A-3	1.1394
12	Dacite(2A1)	Dacite	G-3	1.1436
7	Trachyte	Quartz Latite	D-3	1.1442
13	Dacite(2B5)W	Dacite	G-3	1.1574
14	Diorite(A129)	Granodiorite	G-1	1.1685
10	Granodiorite (A127)	Quartz Monzonite	D-1	1.1723
11	Dacite(E12A)	Quartz Latite Porphyry	D-2	1.1724
5	Rhyolite (Welded Tuff)	Quartz Latite	D-3	1.1741
1	Granite(A79)	Quartz Monzonite	D-1	1.1761
6	Pyroxene Syenite (E83A)	Pyroxene Syenite	B-1	1.1784
15	Diorite(E47C)	Diorite	H-1	1.1795
18	Gabbro(E80A)	Gabbro	I-1	1.1810
2	Granite(A119)	Quartz Monzonite	D-1	1.1946
16	Andesite(E55A)	Dacite	G-3	1.1962
3	Granite(A122)	Quartz Monzonite	D-1	1.1987
23	Basalt(1A3)	Basalt	I-3	1.2018
8	Nepheline Syenite	Nepheline Monzonite	F-1	1.2094
9	Granodiorite (A117)	Diorite	H-1	1.2134
19	Basalt(1A8)	Basalt	I-3	1.2154
25	Diabase	Diabase	I-1	1.2204
20	Basalt(WI-1-104)	Basalt	I-3	1.2204
21	Basalt(S95)	Basalt	I-3	1.2246
22	Basalt(5B4)	Basalt	I-3	1.2255
24	Anorthosite	Anorthosite	I-1	1.2458
26	Peridotite	Peridotite	J-1	1.3723

TABLE 12. ASSIGNMENT OF GROUP CLASSIFICATIONS ACCORDING TO TRAVIS'S NOMENCLATURE

Symbol	Interpretation
A	Potassic Feldspar >2/3 Total Feldspar, Quartz >10%
B	Potassic Feldspar >2/3 Total Feldspar, Quartz <10%, Feldspathoid <10%
C	Potassic Feldspar >2/3 Total Feldspar, Feldspathoid >10%
D	Potassic Feldspar 1/3 to 2/3 Total Feldspar, Quartz >10%
E	Potassic Feldspar 1/3 to 2/3 Total Feldspar, Quartz <10%, Feldspathoid <10%
F	Potassic Feldspar 1/3 to 2/3 Total Feldspar, Feldspathoid >10%
G	Plagioclase >2/3 Total Feldspar, Potassic Feldspar >10% Total Feldspar, Quartz >10%
H	Plagioclase >2/3 Total Feldspar, Potassic Feldspar <10% Total Feldspar, Quartz <10%, Feldspathoid <10%, Sodic > Calcic Plagioclase
I	Plagioclase >2/3 Total Feldspar, Potassic Feldspar <10% Total Feldspar, Quartz <10%, Feldspathoid <10%, Calcic > Sodic Plagioclase
J	Little or No Feldspar, Chiefly Pyroxene and/or Olivene
1	Phaneritic Texture
2	Porphyritic Texture
3	Aphanitic Texture

short of those for anorthite, since both contain Ca-O bonds. In the stepwise regression for M_{16} , anorthite and magnetite were eventually replaced by other minerals

The fact remains that $R_{1,2}$ discriminates among silicates on the basis of the M_{16} mineralogical parameter, which is different from the basis of traditional rock classification schemes. Table 13 shows the M_{16} values, in ascending order, for the rock samples of Set C. Also shown in Table 13 is a suggested classification scheme based on values of M_{16} . Category III contains mostly basalts and diabase, Category IV is anorthosite and possibly some other very basic rocks, and Category V is strictly ultrabasic. Categories I and II are not well correlated with rock groups based on Travis's nomenclature, except that group I contains five of the seven fine-grained volcanic samples. This could be indicative of a textural effect on $R_{1,2}$ for acidic rocks. However, this effect could be indirectly caused by composition—for example, the D-3 and G-3 samples in group I all have higher % water than the D-1 and G-1 samples, respectively.

The value of Eq. (8) is that if a geologist knows the norms of a collection of his rocks, he can calculate M_{16} (which is really the best predicted value of $R_{1,2}$) without having to make infrared laboratory measurements on the rocks. If the detector which measures $R_{1,2}$ is flown at 1 km above the ground over his test site, the $R_{1,2}$ values measured by the scanner can then be used to help him decide which of the rocks in his collection a given outcrop (seen on the $R_{1,2}$ ratio image) could or could not be. Given an $R_{1,2}$ value, the problem of determining the standard deviations in M_{16} is a difficult statistical one involving inverse regression methods for several independent parameters (the mineral volume percentages in this case). This problem has not been solved, and it was not the subject of any published statistical papers between 1961-69 [24]. To estimate crudely this standard deviation in M_{16} (or predicted value of $R_{1,2}$), given the value of $R_{1,2}$, one can compare the M_{16} values from Table 13 with the $R_{1,2}$ values of Table 11. The largest disagreement between M_{16} and $R_{1,2}$ is 0.011. Therefore, the standard deviation from predicting M_{16} from measured $R_{1,2}$ can be estimated as approximately $\sigma_1 = 0.01$. The estimated standard deviation from an error in the measurement of $R_{1,2}$ is approximately $\sigma_2 = 0.007$. The combined standard deviation, assuming that additive errors can be expressed as in Wilson [25], is

$$\sigma = \sqrt{\sigma_1^2 + \sigma_2^2} = 0.012 \quad (9)$$

24. B. L. Joiner, N. F. Laubscher, E. S. Brown, and B. Levy, An Author and Permuted Title Index to Selected Statistical Journals (1961-1969), National Bureau of Standards Publication 321, U.S. Department of Commerce, Washington, 1970.

25. E. B. Wilson, Jr., An Introduction to Scientific Research, McGraw-Hill Book Co., Inc., New York, 1952, p. 273.

TABLE 13. A CLASSIFICATION BASED ON THE M_{16} MINERALOGICAL INDEX

Sample No.	Old Sample Name	New Sample Name	Travis's Groups	M_{16} Groups	M_{16}
4	Rhyolite	Quartz Latite	D-3		1.1255
13	Dacite	Dacite	G-3		1.1412
17	Rhyolite	Rhyolite	A-3	I (≤ 1.160)	1.1423
12	Dacite	Dacite	G-3		1.1555
7	Trachyte	Quartz Latite	D-3		1.1578
10	Granodiorite	Quartz Monzonite	D-1		1.1691
14	Diorite	Granodiorite	G-1		1.1702
5	Rhyolite	Quartz Latite	D-3		1.1708
11	Dacite	Quartz Latite Porphyry	D-2		1.1726
1	Granite	Quartz Monzonite	D-1		1.1740
6	Pyroxene Syenite	Pyroxene Syenite	B-1	II (1.160-1.200)	1.1741
15	Diorite	Diorite	H-1		1.1793
18	Gabbro	Gabbro	I-1		1.1823
2	Granite	Quartz Monzonite	D-1		1.1931
16	Andesite	Dacite	G-3		1.1996
23	Basalt	Basalt	I-3		1.2033
8	Nepheline Syenite	Nepheline Monzonite	F-1		1.2094
9	Granodiorite	Diorite	H-1		1.2115
19	Basalt	Basalt	I-3	III (1.200-1.230)	1.2146
20	Basalt	Basalt	I-3		1.2181
25	Diabase	Diabase	I-1		1.2188
21	Basalt	Basalt	I-3		1.2271
24	Anorthosite	Anorthosite	I-1	IV (1.230-1.270)	1.2446
26	Peridotite		J-1	V (≥ 1.270)	1.3724

Twice this standard deviation is 0.024, which represents the minimum separation in M_{16} value that two rocks must have in order to be discriminated with a 68% probability of success by a measurement of $R_{1,2}$.

Although the M_{16} index is the best single parameter correlated with $R_{1,2}$ (until the statistical base of rock samples is extended beyond the 25 samples of Set C), the geologist may find that a mineralogical index that is more simply determined is more useful with rock samples for which he has no rapid rock analyses. In that case, it would be helpful to have a mineralogical parameter based only on minerals recognizable with a hand lens or polarizing microscope. Table 14 shows the results for Set C of confining the mineralogical parameters to quartz, anorthite, nepheline, olivine (forsterite plus fayalite), magnetite, and orthoclase. Because of the nature of C.I.P.W. calculations, anorthite represents all calcic plagioclase and orthoclase represents all potassic feldspars. Olivine for Table 14 was taken to be sum of forsterite and fayalite. The resulting simplified mineralogical index is as follows (where % refers to volume %):

$$M_6 = 1.2081 - 0.0008(\% \text{ Quartz}) + 0.0007(\% \text{ Calcic Plagioclase}) + 0.0027(\% \text{ Nepheline}) \\ + 0.0023(\% \text{ Olivine}) - 0.0169(\% \text{ Magnetite}) - 0.0005(\% \text{ Potassic Feldspar}) \quad (10)$$

The correlation between M_6 and $R_{1,2}$ is 0.94; the standard error in $R_{1,2}$ when the latter is the independent variable is 0.019. The estimated combined standard deviation in M_6 when $R_{1,2}$ is known (calculated in the same manner as that for M_{16} in Eq. (9) is 0.030. Though M_6 is more convenient than M_{16} , the estimated standard deviation is 2.5 times as large. If the M_6 index for two rocks differs by more than 0.060, there is a 68% probability that the rocks can be discriminated. A plot of M_6 versus $R_{1,2}$ is shown in Fig. 24. The M_6 parameter is not very useful for acidic rocks.

5.2 GEOLOGIC APPLICATIONS FOR THE $R_{1,2}$ INFRARED RATIO IMAGING METHOD

The two-channel infrared ratio imaging method (described in previous sections), plus a third channel for temperature correction, is a new tool which can be useful for discriminating among silicate rocks and, to a more limited degree, for identifying unknown silicate targets as belonging to a certain group of rocks. Although the rock groups recognized by the $R_{1,2}$ ratio are different from groups defined by traditional rock classification schemes, the ratio does considerably reduce the number of rocktype possibilities which an unknown target can be. Though infrared ratio imaging is new, there are some geological applications for which it may be useful, even in its present state of development.

The end members of the silicate rocks, namely the highly acidic and ultrabasic rocks, are relatively simple to discriminate from other silicates. Therefore, the most straightfor-

TABLE 14. REGRESSION OF THE M_6 MINERALOGICAL INDEX
WITH $R_{1,2}$ FOR SET C

<u>Mineral</u>	<u>Parameter No.</u>	<u>Coefficients</u>
Quartz	1	-.000798
Anorthite	2	.000704
Nepheline	3	.002673
Olivine (All)	4	.002264
Magnetite	5	-.016910
Orthoclase	6	-.000511
Constant	0	1.208100
Correlation (r)		.94
Standard Error (s.e.)		.019

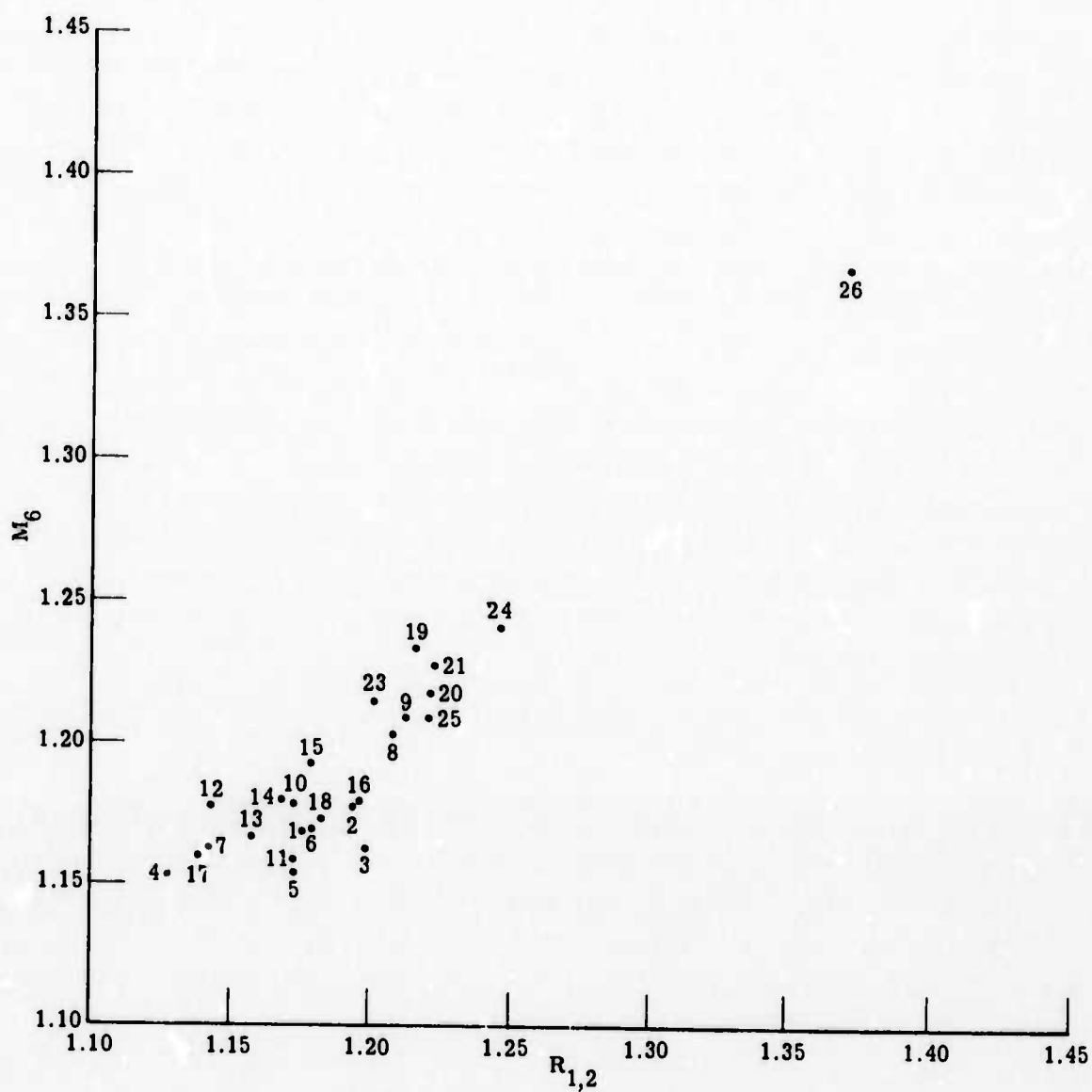
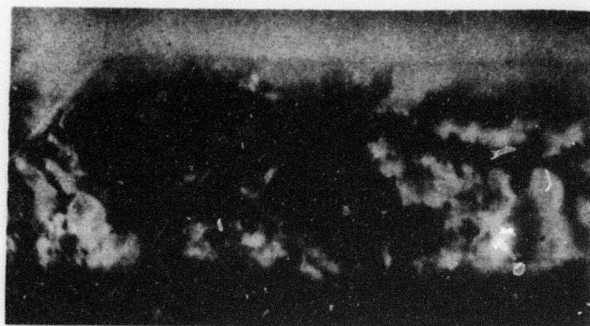


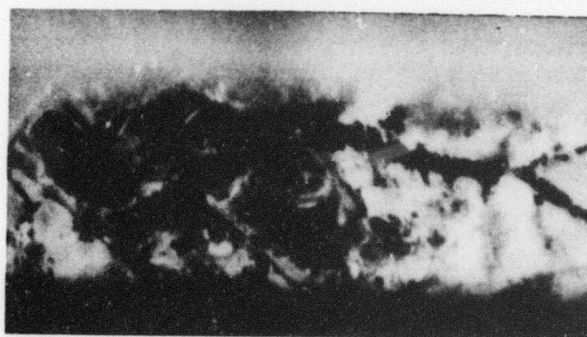
FIGURE 24. MINERALOGICAL PARAMETER M_6 VERSUS $R_{1,2}$ FOR SET C

ward geological applications of the infrared ratio method include exploitation of these end members. At one extreme, highly acidic rocks can be identified on the basis of their low $R_{1,2}$ infrared ratio, such as the quartz sand and sandstone shown in Fig. 25. Three obviously related applications are exploration for construction materials, beach surveys, and sand dune mapping. Sand and gravel (chert has a ratio approximately equal to that of quartz) deposits can be easily spotted by this method, in night or day operation. Concerning the second application, the difference between quartz and calcite ratios is so pronounced that beach surveys with a two-channel thermal infrared scanner should permit the accurate mapping of quartz-calcite sand boundaries, even though both minerals are difficult to discriminate by eye and practically impossible to discriminate by photography. Third, quartz sand-dune surveys likewise should be aided by this method because of the sharp contrast produced in $R_{1,2}$ between quartz sand and most other natural materials. Quartz sand dunes should appear distinct from calcite and gypsum sand dunes, also. At the other extreme, peridotites and other ultrabasic rocks are easily discriminated from other silicates and other natural materials, a fact which leads to such potential uses as exploration for ophiolites or kimberlites. Ophiolites, thought to be remnants of fossil subduction zones, are basic and ultrabasic complexes usually found in rugged, mountainous terrain, where remote sensing would be highly desirable. Kimberlites, which may be economically important, should also be identified as ultrabasic complexes by the infrared ratio method.

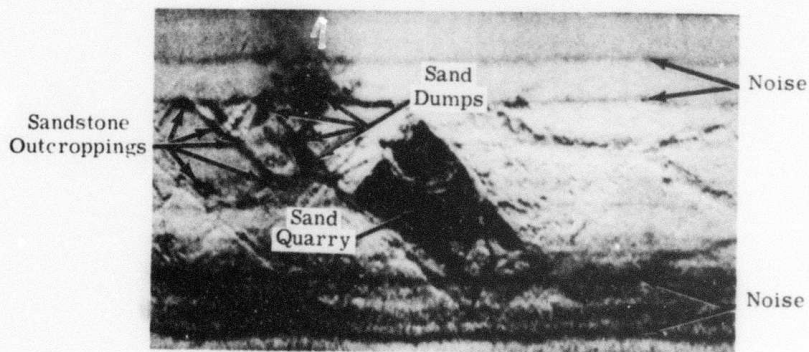
There are types of applications which depend primarily on the infrared ratio for discrimination alone (not for identification). One is the mapping of volcanic ash flows in the presence of similarly colored alluvium. Figure 26 is a blow-up of an $R_{1,2}$ ratio image from a region near Pissgah Crater, California, alongside a color aerial photo taken simultaneously with the scanner data. The rhyolitic tuff areas (marked T) are darker than the less acidic alluvium in the infrared ratio image, but indistinguishable from the alluvium in the color photo. Ash flows have traditionally been difficult to map by visible means; the infrared ratio method may be helpful in solving this problem. As a sidelight, the rhyolitic tuff in this intermittent stream bed near Pissgah Crater contains malachite (a copper ore) but not in large enough quantities to be economically important. This brings up the subject of mineralogical exploration, which will no doubt be impacted by this new method for those problems associated with great local % SiO_2 variations. In some cases, such as the rhyolitic tuff, the host rock for the ore or precious mineral may be discriminable from other rocks in the scene by $R_{1,2}$. In other cases, the ore itself may be more easily discriminated from similarly colored rocks by the infrared ratio. For example, iron formation members can be high in silica content as compared to dark shales, and yet the two can be equally dark in the visible wavelength region. Concerning iron and several other metallic ores, the $R_{1,2}$ ratio may be of use in discriminating widely different metamorphic facies. For intermediate temperatures and pressures, the green-



(a) Channel 1: 8.2-10.9 μm

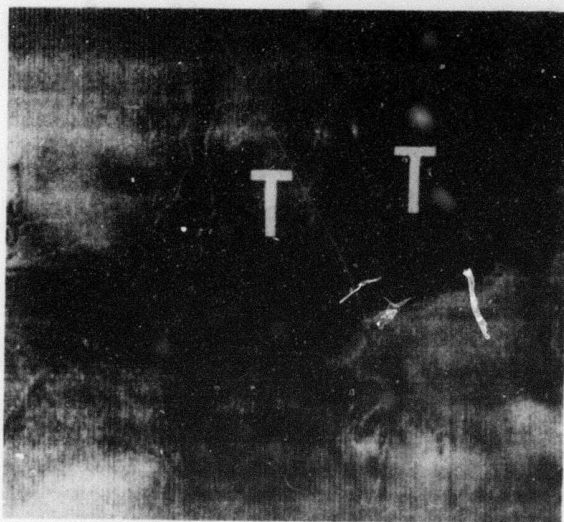


(b) Channel 2: 9.4-12.1 μm

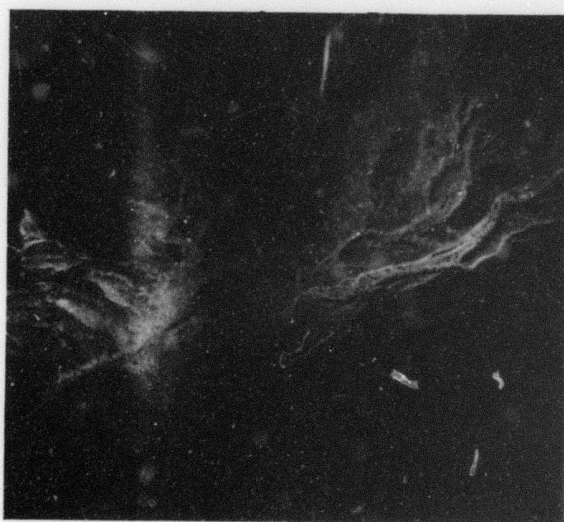


(c) Ratio Image of Channel 1 over 2

FIGURE 25. DISCRIMINATION OF ACIDIC SILICATES NEAR MILL CREEK, OKLAHOMA. (Sand quarry).



Infrared Ratio Image



Aerial Photo

FIGURE 26. COMPARISON OF THERMAL INFRARED RATIO IMAGE WITH AN AERIAL PHOTO FOR A RHYOLITIC TUFF (DARK ON RATIO IMAGE, MARKED BY T) ASSOCIATED WITH MALACHITE. Near Pisgah Crater, California. North is toward the top and the images are approximately 1.5 km on a side.

schist facies contains no pyroxene and less calcic plagioclase than the pyroxene granulite facies, which does contain pyroxenes [26]. If the M_{16} mineralogical index (which was determined for igneous silicates) also happens to be valid for metamorphic rocks, the green-schist and pyroxene granulite facies may be discriminable by the ratio imaging method.

The infrared ratio purely as a discriminant can also be useful in general geologic mapping, especially when the region being mapped is fairly well known and the rock types are of similar color — but quite different infrared ratios are present (e.g., some anorthosites and light-colored felsite, granite and limestone, etc.). In a similar way, the method should be useful in soil-mapping, although there may be larger % ($\text{SiO}_2 - \text{Al}_2\text{O}_3$) variations with depth of soil horizon than with different soil species.

Finally, the infrared ratio method can also be used in an absolute sense to help identify silicate rock types over unknown terrain. For instance, if a rock is dark in the visible region and has an $R_{1,2}$ ratio near 1.2, it is most likely a basalt — and definitely not a peridotite. Using the visible color and $R_{1,2}$ ratio value, the rock-type can be narrowed to a few possibilities. This would be most useful in extraterrestrial remote sensing and in reconnaissance mapping of inaccessible terrain on earth (where ground truth is sparse, if available at all). However, since atmospheric effects can change the magnitude of the infrared ratio, new ratios must be calculated for the specific experiment performed. In remote sensing from earth satellites, for instance, the total earth atmosphere must be accounted for: this problem can and will be attacked both by extension of present atmospheric models and by empirical atmospheric parameters determined from Skylab infrared spectrometer measurements [27].

5.3 CONCLUSIONS

A method has been presented whereby compositional differences among silicate rocks can be imaged by infrared scanners capable of recording two or three channels in the 8- to 14- μm wavelength region. The ratio of two infrared channels has been related to chemical and mineralogical parameters for a suite of widely varied igneous silicate rocks. Infrared measurements were made on naturally exposed surfaces of these rock samples, and an infrared ratio ($R_{1,2}$) was calculated for each rock under the following experimental conditions: an aircraft altitude 1 km above ground, a clear dry atmosphere, and two infrared channels defined by a particular two-element detector currently in use.

26. W. G. Ernst, *Earth Materials*, Prentice-Hall, Inc., Englewood Cliffs, 1969, p. 135.

27. R. K. Vincent, *The NASA Earth Resources Spectral Information System: A Data Compilation — Second Supplement*, Environmental Research Institute of Michigan, Technical Report No. 31650-156-T, NASA Contract NAS9-9784, 1973.

Chemical parameters, consisting of oxide weight percentages, were measured by rapid rock analysis. Mineralogical parameters, consisting of volume percentages of natural minerals, were calculated from a C.I.P.W. computer program, with the oxides as inputs. Forward linear regressions showed that chemical parameters are better correlated with $R_{1,2}$ than mineralogical parameters for up to approximately six variables. For more than six variables, the mineralogical parameters are better correlated with $R_{1,2}$. The best single parameter is % SiO_2 , and the best two-parameter combination is % $[\text{SiO}_2 + 5.4(\text{Fe}_2\text{O}_3)]$, with % $(\text{SiO}_2 - \text{Al}_2\text{O}_3)$ a close second. The best overall compositional parameter is a mineralogical index (M_{16}), which is based on the volume percentages of 16 materials. Another mineralogical index (M_6), which is based on six easily identified minerals, was created for use with rock collections which have only partial modal analysis results.

The minerals which are most important in traditional rock classification schemes do not have the same relative importance in relation to their control of infrared spectral features. Thus, the $R_{1,2}$ infrared ratio does discriminate among silicate rocks, but not on the same basis as petrologists. The M_{16} mineralogical index, which is the best compositional basis for describing the $R_{1,2}$ discrimination, was divided into five silicate categories. Only three of these categories are comparable to traditional rock classifications.

The infrared ratio imaging method was applied to two test areas with good agreement between scanner-measured and theoretically calculated values of $R_{1,2}$. In the area around Mill Creek, Oklahoma, quartz sand and sandstone were readily discriminated from other natural materials (including other silicates such as topsoil, and nonsilicates such as carbonates and vegetation). In the area around Pisgah Crater, California, dacites and basalts were clearly discriminated and were identifiable on the basis of their infrared ratio values. On a relative basis, a rhyolitic tuff was discriminable from surrounding alluvium on the basis of the $R_{1,2}$ infrared ratio, whereas the two could not be separated by color air photographs in the visible wavelength region.

Several geologic applications have been suggested for the infrared ratio method. They include the following:

- (1) exploration for construction materials (sand and gravel)
- (2) surveying beaches (quartz versus calcite sands) and mapping sand dunes
- (3) exploration for ophiolites
- (4) mineralogical exploration
- (5) mapping of volcanic ash flows
- (6) reconnaissance geologic mapping of inaccessible terrain

SOIL INFORMATION FROM REMOTE SENSOR IMAGERY

6.1 INTRODUCTION

Both large-scale generalized and detailed soil information are required for tunnel site selection and subsequent tunnel construction. The exact location and method of detailed soil investigations are determined on the basis of preliminary site inspection surveys [28] and interpretation of available maps, reports, and imagery. It is the purpose of this section to describe some of the types of soil information which may be obtained from modern remote sensor data—particularly multispectral scanner data.

6.1.1 APPROACH

Two approaches may be utilized for obtaining soil information from remote sensor data. One approach is to interpret spatial terrain patterns from the imagery and to infer the nature and extent of soils on the basis of the interpreter's understanding of soil-environmental relationships—particularly those of vegetative, topographic, and drainage patterns. This is the path of conventional image interpretation, concerning which there are a number of useful references [29-31]. The second approach is to analyze only those portions of the imagery in which the soil may be observed directly. Here we attempt to discern soil conditions and patterns solely from the appearance of these bare areas. This approach, although spatially limited to those portions of the terrain in which soil is exposed to aerial view, is particularly suitable for the application of automated processing and image enhancement techniques. Consistent image patterns and tones are assumed to represent similar soil conditions; these may then be automatically enhanced or selectively delineated with current computer processing techniques. But since these techniques are designed to apply to specific terrain conditions, their effects on non-bare (vegetated) areas are not always predictable. Thus, this section is primarily concerned with lithological applications of the second approach, although enhancement of vegetative differences as indicators of soil conditions is also discussed.

28. K. Szechy, *The Art of Tunneling*, Akademiai Kiado, Budapest, 1967.

29. R. E. Frost, et al., *Photointerpretation of Soils, Manual of Photographic Interpretation* (R. N. Colwell, ed.), Am. Society of Photogrammetry, 1960, pp. 343-402.

30. V. C. Miller and S. A. Schumm, *Aerial Photographs and Surface Features, Aerial Surveys and Integrated Studies: Proceedings of the Toulouse Conference, UNESCO, Paris, 1968*, pp. 41-79.

31. A. H. Gerbermann, H. W. Gausman, and C. L. Wiegand, *Color and False Color-IR Films for Soils Identification, Photogrammetric Engineering*, Vol. 37, No. 4, 1971, pp. 359-364.

6.1.2 BACKGROUND

In tunnel site selection, soil information is especially important for shallow-depth tunnels and in the placement and construction of tunnel portals. Soil information may also be important as an indicator of subsurface hydrologic and lithologic conditions over the length of the tunnel location. In other words, since specific soils are derived from certain lithologic parent materials under given environmental conditions, natural soil permeability and drainage may greatly affect subsurface hydrologic conditions. In general, both on-site observations and interpretation and analysis of aerial images are required. Precise quantitative methods have been developed for describing and sampling soils in vertical profiles in the field. Soil samples are also extensively analyzed and tested in the laboratory. The challenge is to extrapolate these observations to the surroundings and to obtain accurate knowledge of important spatial variations in soil conditions over the tunnel site location. It is estimated that for a survey of intermediate scale, only 1/5,000,000 of the soil is actually observed from borings in the field. Consequently, the soil engineer must rely on the art of image interpretation in mapping soils. He not only requires an understanding of soil morphology and genesis, but more importantly, he also must know the relationships of soil physics to geological materials, landforms, topography, vegetation, and natural drainage.

Current survey practice often makes use of aerial photographs as a mapping base and for interpreting the area over which field observations are applicable. In some initial reconnaissance surveys, aerial photographs largely substitute for extensive field observations.

In working with images we have recognized certain limitations to the film-camera system which have led to the development of other types of aerial and orbital sensors. Potentially the newer systems provide additional, useful terrain imagery to the soil scientist or engineer. The potential of one such system, the multispectral scanner, stems from the large amount of spatial and spectral data collected and from the compatibility of these data with modern processing facilities. Some of the information concerning soils that a multispectral scanner system may provide is discussed below. In addition, a practical approach for realizing this potential is suggested.

6.1.3 A MULTISPECTRAL SYSTEM

For purposes of this discussion it is important to briefly consider three characteristics of multispectral systems: the spectral range and resolution over which they are sensitive, the manner in which the data are recorded and stored, and several of the methods available for retrieving information from these data.

Imagery used in this study was obtained from the experimental ERIM M-7 airborne scanner system [32]. This system synchronously collects 12 bands of data from a choice of 19 bands over the 0.32- to 13.5- μm spectral range. This range includes radiation in the ultraviolet, visible, near infrared, and thermal infrared portions of the electromagnetic spectrum. The scanner has a maximum 2-milliradian spatial resolution and a 90° total field of view.

The 12 bands are recorded in the aircraft on computer-compatible, multitrack, analog magnetic tape; this allows subsequent electronic processing and image enhancement of these data. Shown in Fig. 27 are the tape-recorded signal levels associated with each of 12 bands for a given scanline of a scanner image. Internal radiation reference sources which allow subsequent calibration of the imagery are also recorded along with the imagery. The data illustrated were recorded from the Bureau of Mines, multispectral-scanner flight over a portion of the Black Hills in South Dakota (as discussed previously in this report).

The simplest method of retrieving these tape-recorded data is to photograph sequentially a CRT video image of each of the 12 spectral bands. Each image portrays the terrain in a single spectral band (as shown in Fig. 27). Contrasts in the ultraviolet, visible, and near-infrared bands are a result of solar illumination, terrain aspect, scanner look-angle, and surface reflectance characteristics. The thermal infrared band shows contrasts related to the absolute temperature and emittance characteristics of the terrain materials—warmer areas are characterized by lighter tones. Although video images of selected bands have been found useful in displaying contrasts associated with certain terrain features, no single band has proved consistently useful for identifying soil conditions. However, full use of the information contained in multispectral data requires simultaneous analysis of a number of bands in combination.

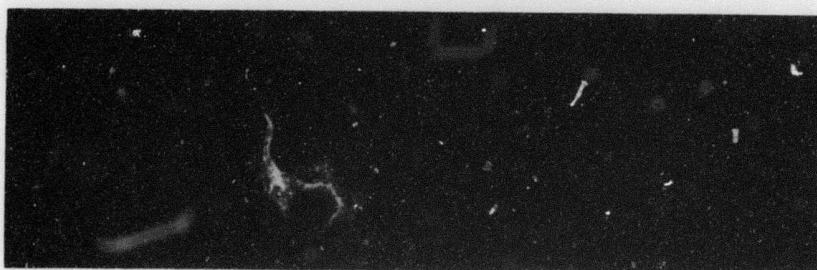
Powerful statistical techniques have been developed for use with computers to automatically recognize scene elements on the basis of their unique spectral characteristics in up to 12 bands. These techniques have been used experimentally for mapping the distribution of soils in areas bare of vegetation. Several limitations of this technique, however, preclude its consideration as an operational method at present. These include the large amount of a priori soil information required to train the computer and validate the results [33], the heterogeneity of terrain

32. P. G. Hasell, Jr., Michigan Experimental Multispectral Scanner System, Proceedings of 4th Annual Earth Resources Review, NASA, January 17-21, 1972, pp. 34-1 through 34-13.

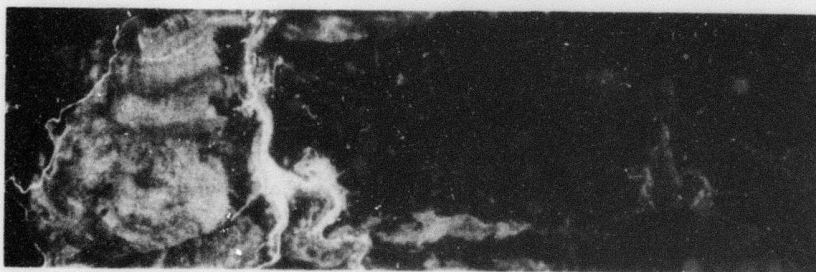
33. G. Nagy, G. Shelton, and J. Toloba, Procedural Questions in Signature Analysis, Proceedings of the 7th International Symposium on Remote Sensing of Environment, Vol. II, May 1971, pp. 1387-1401.



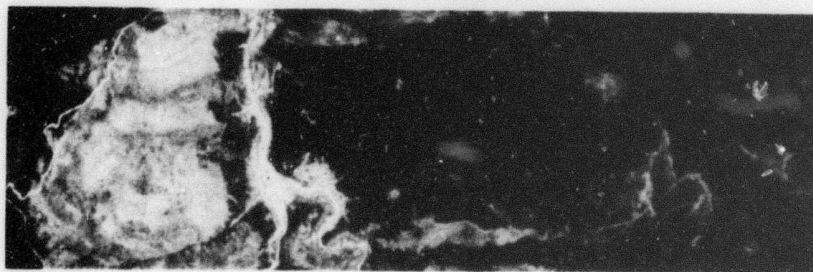
(a) USGS Topographic Map Section



(b) Ultraviolet (0.33-0.38 μm)



(c) Violet (0.41-0.48 μm)

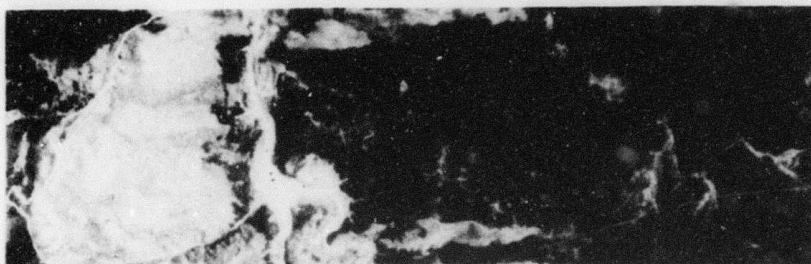


(d) Blue (0.46-0.49 μm)

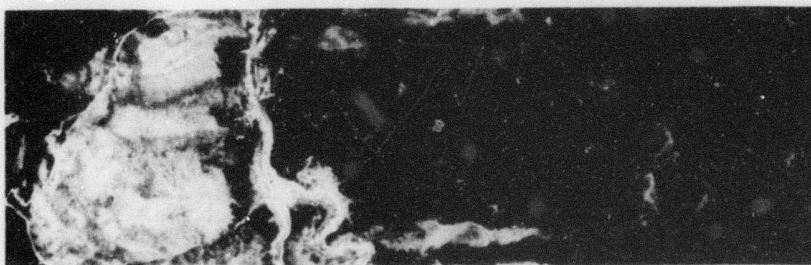
FIGURE 27. MULTISPECTRAL IMAGERY DISPLAY. Black Hills, South Dakota, 21 May 1972, 1100 hr, 5000 ft altitude.



(e) Green (0.50-0.54 μm)



(f) Yellow (0.55-0.60 μm)

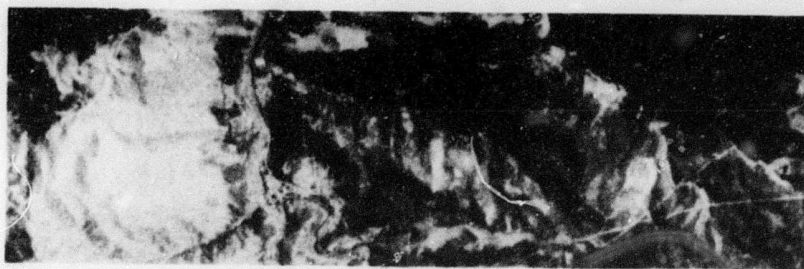


(g) Red (0.62-0.70 μm)

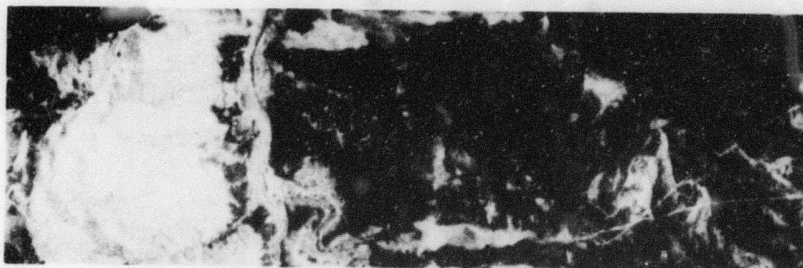


(h) Near Infrared (0.67-0.94 μm)

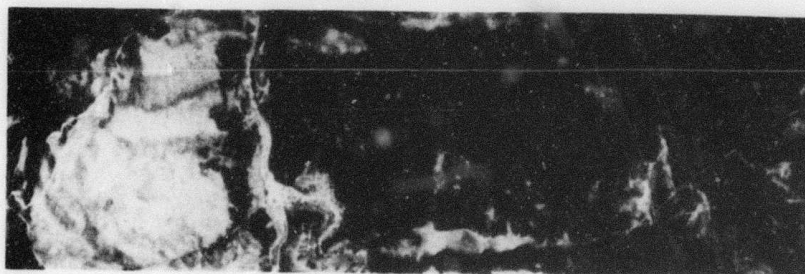
FIGURE 27. MULTISPECTRAL IMAGERY DISPLAY. Black Hills, South Dakota, 21 May 1972, 1100 hr, 5000 ft altitude. (Continued)



(i) Infrared (1.0-1.4 μm)



(j) Infrared (1.5-1.8 μm)



(k) Infrared (2.0-2.6 μm)



(l) Thermal Infrared (9.3-11.7 μm)

FIGURE 27. MULTISPECTRAL IMAGERY DISPLAY. Black Hills, South Dakota, 21 May 1972, 1100 hr, 5000 ft altitude. (Concluded)

surface which limits the extension of statistical recognition criteria [34], and the large costs associated with data analysis and recognition processing. These are discussed further in Section 6.3.

For tunnel-site selection purposes, we require a procedure that produces spatial soil information which is not readily available from less expensive aerial photographic systems, allows use of the engineer's knowledge of soils and local terrain conditions prior to and subsequent to image production, and is economically cost effective. Thus, Section 6.4 of this report is concerned with the constraints on operational multispectral systems for identifying and mapping soil conditions.

6.1.4 SOIL REFLECTANCE

Implicit in the use of imaging systems for identification of soil conditions is the assumption that the reflectance or emittance characteristics of soils are wavelength-dependent and relatively specific for differing physical conditions. In other words, the physical and chemical nature of soils affect certain radiation absorption characteristics, and these effects are observable from aerial platforms.

In selecting spectral bands to use, we must know something about the spectral characteristics of soils. Very general relationships of soil conditions to their reflectances have long been noted but seldom quantitatively investigated. Soil reflectance generally increases monotonically with increasing wavelength over the ultraviolet, visible, and near infrared portions of the spectrum. Most frequent observations concern the more-or-less uniform decrease in soil reflectance with increasing moisture content, increasing percentages of organic matter, and increasing particle or aggregate sizes. Also noted are differences in visual color related to the form and amount of iron oxides.

In a study of 160 surface soil samples collected from 36 states, Condit [35] showed only three significant variations in the shapes of spectral reflectances curves for the 0.3- to 1.0- μm range: a relatively linear increase with increasing wavelength (Chernozem type), a convex shape resulting from lower rates of increase in reflectance beyond about 0.6 μm (pedalfer type), and an inverted S-shaped curve resulting from a leveling or slight decrease and then an increase in reflectance beyond 0.7 μm (lateritic type). In other words, only slight variations

34. R. F. Nalepka and J. P. Morgenstern, Signature Extension: An Approach to Operational Multispectral Surveys, Environmental Research Institute of Michigan, Report No. 3165-152-T, 1973.

35. H. R. Condit, Application of Characteristics Vector Analysis to the Spectral Energy Distribution of Daylight and Spectral Reflectance of American Soils, Applied Optics, Vol. 11, No. 1, 1972, pp. 74-86.

in the shapes of reflectance curves appear to occur as a result of differences in soil conditions. Average reflectance (albedo) levels vary quite greatly, however.

Color contrasts have long been used as an easily observable soil property which may indicate more important soil differences. Differences in surface color may indicate the location of different soil types or degrees of surface erosion. (Some of the older soil taxonomic systems maintain a strong emphasis on color as a classification criterion.) Since the late 1940's, soil colors have been routinely recorded in the field through use of the semi-quantitative Munsell color standards [36].

6.2 RATIOED IMAGES

Intermediate to the simple playback of single video images and the multiband statistical recognition of scene features is the ratioing of two bands of multispectral data. Using an image processor, it is a relatively inexpensive and simple procedure that divides the recorded signals in one band by those in another to produce a new (ratioed) image.

This new image, which is a derivative of the two original bands, displays, by variations in tone, those areas which have differing amounts of spectral change from one band to the other. In other words, the contrasts inherent in the ratioed image result from the relative differences between the two bands and are not dependent on absolute signal levels in either band. This fact is important. A ratio image is fundamentally different from a single-channel video image, in spite of the superficial similarity of the ratioed image to a single-band video image—or to an aerial photograph for that matter. The ratioed image is less dependent on illumination, temperature, and directional variations of the scene, and it is more nearly a function of terrain reflectance or emittance characteristics than the radiance levels recorded in any one band. The ratio also tends to emphasize subtle spectral differences when signal levels in the denominator are low—a feature of the hyperbolic nature of ratios.

6.2.1 MUNSELL HUE

In an experiment (for the USDA Experiment Station at Weslaco, Texas) to delineate soils from multispectral data, it was noted that the 11 soil types differed in their redness, or dominant Munsell hue [37]. Eight were in the 5 YR (Yellow-Red) range and three were in the 10 YR range.

36. J. A. Shields, et al., Measurements of Soil Color, Canadian Journal of Soil Science, Vol. 46, 1966, pp. 83-90.

37. A. H. Munsell, A Color Notation, Munsell Color Co., Inc., Baltimore, 1947.

Two types of spectral curves were obtained from multispectral data of 20 soil sample locations. Illustrated in Fig. 28, these two types of curves clearly distinguish the 10 YR from the redder 5 YR soils, although considerable variation in the absolute levels occurs within each type. (The maximum and minimum for each type are shown.) The primary difference between the two types of curves occurs in the rate of increase between the 0.52 μm (green) and the 0.62 μm (red) wavelength range. The redder 5 YR soils more than double their reflectance, while the 10 YR soils remain about the same over this range. This fact suggested that the soils of this area could be separated on the basis of Munsell hue by a simple ratio of the 0.61 to 0.70 μm (red) band to the 0.50 to 0.54 μm (green) band. Figure 29 compares an annotated video image showing the locations of the soils with the ratioed image of these two bands. The darker soil areas correspond to those with 10 YR hues, while the lighter areas have 5 YR hues on the ratioed image. It is likely that the differences in hue result from the relative ferric iron content of the soil parent materials, but the sample analysis is not yet complete enough to confirm this hypothesis. Obvious differences related to the average lightness or darkness of these soils (Munsell value) were reduced with this ratio image. Contrasts related to Munsell value, which are apparent on the single-band image, are probably related to organic matter and relative moisture contents.

6.2.2 NATURAL SOIL DRAINAGE

Poorly drained soil areas generally appear darker than surrounding drier soils in the reflectance wavelengths ($<3 \mu\text{m}$). During the day, this contrast is often reversed in the thermal infrared band—that is, moist areas containing more organic matter appear warmer (because of their darker color) than drier soil areas. A ratio of a reflective band and a thermal band then serves to enhance differences associated with soil moisture and organic matter accumulation—usually an indication of natural soil drainage. Shown in Fig. 30 is the coincidence of a dark pattern in a bare field with a soil mapped as poorly drained. Differences between well drained and somewhat poorly drained are not so obvious, however.

6.2.3 VEGETATION VIGOR

The ability of a ratioed image to enhance tone differences associated with terrain conditions depends on the existence of relative spectral differences in two or more bands. The most effective differences are tone reversals from one band to another. For example, comparisons of vegetation in the 0.62- to 0.70- μm (red) chlorophyll-absorption band and the 0.70- to 0.94- μm (near-infrared) reflectance band show that vigorous vegetation is darker in the red band and lighter in the infrared band than stressed or less-dense vegetation. Examples of these differences in lawn vigor are shown for a small town in western Virginia in April, 1971. Figure

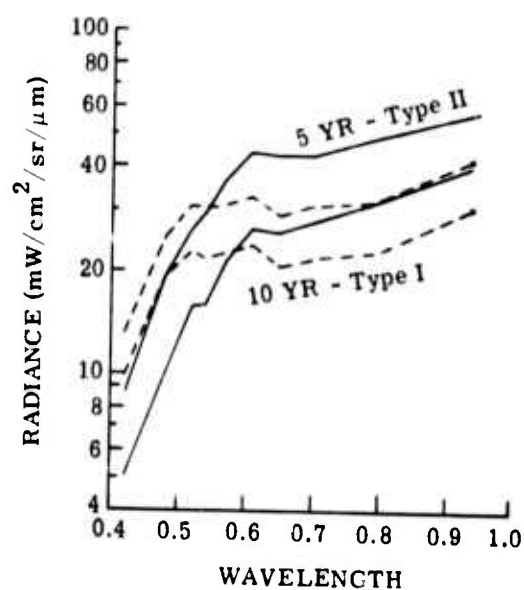
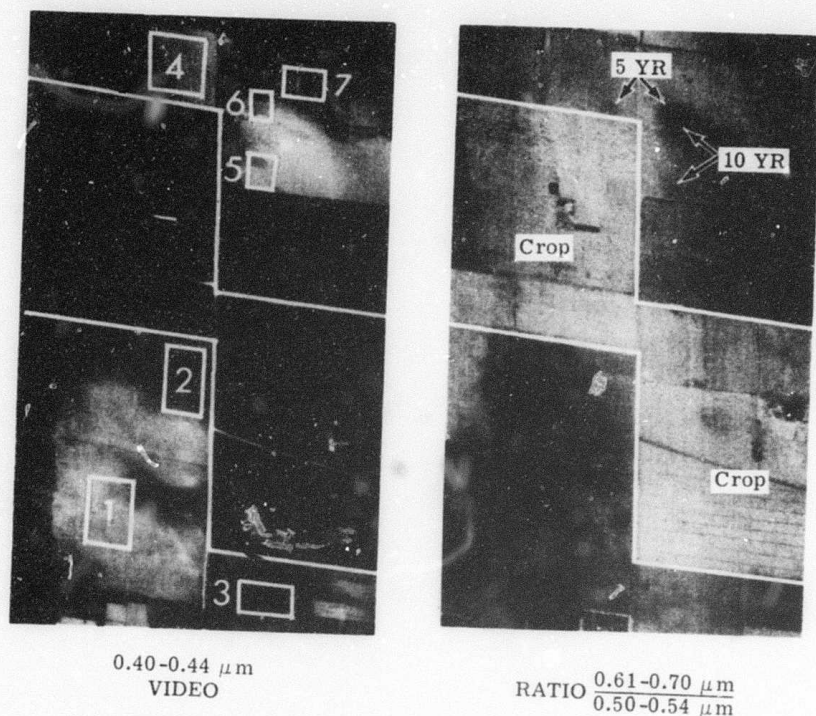


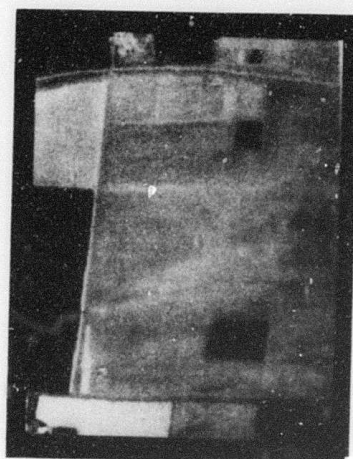
FIGURE 28. MAXIMUM AND MINIMUM RADIANCE FOR TWO COLORS OF SOIL (10 YR AND 5 YR). From Weslaco, Texas — 20 sample locations.



SAMPLE AREA

1	10 YR 6/3
2	5 YR 5/4
3	3 YR 5/4
4	5 YR 5/4
5	10 YR 4/3
6	10 YR 5/2
7	5 YR 5/4

FIGURE 29. COMPARISON OF A SINGLE-BAND VIDEO IMAGE WITH A RATIOED IMAGE. Dark soil areas on the ratioed image correspond to 10 YR hues, light areas to 5 YR hues.



Thermal Image
9.3-11.7 μm



Near-IR Image
1.5-1.8 μm



Ratio Image
 $\frac{9.3-11.7 \mu\text{m}}{1.5-1.8 \mu\text{m}}$



Soil Map
W-Well drained
S-Somewhat poorly
drained
P-Poorly drained

FIGURE 30. ENHANCEMENT OF NATURAL SOIL DRAINAGE

31 compares black-and-white aerial photographs with a near-IR red ratioed image — these data were processed for the Federal Highway Administration [38].

6.2.4 SCENE CONTRAST SUPPRESSION

Aerial images typically show terrain contrasts related largely to land use practices. In agricultural areas, bare fields often are light in tone in comparison to fields with dark green crops. These sharp contrasts have the effect of concealing other, more subtle, terrain patterns related to drainage, physiography, or natural vegetation distribution. Also, the occurrence of intensive dark areas on the imagery makes it less suitable as a field mapping base — because of the difficulty in seeing pen or pencil annotations in these dark areas.

Figure 32 demonstrates that the ability exists to reduce these marked contrasts significantly with ratioed images of two spectrally similar bands (green and violet in this case). Using different bands has the effect of emphasizing or suppressing different combinations of terrain patterns to different degrees. The ratioed figure in this example reduces most of the contrast within the cultivated areas but maintains contrast for the wooded portions of the image. The latter areas are scarcely discernible on the single-channel video image — a panchromatic photograph would appear similar to this video image.

6.2.5 SOIL EMITTANCE

Energy radiated from a soil surface in the thermal infrared portion of the spectrum ($>3 \mu\text{m}$) is primarily a function of the emittance and absolute temperature of the soil. Absolute temperature, in turn, is dependent on the thermal properties of the soil and the diurnally changing, local climatic conditions.

Emittance characteristics of soils (that is, how closely they simulate a theoretically perfect emitter — a "blackbody") are wavelength-dependent. In the 8- to 10- μm range, soil thermal emittance is lowered by the so-called reststrahlen effects of silicate minerals. This lower emittance reduces the apparent radiant energy (blackbody temperature) in this range in comparison to the apparent radiant energy at other wavelengths for the same soil. Field observations reported at Purdue [39] show the decrease in apparent temperature in the 8- to 10- μm range for mineral soils and a sandy-gravel road (see Fig. 33). Greater apparent temperature

38. T. W. Wagner and P. G. Hasell, Jr., Remote Identification of Terrain Features and Materials at Virginia Test Sites - An Investigation Study of Techniques, Environmental Research Institute of Michigan, Report No. 27600-9-T, 1973.

39. Annual Report No. 4, Laboratory for Agricultural Remote Sensing, Purdue University, 1971.

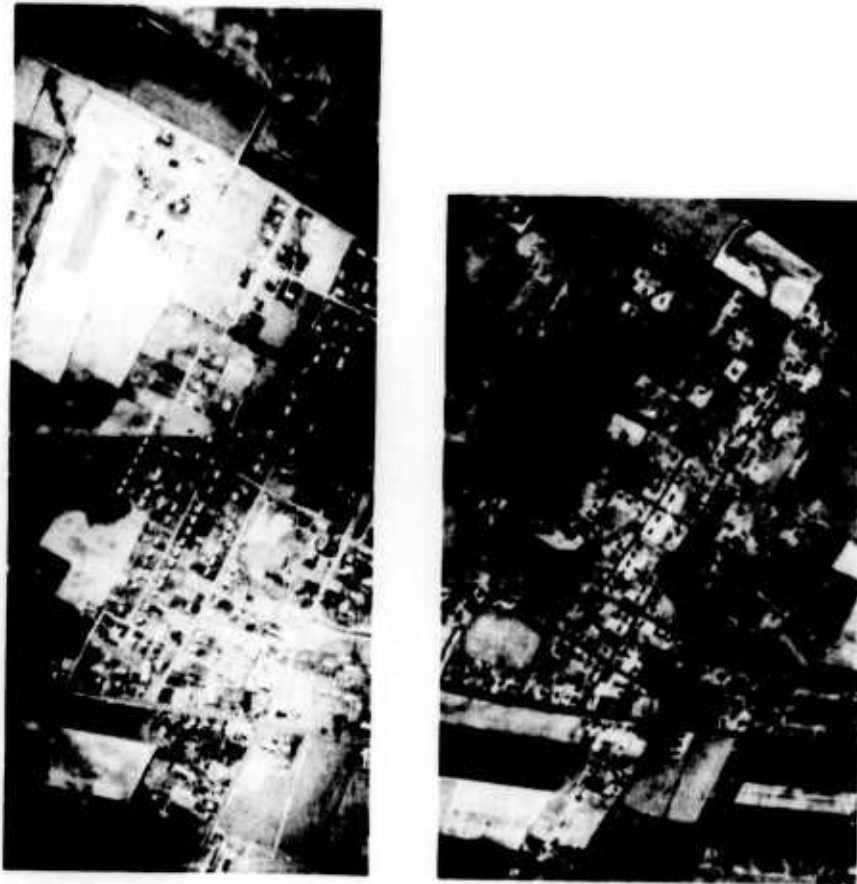


FIGURE 31. COMPARISON OF BLACK AND WHITE PANCHROMATIC PHOTOMOSAIC (LEFT) WITH A RATIOED IMAGE FOR VEGETATION VIGOR ENHANCEMENT (RIGHT). Light areas show vigorous vegetation. Dark areas are non-vegetated.



FIGURE 32. COMPARISON OF A VIDEO IMAGE OF AGRICULTURAL LAND USE WITH A RATIOED IMAGE OF THE SAME AREA. Ratio image is designed to suppress scene contrast associated with cropped versus bare fields. Dark area in upper right is a cloud shadow.

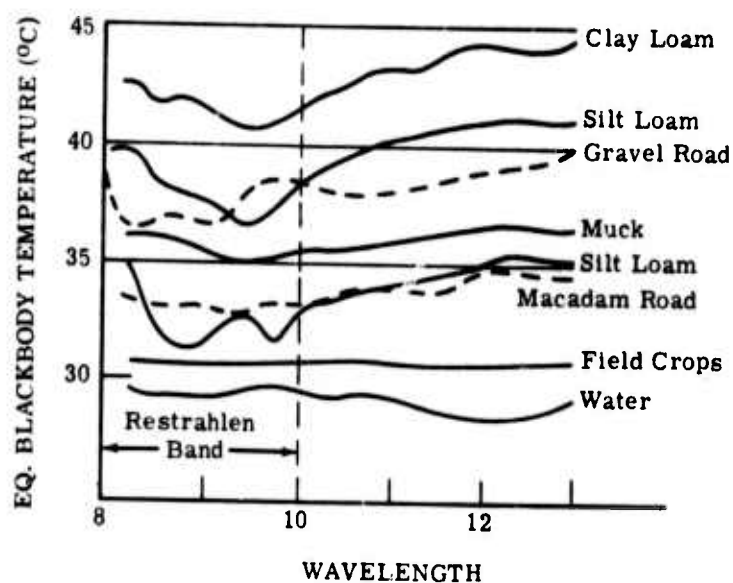


FIGURE 33. BLACKBODY TEMPERATURES SHOWING THE RESTRAHLEN EFFECT FOR MINERAL SOILS IN THE 8 TO 10 μ m WAVELENGTH RANGE. Data from LARS (Purdue) — annual report No. 4.

differences are indicated for the two silt loam soils than for the clay loam soil, and the organic muck soil shows little variation in the reststrahlen band. Also, the crop vegetation, hard-surfaced road, and water surface show little or no apparent temperature variation in this range. Absolute temperature values are not of concern here.

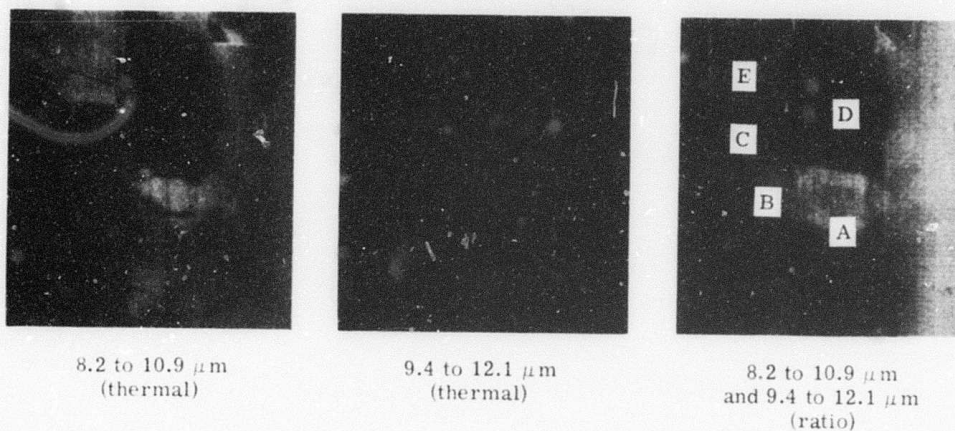
Roughly, the greater the SiO_2 content of a soil surface, the lower the soil emittance is expected to be in the 8- to 10- μm range. Since SiO_2 frequently makes up the bulk of the sand-size fraction of well-weathered soils, a rough correlation between a ratio of two thermal bands and surface soil texture may be possible. Indeed, the reststrahlen effect has been shown to vary somewhat with particle size as well as with mineral content [40].

To test this approach to remote determination of soil texture, two bands of thermal infrared imagery collected near Weslaco, Texas, were ratioed. The two bands used were in the 8.0- to 10.9- μm and the 9.4- to 12.1- μm wavelength ranges—the former being the reststrahlen band for silicate minerals. Results are presented in Fig. 34. Four soil types ranging from clay loam to loamy fine sand, plus field crops, are shown in the scene. While it would not be possible to identify these soil types individually from the single thermal images, it appears that the ratioed image does indicate by tone contrast (darker areas have sandier textures) the locations of differing soil types. Soil samples collected from this area are currently being analyzed and should provide confirmation of this conclusion. It should be noted that differences in soil moisture and in cultivation practices are likely to affect ratioed image results—in addition to any effect produced by the silicate composition of these soils.

6.3 MULTICHANNEL RECOGNITION

If soils or other materials of interest are sufficiently different from one another in their spectra, they should be discriminable in some manner. Consider two objects, A and B, in two spectral bands (dimensions), as shown in Fig. 35. These objects of interest may be recognized by ascertaining that a sample occurs within some boundary about the objects in the space (λ_1 , λ_2). In this example, little confusion is possible since the objects do not overlap. They may be discriminated by very simple boundaries, such as a ratio value. But more complex situations arise in nature; here, simple two-dimensional boundaries can cause misclassification of scene objects of interest. For example, with ratio discrimination, note that portions of object C would be mistakenly classified as either object A or B. In such cases, a more general type of boundary is necessary, usually based on a statistical model in which the probabilities or likeli-

40. R. J. P. Lyon, Evaluation of Infrared Spectrophotometry for Compositional Analysis of Lunar and Planetary Soils, NASA Report No. 49104, Stanford Research Institute, 1964.



Area:

- A - Rio clay loam
- B - Ramadero sandy clay loam
- C - Hidalgo fine sandy loam
- D - Hebbroville loamy fine sand (?)
- E - Crop vegetation

FIGURE 34. COMPARISON OF TWO THERMAL IMAGES WITH
A RATIOED IMAGE OF A SOIL TEST AREA NEAR WESLACO,
TEXAS

hoods of the various objects are compared for each sample to be classified. It is often necessary that the spectral characteristics of several objects be considered simultaneously to obtain the best results. Multi-channel analog and digital computer techniques have been developed for this purpose.

In situations where the spectral distributions of objects overlap or are expected to overlap (generally the case), simple ratio techniques do not provide adequate discrimination capabilities. The concept of likelihood—making a decision on the basis of probability—is more appropriate. If the two distributions, A and B, overlap (see Fig. 36), equi-probable contours are drawn for the distributions of objects A and B. At the intersections of those contours of equal probability value, A and B are equally likely or probable; and a curve may be drawn through these points to form a decision surface on either side of which decisions may be made for any point. The function used for this decision is known as the likelihood ratio:

$$L(A|\lambda_1, \lambda_2) = \frac{p(A|\lambda_1, \lambda_2)}{p(B|\lambda_1, \lambda_2)} \quad (11)$$

where L = the likelihood ratio

$p(A|\lambda_1, \lambda_2)$ = the probability of object A, given measurements (λ_1, λ_2)

$p(B|\lambda_1, \lambda_2)$ = the probability of object B, given measurements (λ_1, λ_2)

If the decision rule is established such that

$$L = \frac{p(A|\lambda_1, \lambda_2)}{p(B|\lambda_1, \lambda_2)} \geq 1 \quad (12)$$

then this is a likelihood-ratio decision, and the bounds are represented by this decision rule. Fast computers allow the extension of this likelihood decision concept to a number of dimensions (spectral bands) and multiples of objects.

Using soil sample areas selected from southeastern Michigan, an analog image processor, SPARC, was used to implement this likelihood-ratio decision rule. The processor accepted data from four spectral bands for three surface soils and applied the likelihood test to determine the distribution of these materials for the flightline. The assumption is made that the probability distribution of the samples is approximated by a normal or Gaussian distribution.

Signals from each of the four selected spectral bands are supplied to summing amplifiers from a tape-loop recorder, along with the mean values for the particular object of interest. The level at the output of the first summer is set to a particular value by manually adjusting a potentiometer ($1/\sigma_1$). Outputs from the summers are repetitively examined on an x-y oscilloscope and adjusted to show no correlation. The level of the signal at the output of the

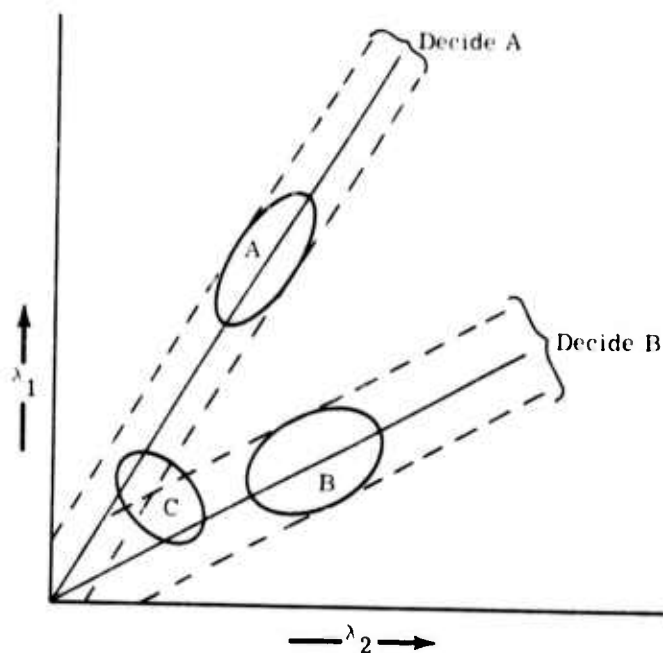


FIGURE 35. SPECTRAL DISTRIBUTION OF TWO MATERIALS AND RATIO DECISION BOUNDARIES

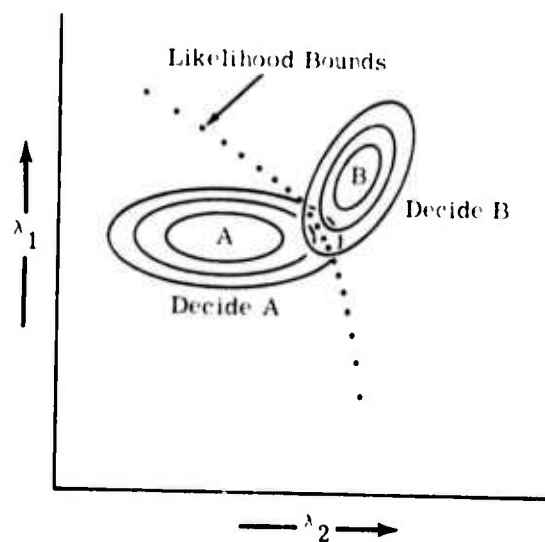


FIGURE 36. OVERLAPPING SPECTRAL DISTRIBUTIONS OF TWO MATERIALS AND LIKELIHOOD-RATIO DECISION BOUNDARY

second summer is set to the same value as the output of the first by adjusting the second potentiometer, and so on. These signals, now uncorrelated, are squared and added to obtain the exponent of the normal distribution. The output is then exponentiated to obtain the probability of all the signals.

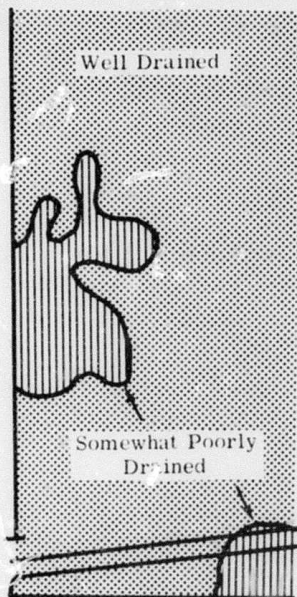
The same operations are performed on the signals for all other sample material distributions. The outputs are then supplied to the final summer with the proper sign and tested with a threshold device. If the unknown output signal is greater than a present threshold, an object of interest is registered as present. This final output signal is displayed on a CRT and photographed with a filmstrip printer. Thus, the output is a black (object) and clear (not object) recognition filmstrip showing, point by point, the results of the likelihood test for each material in the entire study area.

Two examples of multichannel recognition of soil areas are included here for illustration—both areas are in southern Michigan. Figure 37 shows recognition of three soil types having different drainage characteristics. For purposes of comparison, a drainage map (based on existing soil survey maps) is provided. The computer-generated distribution of well-drained and somewhat poorly drained soils compares well with the soil drainage map, although there is considerably greater detail in the processed imagery. The somewhat poorly drained soils occur on the lower slopes of this undulating terrain. Poorly drained soils recognized by the computer constitute too small an area to be differentiated on the conventional map. Field examination determined that these areas were correctly delineated. The multispectral data used to produce these images were collected at 2000 ft altitude. The following spectral bands were employed: 0.48-0.52 μm (blue-green), 0.67-0.94 μm (near-IR), 2.0-2.6 μm (mid-IR), and 9.3-11.7 μm (thermal-IR).

The currently orbiting Earth Resources Technology Satellite (ERTS) also collects multispectral data, but at a much coarser resolution because of its 500 mi altitude. Figure 38 shows an attempt to differentiate different soil drainage classes by using ERTS multispectral data. In this example, correlation of the digital computer-generated results with existing soil maps indicates that consistently correct identification of these bare fields occurred only in the case of the mineral versus organic (peat and muck) soils. These data were collected at a sub-optimum time of year for soils differentiation (less than 10% of the ground was free of vegetative cover, as indicated by sparse soil recognition). Research is continuing into the use of orbital multispectral imagery to separate soil drainage classes.

6.4 TOWARD AN OPERATIONAL SYSTEM

Earlier, we suggested several requirements which should be met if we are to consider multispectral systems for an operational role in soil surveys. Ultimately, we must be con-



Soil Drainage Map



Well Drained
(Miami Series)



Somewhat Poorly Drained
(Conover Series)



Poorly Drained
(Brookston Series)

FIGURE 37. COMPARISON OF A CONVENTIONAL SOIL DRAINAGE MAP WITH SOIL RECOGNITION IMAGES FOR FLEMING CREEK WATERSHED

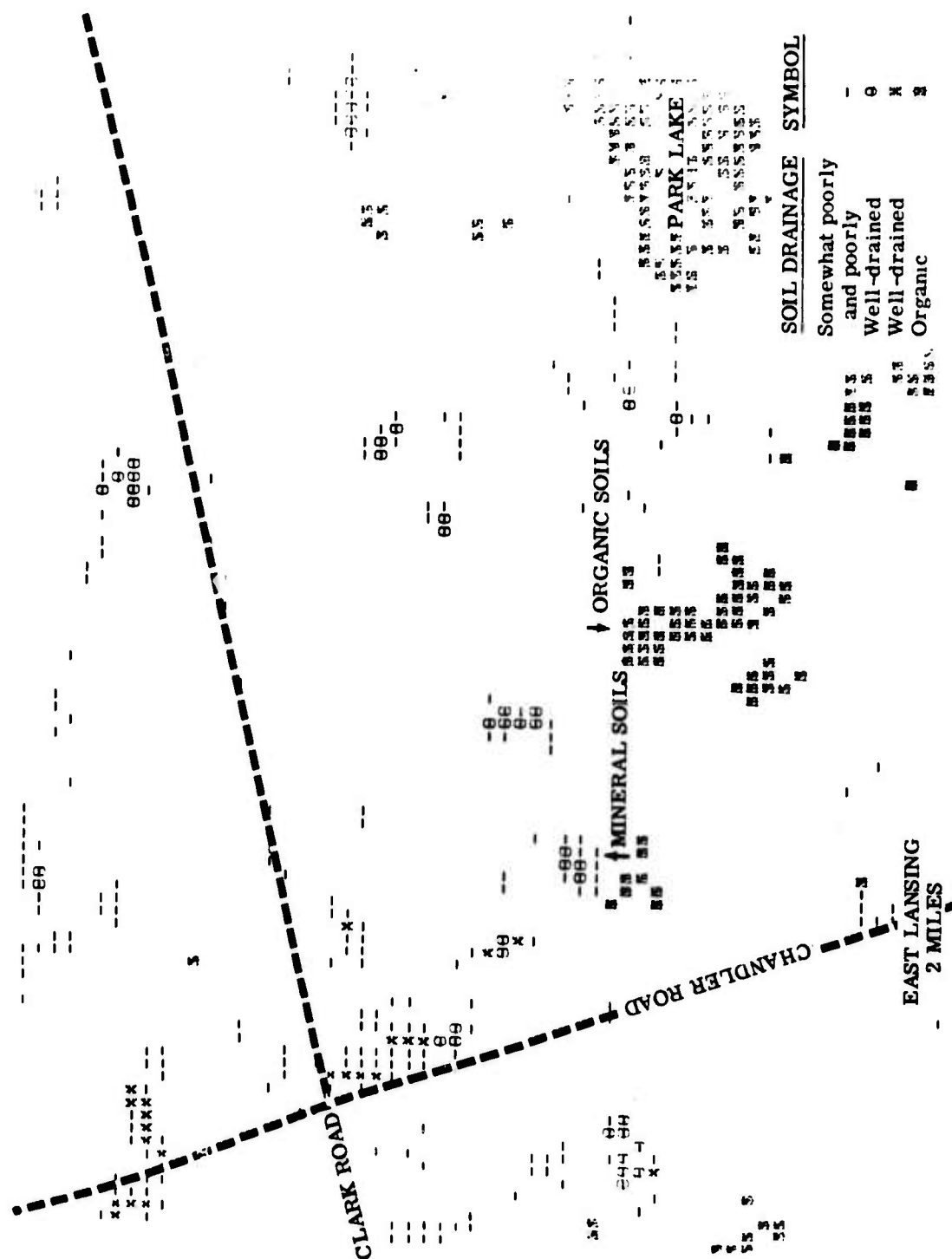


FIGURE 38. MAXIMUM LIKELIHOOD RECOGNITION MAP FOR SOILS SIGNATURES ONLY

cerned with such applications if we are to justify continued public support for the development of such systems. What are some of the limitations in the application of multispectral data for identifying and mapping soil conditions?

One limitation is that often only a portion of the soil is exposed to aerial view in an area to be surveyed. To maximize bare soil areas, it is necessary to collect remote sensor data from agricultural areas either in the fall or, preferably, in the spring prior to substantial crop growth. Even then, there will be areas of perennial vegetation or cultural development for which no direct soil information can be obtained from aerial imagery. Aerial imagery can delineate only surface or near surface conditions; taxonomic soil units established from subsurface profiles cannot be identified from imagery. Precise identification of soils must still be made on the ground. Remote sensors can help extrapolate those observations, reduce their numbers, and provide easier determinations of soil boundaries; but they cannot replace the task of field sampling.

The processed results presented here were produced in a research mode using an experimental scanner and playback system. Other techniques may prove to be better suited for enhancement of these or other, more useful soil conditions. For example, a ratio of two frequencies of radar data hopefully may provide new synoptic information concerning near-surface properties of different soils. Experiments are currently underway to test this idea.

In time, we hope to attach numerical ranges to absolute values for certain soil conditions. If successful, this may make possible an automatic discrimination process to select and print-out recognition images of soil conditions from selected ratios. Here, discrimination could be accomplished automatically by a simple level-slicing, or thresholding, procedure.

6.4.1 SPECTRAL VARIATIONS

In addition to enhancing contrasts associated with soil conditions, ratioed images reduce certain scene variations which occur as a result of illumination or directional reflectance differences. Recent studies have shown that soils are not uniformly diffusing Lambertian surfaces. When the sun angle is low, the same soil can have quite different appearances — depending upon the direction of view (see Fig. 39). Variations in terrain slope and aspect can have a similar effect even when the sun is high. These effects, associated with solar direction, look angle geometry, and terrain slope, are recorded by the scanner. Frequently, one side of a video image is uniformly lighter than the other side as a result of scanning alternately into and away from the sun's direction. These scan angle variations are only slightly wavelength-dependent. A ratio of two bands, particularly two bands which are spectrally close, effectively reduces this directional reflectance variation. Ratios of adjacent bands have been used for a number of years as a preprocessing technique to eliminate gross directional-reflectance variations.

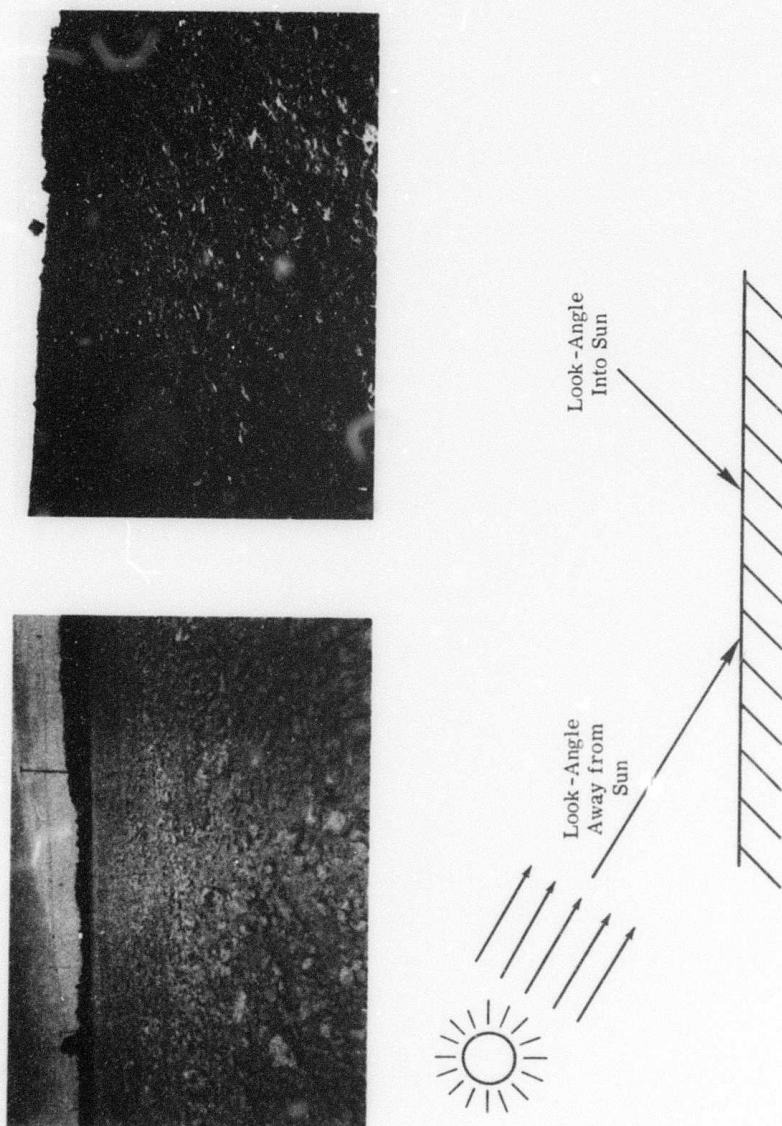


FIGURE 39. DIRECTIONAL REFLECTANCE OF SOIL SURFACES

Solar illumination may also vary as the aircraft collects data along a flightline. Again, these variations are not strongly wavelength-dependent, and a ratio of two reflective bands helps eliminate cloud shadows and other types of illumination variations.

6.4.2 CONCLUSIONS

We have attempted to present some of the kinds of soil information available from selectively enhanced multispectral images — soil color, terrain patterns, natural drainage, and soil texture. The relative simplicity of the ratio approach seems to commend it for study as a source of soil survey imagery. On the other hand, experience with single video images indicates no more soil information than is contained in aerial photography. Statistical recognition processing is laborious, and additional research into its use in standard survey practice is required.

Ratioed images are produced at the same real-time rate as single-band video playbacks and at a comparable cost. If the soil surveyor can suggest what kinds of surface soil and terrain conditions would be useful for discriminating and mapping soils in his area, he might be able to specify the ratios most likely to emphasize any soil differences. When the resulting enhanced images are produced, he can then use the full range of his knowledge and experience in interpreting them. Other ratios of multispectral bands used for enhancing vegetation differences have been reported recently [41, 42]. These may also prove useful to the soil scientist in terrain areas where he cannot observe the soil surface directly.

41. R. L. Pearson and L. D. Miller, Remote Mapping of Standing Crop Biomass for Estimation of the Productivity of the Shortgrass Prairie, Pawnee National Grasslands, Colorado, Proceedings of the 8th International Symposium on Remote Sensing of Environment, Vol. II, October 1972, pp. 1355-1379.

42. C. E. Olson, Jr., Remote Sensing of *Fomes annosus* in Forest Stands, Proceedings of the 8th International Symposium on Remote Sensing of Environment, Vol. II, October 1972, pp. 1381-1384.

GENERAL CONCLUSIONS AND RECOMMENDATIONS

Remote sensing for geologic reconnaissance is on the verge of becoming operational. ERTS-1 has already performed the two tasks of alerting the user community to remote sensing and providing data with which to develop useful analysis procedures. Because of the wide publicity given the successful experiments of ERTS-1, the authors believe that any further justification for, description of, or proof of the usefulness of remote sensing for geologic purposes would be redundant. Therefore, we have concentrated on contributing directly to the further development of geologic remote sensing. To this end, a test site was selected in the Black Hills of South Dakota, and MSS airborne data were collected during two flights in May, 1972. Although the cost of gathering complementary SLAR data expressly for this contract was prohibitive, Strategic Air Command SLAR imagery was obtained for a portion of the area flown; it could not be included in this report because of analysis-time limitations.

We feel that we made significant advances in adopting and utilizing remote data for the purposes of geologic and soils analysis. The primary technique employed was that of image ratioing, a straightforward processing method which is not only economical but which has an image format similar to that of an aerial photo; in the future, the process can even be accomplished in real time.

By ratioing pairs of multispectral images, the following geologic features can be discriminated:

- (1) exposed rock areas
- (2) separate rock groups, including Precambrian quartzite; Precambrian phyllite, slate, and schist; basal quartzite and sandstone; and intrusives such as rhyolite, quartz latite, quartz monsonite, and phonolite
- (3) large-scale structures; faults, folds, intrusive bodies, and regional trends.

In addition, soil color, terrain patterns, natural drainage, and soil texture are enhanced by ratio images.

To help make the data processing automatic, a gating logic has been developed for ratioed images. The basis of this logic is to use a known ratio range for each rock type in the preparation of recognition maps. All ratio values which fall into a preset range for a given rock type are selected and automatically placed in the map location of the rock's appearance in the scanned scene. Statistical procedures based on laboratory measurements can provide a firm basis for discrimination of rock types.

These advances in remote sensing analysis are supplemental to the thermal and mineralogical determinations accomplished earlier and described in the previous annual report.

The techniques described in detail in this report now need to be extended as follows: (1) by application to more rock, soil, and vegetation types, and (2) through the simple addition of airborne ratio logic in order to obtain real-time ratioed data. Because the procedures we used must be considered investigative, each step requiring the judgment of an experienced researcher, our first recommendation is that enough analyses be performed to establish a solid experimental and theoretical basis for the operational use of ratioing. Our further recommendation is that a straightforward airborne operational system be developed and flown to serve potential users.

REFERENCES

1. Richard W. Bayley, Structure and Mineralization of Precambrian Rocks in the Galena-Roubaix District, Black Hills, South Dakota, USGS Bull. 1312-E, 1970, 15pp.
2. J. A. Noble and J. O. Harder, Stratigraphy and Metamorphism in a Part of the Northern Black Hills and the Homestake Mine, Lead, South Dakota, Geol. Soc. Amer. Bull., Vol. 59, 1948, pp. 941-976.
3. N. H. Darton and S. Paige, Central Black Hills Folio (219), USGS Geologic Atlas, 1925, 35pp.
4. J. A. Noble, J. O. Harder, and A. L. Slaughter, Structure of a Part of the Northern Black Hills and the Homestake Mine, Lead, South Dakota, Geol. Soc. Amer. Bull., Vol. 60, 1949, pp. 321-352.
5. L. H. Shapiro and J. P. Gries, Ore Deposits in Rocks of Paleozoic and Tertiary Age of the Northern Black Hills, South Dakota, USGS Heavy Metals Program, Contract No. 14-08-0001-10650, 1970, 235pp.
6. Richard W. Bayley, Preliminary Geologic Map of the Nemo District, Black Hills, South Dakota, Misc. Geologic Investigations, Map I-712, 1972.
7. A. L. Slaughter, The Homestake Mine: Ore Deposits in the United States 1933-1967, AIME, 1968, pp. 1436-1459.
8. R. K. Vincent, R. Horvath, F. Thomson, and E. Work, Remote Sensing Data-Analysis Projects Associated with the NASA Earth Resources Spectral Information System, The University of Michigan, Report No. 3165-77-T, NASA Contract NAS9-9784, 1972.
9. R. K. Vincent and F. Thomson, Spectral Compositional Imaging of Silicate Rocks, J. of Geophys. Res., Vol. 77, 1972, pp. 2465-2471.
10. R. K. Vincent, Rock-Type Discrimination from Ratio Images of the Pisgah Crater, California Test Site, The University of Michigan, Report No. 3165-77-T, NASA Contract NAS9-9784, 1972.
11. R. K. Vincent, F. Thomson, and K. Watson, Recognition of Exposed Quartz Sand and Sandstone by Two-Channel Infrared Imagery, J. of Geophys. Res., Vol. 77, 1972, pp. 2473-2477.
12. R. K. Vincent and F. Thomson, Rock Type Discrimination from Ratioed Infrared Scanner Images of Pisgah Crater, California, Science, Vol. 175, 1972, pp. 986-988.
13. Robert Vincent, A Thermal Infrared Ratio Imaging Method for Mapping Compositional Variations Among Silicate Rock Types, unpublished Ph.D. dissertation, The University of Michigan, 1973.
14. T. Wagner, R. K. Vincent, B. Drake, R. Mitchell, and P. Jackson, Tunnel-Site Selection by Remote Sensing Techniques, The University of Michigan, Tech. Report No. 10018-13-F, U.S. Bureau of Mines Contract HO210041 (ARPA Order No. I579, Amend. 2, Program Code IF10), 1972.
15. D. Anding, R. Kauth, and R. Turner, Atmospheric Effects on Infrared Multi-spectral Sensing of Sea Temperature from Space, Willow Run Laboratories, Report No. 2676-5-F, 1970.
16. W. L. Wolfe, ed., Handbook of Military Infrared Technology, U.S. Office of Naval Research, Department of the Navy, Washington, 1965, pp. 9-20.

17. N. Draper and H. Smith, *Applied Regression Analysis*, John Wiley and Sons, Inc., New York, 1967, pp. 171-172.
18. K. A. Rodgers, R. H. A. Cochrane, and P. C. LeCouteur, Fortran II and Fortran IV Programs for Petrochemical Calculations, *Mineralogical Magazine*, 37, 1970, pp. 952-953.
19. W. Cross, J. P. Iddings, L. V. Pirsson, and H. S. Washington, A Quantitative Chemico-Mineralogical Classification and Nomenclature of Igneous Rocks, *J. of Geology*, 10, 1902, pp. 555-690.
20. A. Johannsen, *A Descriptive Petrography of the Igneous Rocks*, Vol. 1, The University of Chicago Press, Chicago, 1931, pp. 85-88.
21. N. G. Ware, Department of Geophysics, Australian National University, Canberra, Private Communication, 1973.
22. E. Essene, Department of Geology and Mineralogy, The University of Michigan, Ann Arbor, Private Communication, 1973.
23. R. B. Travis, Classification of Rocks, *Quarterly of the Colorado School of Mines*, 50, 1955, p. 12.
24. B. L. Joiner, N. F. Laubscher, E. S. Brown, and B. Levy, An Author and Permuted Title Index to Selected Statistical Journals (1961-1969), National Bureau of Standards Publication 321, U.S. Department of Commerce, Washington, 1970.
25. E. B. Wilson, Jr., *An Introduction to Scientific Research*, McGraw-Hill Book Co., Inc., New York, 1952, p. 273.
26. W. G. Ernst, *Earth Materials*, Prentice-Hall, Inc., Englewood Cliffs, 1969, p. 135.
27. R. K. Vincent, The NASA Earth Resources Spectral Information System: A Data Compilation-Second Supplement, Environmental Research Institute of Michigan, Tech. Report No. 31650-156-T, NASA Contract NAS9-9784, 1973.
28. K. Szechy, *The Art of Tunneling*, Akademiai Kiado, Budapest, 1967.
29. R. E. Frost, et al., Photointerpretation of Soils, *Manual of Photographic Interpretation* (R. N. Colwell, ed.), Am. Society of Photogrammetry, 1960, pp. 343-402.
30. V. C. Miller and S. A. Schumm, Aerial Photographs and Surface Features, Aerial Surveys and Integrated Studies: Proceedings of the Toulouse Conference, UNESCO, Paris, 1968, pp. 41-79.
31. A. H. Gerbermann, H. W. Gausman, and C. L. Wiegand, Color and False Color-IR Films for Soils Identification, *Photogrammetric Engineering*, Vol. 37, No. 4, 1971, pp. 359-364.
32. P. G. Hasell, Jr., Michigan Experimental Multispectral Scanner System, Proceedings of 4th Annual Earth Resources Review, NASA, January 17-21, 1972, pp. 34-1 through 34-13.
33. G. Nagy, G. Shelton, and J. Toloba, Procedural Questions in Signature Analysis, Proceedings of the 7th International Symposium on Remote Sensing of Environment, Vol. II, May 1971, pp. 1387-1401.
34. R. F. Nalepka and J. P. Morgenstern, Signature Extension: An Approach to Operational Multispectral Surveys, Environmental Research Institute of Michigan, Report No. 3165-152-T, 1973.

35. H. R. Condit, Application of Characteristics Vector Analysis to the Spectral Energy Distribution of Daylight and Spectral Reflectance of American Soils, *Applied Optics*, Vol. 11, No. 1, 1972, pp. 74-86.
36. J. A. Shields, et al., Measurements of Soil Color, *Canadian Journal of Soil Science*, Vol. 46, 1966, pp. 83-90.
37. A. H. Munsell, A Color Notation, Munsell Color Co., Inc., Baltimore, 1947.
38. T. W. Wagner and P. G. Hasell, Jr., Remote Identification of Terrain Features and Materials at Virginia Test Sites — An Investigation Study of Techniques, Environmental Research Institute of Michigan, Report No. 27600-9-T, 1973.
39. Annual Report No. 4, Laboratory for Agricultural Remote Sensing, Purdue University, 1971.
40. R. J. P. Lyon, Evaluation of Infrared Spectrophotometry for Compositional Analysis of Lunar and Planetary Soils, NASA Report No. 49104, Stanford Research Institute, 1964.
41. R. L. Pearson and L. D. Miller, Remote Mapping of Standing Crop Biomass for Estimation of the Productivity of the Shortgrass Prairie, Pawnee National Grasslands, Colorado, Proceedings of the 8th International Symposium on Remote Sensing of Environment, Vol. II, October 1972, pp. 1355-1379.
42. C. E. Olson, Jr., Remote Sensing of *Fomes annosus* in Forest Stands, Proceedings of the 8th International Symposium on Remote Sensing of Environment, Vol. II, October 1972, pp. 1381-1384.